STUDY OF SOUND ATTENUATION IN ELLIPTIC DUCTS

BY

SUBHABRATA BANERJEE

DISSERTATION

Submitted in partial fulfillment of the requirements
for the degree of Doctor of Philosophy in Mechanical Engineering
in the Graduate College of the
University of Illinois at Urbana-Champaign, 2015

Urbana, Illinois

Doctoral Committee:

Professor Anthony M. Jacobi, Chair & Director of Research
Professor Daniel J. Bodony
Professor Predrag S. Hrnjak
Professor William D. O'Brien, Jr.

Abstract

The acoustic emission resulting from the reciprocating motion of machinery parts, such as the movement of pistons and the intake/exhaust of gases in an automotive engine, or the pressure pulsation generated in compressors cause noise pollution. Passive noise–attenuating devices such as mufflers are usually employed in the intake or the exhaust flow path of such systems. A typical muffler element consists of an expansion chamber with inlet and outlet ports for the passage of the exhaust fluid. The difference in the size of the ports from the chamber dimensions presents an impedance mismatch to the propagating acoustic wave, resulting in partial or complete reflection of the sound energy. Mufflers can broadly be classified as reactive type or dissipative type. Reactive mufflers employ the principle of impedance mismatch by incorporating area changes in the transmission path. Dissipative mufflers usually have some kind of absorptive lining that converts sound energy into heat. In comparison to reactive mufflers, dissipative mufflers usually have a sound attenuation over a wider frequency range. However, pressure drop and particle clogging limit their application.

The sound attenuation characteristics of a muffler is dependent on various factors like shape and size of the muffler, orientations of inlet/ outlet ports, and number of inlet/outlet ports. Since the parameter space involved is potentially very large, only a few muffler geometries have been extensively studied in the past, viz. circular or rectangular chamber mufflers. More recently, mufflers having elliptical cross-sections have received some attention. These types of mufflers require smaller space across one of the dimensions, and are suitable for applications where space constraints are an important design consideration. The existing literature on elliptic reactive mufflers is not extensive; therefore, further attention to this geometry is required. The present work aims to study the sound attenuation in elliptic reactive mufflers using a perturbation–based approach. Although exact solutions for such geometries are available in terms of the elliptic eigenfunctions, the perturbation based approach may be implemented for more general asymmetric

distortions (within moderate eccentricity). Using this approach, the effects of the ellipticity and port–extensions on the sound attenuation are analyzed in this work. The perturbation method is then extended to study the breakout noise from distorted ducts. It has been long established that distortions in ducts significantly alter the sound radiation when subjected to an internal acoustic field. However, most of the reported work had been confined to very small distortions, and plane-wave (acoustic) propagation within the duct. The present work aims to improve on these limitations and provide a solution method for studying the sound radiation from moderately distorted ducts when excited by a point acoustic source. Using an analytical approach suggested earlier, the radiated sound field of an elliptic duct (eccentricity $e = 0.6$) is observed to be much higher (as much as 30 $dB,\ L_w$) than a cylindrical shell of comparable dimensions.

The final part of this dissertation aims to determine the effect of a liquid phase on the sound attenuation in a muffler geometry. The liquid phase is expected to act like a compliant surface, thereby affecting the sound transmission. However, analytical study of a simple rectangular duct and experimental measurement of transmission loss indicate that the wall compliance effects are negligible and may be neglected.

Acknowledgments

I would like to thank my advisor, Professor Anthony M. Jacobi for his mentoring during my doctoral studies. He has been a strong pillar for my academic advancement and personal growth during my stay at the university. His encouraging support for this research, both intellectually and financially, is the sole reason for its successful completion.

I would like to thank my committee members Prof. William D. O'Brien, Jr., Prof. Predrag S. Hrnjak, and Prof. Daniel J. Bodony for their valuable suggestions. My appreciation goes to all the faculty and staff members, and especially Kathy Smith and Lisa Burdin of the Department of Mechanical Science & Engineering for providing an excellent academic environment.

This study was partially funded by the Air–Conditioning and Refrigeration Center (ACRC) at the University of Illinois at Urbana–Champaign. I would like to thank all the industry members of the ACRC for supporting this work.

I am grateful to my lab–mates and friends, especially Rahul (Kolekar), Juan, Jessie, Nathan, Rong, Feini, Mina, Matt, Srikanthan, Vivek, Ashique, Kashif, Rahul(Agarwal), Nikhil, Jayanta, Raj and Pavan for the wonderful times I spent with them.

Finally I would like to thank my parents, my brother and my sister-in-law, who have always been my source of inspiration and strength through all these years.

Contents

List of Tables vi

List of Figures vii

Chapter 1 Introduction 1
1.1 Review of the literature 2
1.2 Objectives 11
1.3 Organization of the thesis 12

Chapter 2 Analytical formulation of the transmission loss 14
2.1 Analytical determination of the TL 14
2.2 Extension of GFM for mufflers with multiple inlet/outlet ports 21
2.3 Validation: cylindrical geometries 23
2.4 Validation: elliptic geometries 35
2.5 Summary 39

Chapter 3 Transmission loss in distorted cylindrical mufflers 40
3.1 Mathematical formulation 40
3.2 Numerical verification: TL in expansion chamber elliptic mufflers 49
3.3 Numerical implementation: TL in extended tube elliptic chamber mufflers 60
3.4 Summary 66

Chapter 4 Study of wall compliance on the radiation and transmission 67
4.1 Structure–acoustic coupled formulation of radiation field from a distorted shell . . 67
4.2 Numerical verification: Radiation from simply–supported cylindrical shell 74
4.3 Numerical implementation: Radiation from an elliptic shell 74
4.4 Effects of a liquid layer on the TL in a duct 78
4.5 Summary 83

Chapter 5 Conclusions 85

Bibliography 88

List of Tables

3.1 Comparison of cut-off frequency (Hz) of different even modes at various eccentricities. Area of cross section is same as a circle of radius 0.09 m for all cases. 56
3.2 Comparison of cut-off frequency (Hz) of different even modes at various eccentricities. Area of cross section is same as a circle of radius 0.09 m for all cases. 57
3.3 Natural frequencies of different even modes for the annular elliptic chamber 65
3.4 Natural frequencies of different even modes for the elliptic chamber 65

List of Figures

1.1 Schematic of an expansion chamber muffler, corresponding electrical analogies, and transfer–matrix representation of the field variables (acoustic pressure and volume velocity) [2] . . . 3
1.2 Schematic description of the instantaneous axial pressure field for higher–order mode propagation, tunneling and leakage of a mode [11] . . . 4
1.3 Predicted ($-\cdot-\cdot-$) and measured (•) transmission loss of a long–seam circular duct from ideally circular duct model; —— from distorted circular duct model [40] . . . 10

2.1 Schematic of an extended tube muffler with elliptic chamber. . . . 17
2.2 Particle velocity along a radial line at the inlet port surface of a cylindrical expansion chamber muffler. Black: real part; Red: imaginary part; - - - - MMM; ——— MMM with $(A_n^-, n > 0)$ and $(E_n^+, n > 0)$ equal to zero; ratio of inlet to chamber diameter is 0.31 . . . 19
2.3 Comparison of the TL using the GFM and the MMM for chamber length, $L = 0.05\ m$. Black: MMM; Green: MMM with $(A_n^-, n > 0)$ and $(E_n^+, n > 0)$ equal to zero; Red: GFM. Red and Green are overlapped . . . 20
2.4 Comparison of the TL using the GFM and the MMM for chamber length, $L = 0.10\ m$. Black: MMM; Green: MMM with $(A_n^-, n > 0)$ and $(E_n^+, n > 0)$ equal to zero; Red: GFM. Red and Green are overlapped . . . 20
2.5 Schematic of the mufflers used for validation of the present method [70, 69]; (a) SIDO muffler: $D = 0.153\ m$, $d_1 = d_2 = d_3 = 0.0486\ m$ (b) DISO muffler: $D = 0.153\ m$, $L = 0.54\ m$, $d_1 = d_2 = 0.0486\ m$, $d_3 = 0.0584\ m$ . . . 24
2.6 TL curve for SIDO mufflers with circular cross section of the chamber, $L/D = 0.205$: —— GFM; ····· Selamet and Ji [70] (a) $\delta_1 = \delta_2 = \delta_3 = 0.051\ m$, $\varphi_1 = \varphi_2 = 0$, $\varphi_3 = \pi$ (b) $\delta_1 = \delta_2 = \delta_3 = 0.051\ m$, $\varphi_1 = 0$, $\varphi_2 = \pi/2$, $\varphi_3 = \pi$ (c) $\delta_1 = \delta_2 = 0.051\ m$, $= \delta_3 = 0\ m$, $\varphi_1 = 0$, $\varphi_2 = \pi/2$, $\varphi_3 = 0$ (d) $\delta_1 = \delta_2 = \delta_3 = 0.051\ m$, $\varphi_1 = 0$, $\varphi_2 = \pi/2$, $\varphi_3 = 3\pi/2$ . . . 25
2.7 TL curve for SIDO mufflers with circular cross section of the chamber, $L/D = 1.84$: —— GFM; ····· Selamet and Ji [70] (a) $\delta_1 = \delta_2 = \delta_3 = 0.051\ m$, $\varphi_1 = \varphi_2 = 0$, $\varphi_3 = \pi$ (b) $\delta_1 = \delta_2 = \delta_3 = 0.051\ m$, $\varphi_1 = 0$, $\varphi_2 = \pi/2$, $\varphi_3 = \pi$ (c) $\delta_1 = \delta_2 = 0.051\ m$, $= \delta_3 = 0\ m$, $\varphi_1 = 0$, $\varphi_2 = \pi/2$, $\varphi_3 = 0$ (d) $\delta_1 = \delta_2 = \delta_3 = 0.051\ m$, $\varphi_1 = 0$, $\varphi_2 = \pi/2$, $\varphi_3 = 3\pi/2$ . . . 26

2.8 TL curve for DISO mufflers with circular cross section of the chamber: —— GFM; ····· Selamet and Ji [69] (a) $L_3 = L/8$, $P_1^+/P_2^+ = 1$ (b) $L_3 = 2L/8$, $P_1^+/P_2^+ = 1$ (c) $L_3 = L/8$, $P_1^+/P_2^+ = -1$ (d) $L_3 = L/8$, $P_1^+/P_2^+ = 1i$ 26
2.9 Schematic of various SIDO muffler orientations. $L = 0.30\ m$, $D = 0.122\ m$ 27
2.10 TL comparison of mufflers having inlet/outlets as shown in Fig. 2.9(a). $L_3 = L/2$, $\delta = 0.6276R$; ——— SIDO muffler, $d_1 = d_2 = d_3 = D/5$; –o–o–o– End-inlet/end-offset outlet muffler, $d_1 = d_2 = D/5$, $d_3 = 0$; +++ End-inlet/side-outlet muffler, $d_1 = d_3 = D/5$, $d_2 = 0$ 27
2.11 Input impedance and TL of an end–inlet/side outlet cylindrical muffler of length $L = 0.30\ m$, $D = 0.122\ m$. The different curves indicate the variation due to the change in the outlet port location L_3; ———, $L_3 = 0.15L$; ———, $L_3 = 0.35L$; ———, $L_3 = 0.55L$; ———, $L_3 = 0.75L$ 29
2.12 Normalized input impedance and TL of an end–inlet/side outlet cylindrical muffler of length $L = 0.30\ m$, $D = 0.122\ m$. The different curves indicate the variation due to the change in the outlet port location L_3; ———, $L_3 = 0.15L$; ———, $L_3 = 0.35L$; ———, $L_3 = 0.55L$; ———, $L_3 = 0.75L$ 30
2.13 TL comparison of mufflers having inlet/outlets as shown in Fig. 2.9(b). $L_2 = L_3 = L/2$; ——— SIDO muffler, $d_1 = d_2 = d_3 = D/5$; –o–o–o– End-inlet/side-outlet muffler, $d_1 = d_3 = D/5$, $d_2 = 0$ 31
2.14 TL comparison of mufflers having inlet/outlets as shown in Fig. 2.9(c). $d_1 = d_2 = d_3 = D/5$; ——— $L_1 = L/2$; –o–o–o– $L_1 = L/4$; +++ $L_1 = L/6$ 31
2.15 TL comparison of mufflers having inlet/outlets as shown in Fig. 2.9(d). $d_1 = d_2 = d_3 = D/5$; ——— $L_1 = L/2$, $L_2 = L_3 = L/4$; +++ $L_1 = L/2$, $L_2 = L/6$, $= L_3 = 5L/6$; –o–o–o– $L_1 = L/2$, $L_2 = L/8$, $= L_3 = 7L/8$ 32
2.16 TL comparison of mufflers having inlet/outlets as shown in Fig. 2.9(d). $d_1 = d_2 = d_3 = D/5$; ——— DISO, $L_1 = L/2$, $L_2 = L_3 = L/4$, $P_2^+/P_3^+ = 1$; +++ SIDO, $L_1 = L/2$, $L_2 = L_3 = L/4$; –o–o–o– DISO, $L_1 = L/2$, $L_2 = L_3 = L/4$, $P_2^+/P_3^+ = 1i$ 33
2.17 TL comparison of mufflers having inlet/outlets as shown in Fig. 2.9(a). $d_1 = d_2 = d_3 = D/5$, $\delta = 0.6276R$; ——— $L_2 = L$, $L_3 = L/2$, $P_2^+/P_3^+ = 1$; –o–o–o– $L_2 = L$, $L_3 = L/2$, $P_2^+/P_3^+ = 1i$ 34
2.18 TL comparison of mufflers having inlet/outlets as shown in Fig. 2.9(c). $d_1 = d_2 = d_3 = D/5$, $\delta = 0.6276R$; ——— $P_2^+/P_3^+ = 1$; –o–o–o– $P_2^+/P_3^+ = 1i$; - - - - - $\triangle TL = 10\log_{10} 2$; –x–x–x– $\triangle TL$ 34
2.19 Numerical verification of the GFM applied to an elliptic SIDO muffler configuration. —— GFM; ····· MMM in Ref. [72]. $L = 0.3\ m$, semi-major axis $a = 0.115\ m$, semi-minor axis $b = 0.065\ m$, $\varphi_1 = \varphi_2 = 0$, $\varphi_3 = \pi$ (a) $\delta_1 = 0, \delta_2 = \delta_3 = 0.073\ m$ (b) $\delta_1 = \delta_2 = \delta_3 = 0.073\ m$ (c) $\delta_1 = 0.05\ m$, $\delta_2 = 0.06\ m$, $\delta_3 = 0.03\ m$ (d) $\delta_1 = 0$, $\delta_2 = \delta_3 = 0.048\ m$ 36
2.20 TL of an elliptic muffler having inlet/outlets and same area and length as shown in Fig. 2.9(b). $L_2 = L_3 = L/2$; ——— SIDO muffler, $d_1 = d_2 = d_3 = D/5$ . . . 37
2.21 TL of an elliptic muffler having inlet/outlets and same area and length as shown in Fig. 2.9(c). $d_1 = d_2 = d_3 = D/5$; ——— $L_1 = L/2$; –o–o–o– $L_1 = L/4$; +++ $L_1 = L/6$ 37

2.22 TL of an elliptic muffler having inlet/outlets and same area and length as shown in Fig. 2.9(a); $P_2^+/P_3^+ = 1$, $d_1 = d_2 = d_3 = D/5$; ——— $L_3 = L/2$; +++ $L_3 = 3L/4$ 38

3.1 Schematic of an annular perturbed cylinder. 41
3.2 Schematic diagram of elliptical mufflers with different inlet/outlet configurations: (a) Concentric chamber muffler (b) Concentric-inlet-offset-outlet muffler (c) Reversing chamber muffler (d) End-inlet-side-outlet (EISO) muffler. 50
3.3 Transmission loss characteristics at different eccentricities (e), and chamber lengths (L) for concentric chamber configuration. · · · · · · ·, Perturbation solution; ——— Exact solution. 51
3.4 Transmission loss characteristics at different eccentricities (e), and chamber lengths (L) for concentric-inlet-offset-outlet chamber configuration. · · · · · · ·, Perturbation solution; ——— Exact solution. 52
3.5 Transmission loss characteristics at different eccentricities (e), and chamber lengths (L) for reversing chamber configuration. · · · · · · ·, Perturbation solution; ——— Exact solution. 53
3.6 Transmission loss characteristics at different eccentricities (e), and chamber lengths (L) for EISO chamber configuration. · · · · · · ·, Perturbation solution; ——— Exact solution. 54
3.7 Cross-section view of even mode shapes of ellipse with eccentricity, · · · · · · ·, Perturbation solution; ——— Exact solution. 55
3.8 Variation of the non-dimensional radial wavenumber with eccentricity, for various even order modes. 59
3.9 Locus of the pressure nodes for the (2, 1) and the (0, 2) even modes: $ABCDE$, $A'B'C'D'E'$ are the pressure nodal lines for the (2, 1) mode; $BFDD'F'B'B$ is the pressure nodal circle for the (0, 2) mode. 60
3.10 Locus of the (2, 1) pressure nodal point on the major-axis of the ellipse as a function of eccentricity. 60
3.11 Transmission loss characteristics at different chamber lengths (L) for the concentric-inlet-offset-outlet chamber configuration; the outlet port is located at the (2, 1) pressure node on the major-axis. 61
3.12 Transmission loss characteristics at different chamber lengths (L) for the concentric-inlet-offset-outlet chamber configuration; the outlet port is located at the intersection of the (2, 1) and the (0, 2) pressure node. 61
3.13 Radial distance δ and angular position θ, of the point of intersection of the (2, 1), and (0, 2) even modes. 62
3.14 TL in an elliptic chamber muffler with extended inlet/outlet ports: $L = 25$ cm, $L_B = 10$ cm, $L_D = 0$ cm, $d_1 = d_2 = 3.3$ cm, $e = 0.6$, $a = 10$ cm; ———, Perturbation result; o o o o, FEM result. 63
3.15 TL in an elliptic chamber muffler with extended inlet/outlet ports: $L = 25$ cm, $L_B = 10$ cm, $L_D = 0$ cm, $d_1 = d_2 = 3.3$ cm, $e = 0.6$, $a = 10$ cm; ———, Perturbation result; o o o o, FEM result. 63
3.16 TL in an elliptic chamber muffler with extended inlet/outlet ports: $L = 25$ cm, $L_B = 5$ cm, $L_D = 5$ cm, $d_1 = d_2 = 3.3$ cm, $e = 0.6$, $a = 10$ cm; ———, Perturbation result; o o o o, FEM result. 64

3.17 TL in an elliptic chamber muffler with extended inlet/outlet ports: $L = 25$ cm, $d_1 = d_2 = 3.3$ cm, $e = 0.6$, $a = 10$ cm; ~~o o o o o~~, $L_B = 5.5$ cm, $L_D = 0$ cm; ~~□□□□□~~, $L_B = 11.6$ cm, $L_D = 0$ cm; ———, $L_B = 11.6$ cm, $L_D = 5.5$ cm. 65

4.1 Validation of the perturbation–based sound radiation model when eccentricity, $e \rightarrow 0$; ———, present formulation; ———, Laulagnet and Guyader[53] 75
4.2 ———, Sound power level from an elliptic shell with simply–supported boundary conditions, $e = 0.6$, $L = 1.2$ m; –o–o–o–, cylindrical shell of same area of cross-section ($r = 0.2$ m) as the elliptic shell 76
4.3 Sound power level from an elliptic shell with simply–supported boundary conditions:———, equivalent cylindrical shell is considered for the structure, $e = 0.6$, $L = 1.2$ m; –o–o–o–, cylindrical shell of same area of cross-section ($r = 0.2$ m) as the elliptic shell 77
4.4 Sound power level from an elliptic shell with simply–supported boundary conditions:———, equivalent cylindrical is considered for the internal acoustic field, $e = 0.6$, $L = 1.2$ m; –o–o–o–, cylindrical shell of same area of cross-section ($r = 0.2$ m) as the elliptic shell 77
4.5 Schematic of the cross–section of a square duct of edge a. (a) The duct is filled with water upto a height of h; (b) Equivalent duct cross–section when the liquid layer is treated as a rigid layer 80
4.6 Schematic diagram of the experimental apparatus for measuring the TL 81
4.7 Measured reflection coefficient at a downstream location in the test apparatus . . . 81
4.8 Transmission loss in a square muffler of edge $a = 0.108$ m, length, $L = 0.292$ m. The height of water level, $h = 0$ m. ———, Analytical model based on the equivalent geometry in Fig. 4.5(b); –o–o–o–, Experimental results 82
4.9 Transmission loss in a square muffler of edge $a = 0.108$ m, length, $L = 0.292$ m. The height of water level, $h = 0.023$ m. ———, Analytical model based on the equivalent geometry in Fig. 4.5(b); –o–o–o–, Experimental results 82
4.10 Transmission loss in a square muffler of edge $a = 0.108$ m, length, $L = 0.292$ m. The height of water level, $h = 0.029$ m. ———, Analytical model based on the equivalent geometry in Fig. 4.5(b); –o–o–o–, Experimental results 83

Chapter 1

Introduction

The reciprocating motion of engine pistons and the intake/exhaust of gases generate significant noise in an automotive engine, causing environmental pollution. In order to attenuate such noise, mufflers are used. Mufflers can be classified as either reactive (or reflective) or dissipative. Reactive mufflers are passive noise attenuating devices based on the principle of impedance mismatch. Dissipative mufflers have absorptive lining which converts sound energy into heat. With the ever increasing requirement of reducing noise pollution, the study of various muffler geometries is an active area of research. While numerical methods like finite element method (FEM) or the boundary element method (BEM) have proved to be very useful (especially for complicated muffler geometries), significant contributions to this field has been made through analytical/semi–analytical studies. The sound attenuation characteristics of a muffler are dependent on various factors like shape and size of the muffler, orientations of inlet/ outlet ports, and number of inlet/outlet ports. Since the parameter space involved is potentially very large, only a few muffler geometries have been extensively studied in the past, viz. circular or rectangular chamber mufflers. More recently, mufflers having elliptical cross–sections have received attention. These types of mufflers require smaller space across one of the dimensions, and are suitable for applications where space constraints are an important design consideration. The existing literature on elliptic reactive mufflers is not extensive; therefore, further attention to this geometry is required.

In many applications, distortions in the duct occur either due to manufacturing defects, or due to some design requirement. The presence of boundary asymmetries may affect the sound attenuation characteristics of a muffler. The effect of boundary asymmetries on the breakout noise from cylindrical ducts has been reported in the literature. Research on the sound attenuation in distorted muffler is lacking. While FEM/BEM can be implemented for such asymmetric geometries, more physical insight can be gained through analytical means. If the distortions are

not large compared to the unperturbed geometry, approximate methods can be implemented to develop analytical solutions for such mufflers.

The 'breakout' or 'breakin' noise from ducts used in heating, ventilation and air–conditioning (HVAC) or in other gas flowing ducting systems is an important area of study in acoustics. Noise generated due to the vibration of ducts can be transmitted to the building space, thereby posing problems. The study of structural noise due to a mechanical excitation, or due to the presence of a noise source has been detailed in the literature. It has been observed that duct discontinuities causes increased sound transmission; only few works have been reported on distorted ducts.

1.1 Review of the literature

1.1.1 Analytical study of sound attenuation in mufflers

Analytical study of sound attenuation in mufflers has been an active area of research with extensive work on mufflers having rectangular or circular cross–sections. A typical muffler element consists of an expansion chamber with inlet and outlet ports for the passage of the exhaust fluid. The difference in the size of the ports from the chamber dimension presents an impedance mismatch to the propagating acoustic wave, resulting in partial or complete reflection of the sound energy. This method of passive attenuation is primarily employed for designing of reactive mufflers, especially for low frequency applications. The simplest of analytical techniques assumes plane–wave propagation in the muffler [1]. Based on this assumption, the upstream condition (acoustic pressure and velocity) is derived in terms of the downstream condition such that the pressure and volume velocity are same across each region of discontinuity. Although the continuity of the pressure and volume velocity is fundamental, and is independent of the plane–wave simplification, the above assumption is made to eliminate mathematical complexities that arise due to higher–order mode contributions. The plane–wave approach was improved by Igarashi and Toyama [2]. Using an electrical circuit analogy (Fig. 1.1), they were able to derive the upstream conditions in terms of the downstream pressure and velocity through a matrix representation known as the transfer matrix (or the four–pole parameter). The transfer matrix may be imagined as an equivalent impedance that maps the pressure and velocity in a muffler. Munjal [3, 4, 5] discussed the basic concepts of four–pole parameters and derived them for different muffler configurations with rigid–wall boundary conditions. This method is applicable at low

frequencies, where higher–order modes are not excited. Even at low frequencies, higher–order

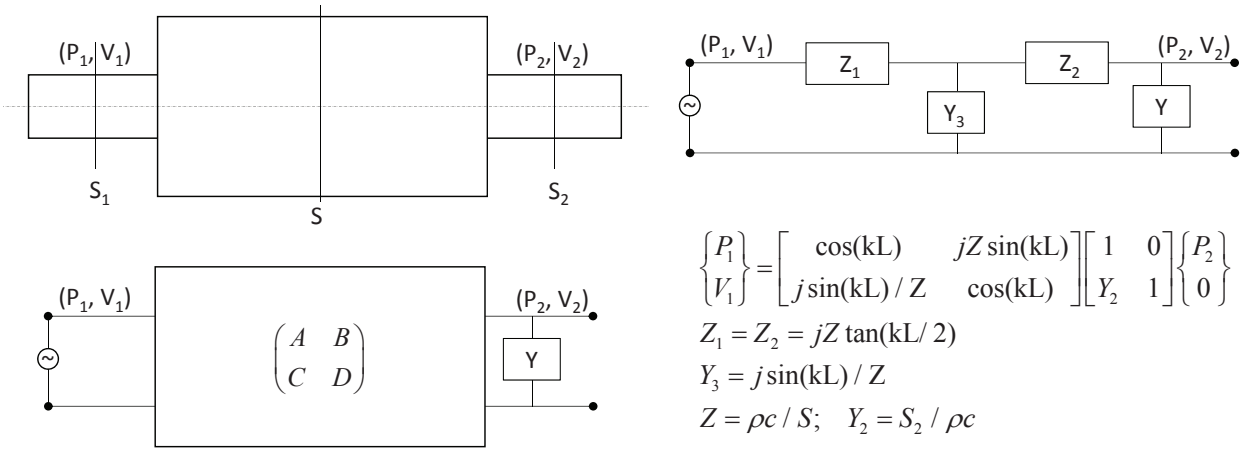

Figure 1.1: Schematic of an expansion chamber muffler, corresponding electrical analogies, and transfer–matrix representation of the field variables (acoustic pressure and volume velocity) [2]

evanescent modes are generated at duct discontinuities, which may not decay for acoustically short mufflers. When two tubes of different cross sections are joined together, abrupt change of area results in an additional impedance [6]. This impedance is of the form of an inductance. The constriction inductance is usually accounted by an equivalent increase in length of the duct. The one–dimensional method for mufflers employs these corrected lengths for deriving the transmission loss [TL]. Therefore, the one–dimensional method relies on the accuracy of the predicted end corrections; extensive work on determining the end corrections for cylindrical chambers with extended inlet/outlet have been reported in the literature [7, 8, 9, 10].

Eriksson [11] investigated various mechanisms of propagation of excited modes in a chamber. Leakage and tunneling effects (Fig. 1.2), implying excitation of higher–order modes at duct discontinuities and their incomplete attenuation due to small duct length, was discussed. The existence of higher–order modes severely restricts the use of the plane–wave model. In order to accommodate the effects of propagation of these modes on sound attenuation, Kim and Soedel [12, 13] developed a point–source method to derive four–pole parameter for three dimensional cavities using modal superposition. The method was based on the assumption that inlet and outlet ports had relatively small dimensions in comparison to the size of the chamber and wavelengths of interest, thereby allowing for point–source assumption. Numerical accuracy of the point–source method can be improved by considering piston driven sources with uniform velocity. Ih and Lee [14] formulated a piston–driven–source model to find TL in circular mufflers with

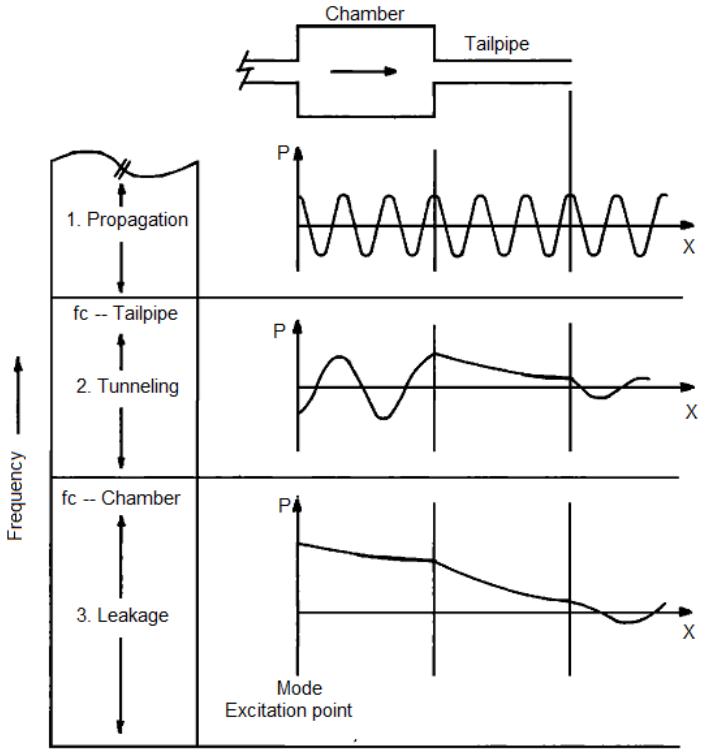

Figure 1.2: Schematic description of the instantaneous axial pressure field for higher–order mode propagation, tunneling and leakage of a mode [11]

mean flow effects. The method relied on finding a series solution to Helmholtz equation. The contribution of each term (coefficients) of the expansion was obtained by imposing boundary conditions. The pressure at each port was taken as an average over the port area. The mean flow was observed to cause a shift in cutoff frequencies of different modes. The piston–driven–source method was implemented by Yi and Lee [15, 16] for a cylindrical reversing chamber, and for mufflers with side inlet/outlet. The possibility of obtaining broadband attenuation by suitable location of ports was a key contribution of their work. Similar to piston–driven–source model, Kim and Kang [17] used a Green's function solution method (GFM) to calculate four–pole parameters of a circular muffler. Their work may be considered as an extension of the method proposed by Kim and Soedel [12, 13]; improvement in the accuracy of the formulation was obtained due to the piston–driven source approximation. Eigensolutions of Helmholtz equation were derived within the muffler domain. The Helmholtz equation being self–adjoint, yielded an orthogonal set of eigenvectors. A Green's function was derived as a series expansion of eigensolutions. Although similar to piston–driven–source method, the GFM was mathematically simpler

way of deriving TL. Moreover, boundary discontinuities due to the piston sources could be incorporated by using the Green's identities, allowing for the study of various inlet/outlet port orientations with minimum changes in the formulation. Venkatesham *et al*. [18] implemented the GFM method to rectangular geometries having different inlet/outlet locations.

The assumption of uniform velocity piston sources is relaxed in mode matching method (MMM) [19, 20, 21]. The MMM is based on continuity of acoustic field variables across a section. It considers higher–order mode propagation in both the chamber and pipe, making it more accurate than other analytical methods. Some of the earliest work on the sound transmission and reflection at a duct–discontinuity using the principles of the MMM may be attributed to Miles [22] and Karal [6]. El–Sharkawy and Nayfeh [19], extended the idea of the MMM in the study of the TL in a circular expansion chamber muffler. In their approach, the pressure field inside the muffler expressed in terms of the eigensolutions of the Helmholtz equation were obtained through orthogonalization. Selamet and co–workers [23, 24, 25, 26] employed the MMM for a wide range of inlet/outlet port orientations, and wall impedances in a cylindrical geometry. Unlike Green's function method, MMM can be implemented for muffler geometries where area discontinuity occurs within the muffler. However, this method involves solution of theoretically an infinite number of linear simultaneous equations, truncated up to a suitable order; matrix ill–conditioning often occurs, making inversion difficult and possibly inaccurate. Similar work on circular and rectangular geometries can be found in the literature [27, 28].

Unlike circular and rectangular geometries, very few works have been reported in the literature on sound propagation and attenuation in elliptical chamber mufflers. Elliptical mufflers though inferior to circular mufflers in attenuating noise, require less space. They are widely used as automobile mufflers, where clearance from the ground is an important design criterion. One of the earliest works on sound propagation in elliptic waveguides is due to Lowson and Bhaskaran [29], who evaluated the cutoff frequencies for various higher–order modes assuming rigid boundary conditions. Hong and Kim [30] developed a similar solution procedure to determine the mode shapes and natural frequencies in an annular confocal elliptical chamber. The splitting of eigenvalues due to loss of rotational symmetry was discussed in their work. It was observed that natural frequency of an odd mode shape (mode shapes that are not symmetric about the major axis) was higher than to the corresponding even mode shape (mode shapes that are symmetric about the major axis). Denia *et al*. [31] detailed TL in an elliptical muffler

of various lengths with concentric inlet/outlet, reversing, and offset inlet/outlet port locations. Through their work it was evident that acoustically long elliptical mufflers had poorer sound attenuation compared to an equivalent circular chamber muffler. This deterioration in sound attenuation was due to propagation of certain higher–order modes which would not have propagated in a circular muffler with similar inlet/outlet configuration. However, as the walls are closer in an ellipse, it is expected that by using absorbent liners the sound attenuation in an elliptical muffler should show better sound attenuation than a similar cylindrical chamber [29]. Research on dissipative elliptical mufflers has not been reported in the literature to validate such hypothesis. Selamet and Denia [32] studied the TL for short elliptic mufflers with end inlet/ side outlet port locations, using the finite element method (FEM). Recent works on elliptic mufflers using the GFM have been reported in the literature [33, 34], where the effects of the higher–order transverse modes on the sound attenuation were discussed.

1.1.2 Study of boundary perturbation problems

In many applications, geometrical asymmetries may exist due to manufacturing defects. In other cases, asymmetry may be due to a design requirement. For example, due to space constraints, most car mufflers are either oval or elliptic in cross–sections and not circular. Sound attenuation in a muffler is very sensitive to geometry. Depending on the axial length of muffler, cross–section, and location of inlet/outlet ports, different acoustic modes may be excited or suppressed. The presence of any boundary asymmetry in an otherwise rotationally symmetric muffler adds components from other unperturbed mode shapes. Inclusion of these additional modes may result in an attenuation characteristic very different from the undistorted muffler. The agreement between the analytical methods and experimental and numerical results, and their relative ease in implementation, makes them an excellent choice for analyzing the eigenvalue problems with regular geometries. However, these exact solutions are available only for geometries conforming to coordinate systems where method of separation of variables is possible. Analysis of eigenvalue problems in irregular geometries has largely been numerical with a few exceptions. Sewall *et al*. [35] developed a Raleigh–Ritz approach to study natural frequencies and mode shapes of vibrating elliptic shell under different boundary conditions. Nayfeh *et al*. [36] employed the method of strained parameters to determine natural frequencies and mode shapes of annular and circular plates with small perturbations at the boundary. The splitting of eigenvalues due to

loss of radial symmetry was established in their work. Roberts [37] used a conformal mapping technique to study the natural frequencies of a perturbed membrane. DiPerna *et al*. [38] also used a conformal mapping method to study the far–field scattered pressure due to a plane–wave incident upon an infinitely long cylinder of noncircular cross section. Their method was observed to work well over a wide variation in circular cross–section. Parker and Mote [39] implemented a fifth–order perturbation method similar to the formulations developed by Nayfeh *et al*. [36] in determining eigensolutions of two–dimensional wave equation in a distorted circular domain. Guidelines for occurrences of mode splitting were developed in their work. Distorted cylinders have been of interest in the study of wall vibrations due to an internal acoustic field [40, 41] as well. It was concluded through these studies that wall distortions caused structural and acoustic mode–coupling, which resulted in different sound transmission characteristics from an ideal undistorted shell. Sarkar and Sonti [42] developed a perturbation–based formulations of the governing equations for an infinite *in–vacuo* and fluid–filled elliptical cylindrical shell. The equations were then solved to give *in–vacuo* and coupled wavenumbers.

1.1.3 Sound transmission through duct walls

In heating, ventilation and air–conditioning (HVAC) and in other gas flow ducting systems, acoustic breakout and breakin through the duct walls might be a significant source of noise, especially if the walls are made of fairly thin sheet metal. Internal noise transmitted through the walls of ventilation ducts into buildings can pose a problem, particularly at low frequencies. The study of noise radiated by structural vibration has been a subject of considerable practical interest. In most applications the vibrating structure can be roughly modeled as flat plates or a collection of flat plates with appropriate boundary conditions. The flat–plate approximation along with a simply supported boundary condition, results in relatively simple modeling of the structural response.

In one of the earlier works on the sound radiation from flat plates, Wallace [43] determined the acoustic pressure at the farfield from a simply supported rectangular panel in an infinite baffle. Employing a Rayleigh integral approach, the radiation resistances of various plate modes were quantified. Fahy and Gardonio [44] presented some interesting observation on the radiation efficiency based on the modal phase cell patterns that effectively reduce the structural excitation into 'edge' and 'corner' radiators.

A simplified method for determining the acoustic field in an enclosed cavity was proposed by Dowell *et al*. [45]. Using the *in–vacuo* structural modes and the acoustic modes for a rigid cavity, the structure–acoustic coupled problem was reformulated into an infinite number of ODE's in time. Dowell's method proved extremely useful for harmonic excitations, whereby the ODE's could be transformed into a set of linear equations. Extension of Dowell's work has been successfully implemented in the study of radiation from unbaffled plates, rectangular cavities with flexible surfaces, and sound radiation from shells [46, 47, 48, 49]. Kim and Brennan [47] developed an impedance–mobility model to study the response of structure–acoustic coupled systems under the excitation of an internal sound field/ mechanical force. Their formulation was similar to the model developed by Dowell *et al*. with the added advantage of a compact matrix formulation, thereby providing easy numerical implementation. Venkatesham *et al*. [48, 49] implemented the impedance–mobility approach to determine the breakout noise from a rectangular plenum under the excitation from a sound source. The impedance–mobility approach was based on the assumption of a weak coupling between flexible structure and acoustic field outside the cavity. This assumption holds true if the external fluid is light in comparison to the structure. However, if the external fluid has density of the same order as the structural material (e.g. water–aluminum) shell boundary pressure may not be neglected.

Similar to the study of plate–radiation, acoustic radiation from harmonically vibrating cylindrical shells is an important subject in the area of noise control. According to Stepanishen [50], the study of vibro–acoustics for such systems can be classified into two broad categories. In the first category, the reaction of the fluid to the shell vibration may be considered to be negligible, allowing for a decoupled solution approach [51, 52]. Usually, light fluids such as air surrounding a metal shell fall into this category. The decoupled approach allows for the $in-vacuo$ solution of the shell vibration. The resulting acceleration field on the shell surface may be considered as acoustic sources for deriving the external pressure field. The second approach is more involved as the fluid surrounding the shell acts like an added mass. They also modify the structural damping. This added–mass effect influences the shell vibration, which in turn affects the external acoustic field.

The coupled structure–acoustic radiation problem was effectively solved by Stepanishen [50] using modal expansion. In his approach, a finite cylindrical shell was considered and the shell displacements were approximated by the modal solutions to the shell equations. A simply–

supported boundary condition was imposed in order to minimize the mathematical complexity. The radiation impedance for the shell was derived. It was observed that the shell response for different axial modes (but same circumferential mode) were coupled through the radiation impedance imposed by the external fluid. Using the modal approach, Laulagnet and Guyader [53] examined the sound radiation from a fluid–loaded finite cylindrical shells. In their work, the cylinder was subjected to a mechanical excitation; the vibratory response was derived using the shell theory. Though the shell boundary pressure was accounted in their work, the effect of internal fluid on the structural vibrations was neglected. Similar works on shell vibro–acoustics may be found in the literature [54, 55, 56].

Analogous to the study of the noise radiation from surfaces due to a mechanical excitation, the study of sound radiation from shells when excited by an internal acoustic field is important in HVAC&R applications. A review article on this area of research was published by Cummings [57]. It has been long observed that the experimentally determined transmission loss from a cylindrical shell varied greatly from the analytical predictions (see Fig. 1.3). This discrepancy led to the idea of 'mode–coupling' [58, 40], implying that plane–wave excitation within the shell causes higher–order structural vibration. The mode–coupling effect is only observable for distorted cylindrical geometries, whereby the generalized acoustic source terms yields non-zero higher–order modal excitation components. This observation was quantitatively proved by Yousri and Fahy [58]; the effects of mode–coupling on the radiated acoustic energy were not considered in their work. Cummings *et al.* [40] developed on the idea of mode–coupling and demonstrated the effects of wall distortion on the breakout noise due to a plane–acoustic wave. The effects of higher–order acoustic modes on the radiated sound power was outside the premise of their work. Fuller [59] developed an analytical formulation of sound radiation from an infinite cylindrical shell subject to an internal monopole source. Using the Donnell–Mushtari shell equation and pressure response due to source as well as the external fluid, the shell displacements were derived. The effect of offset location of the point–source on the TL was studied in details.

1.1.4 Study of sound propagation in the presence of two–phase fluids

In many muffler applications liquid might accumulate on the bottom of the muffler. This accumulation might be due, for example, to the incomplete combustion of oil, or due to the condensation of water vapor. In a compressor muffler, two–phase vapor/liquid mixture might exist. The effect

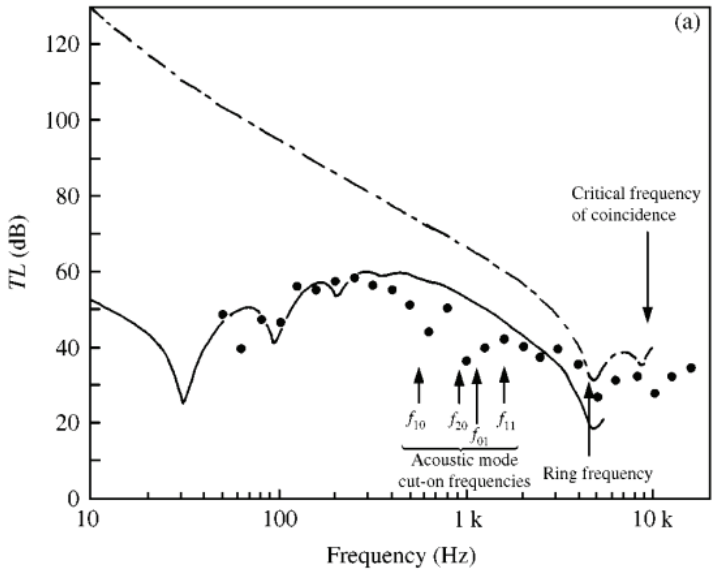

Figure 1.3: Predicted ($- \cdot - \cdot -$) and measured (•) transmission loss of a long–seam circular duct from ideally circular duct model; —— from distorted circular duct model [40]

of accumulation of liquid in a muffler or a duct has two important consequences on sound attenuation. First, the effective shape of the muffler as observed by a propagating wave gets modified due to the presence of liquid. Secondly, the liquid provides finite impedance, thereby altering the boundary conditions. The propagation of sound in a two–phase dispersed or stratified mixture has been extensively studied in the past [60]. However, no significant work has been reported on the study of sound attenuation due to presence of two–phase in a muffler/duct. The most relevant work on this area may be attributed to Morioka and Matsui [61], who studied the pressure wave propagation in one–dimensional duct containing a stratified gas–liquid layer. Dispersive relations for the mode propagation were obtained. It was observed that unlike a single phase system, the two–phase fluid showed dispersive effects even for the fundamental mode. The study of vibration in partially filled shells has been relatively more extensive compared to the acoustic analysis of such problems. Of particular interest to the present work is partially filled horizontal shells; therefore, the liquid free surface is parallel to the shell axis. Amabali [62, 63] studied the natural frequency and mode shapes of a partially filled cylindrical shell. The effect of the liquid pressure on the shell was approximated by an additional virtual mass term, and the shell equations were solved to determine the natural frequency and the mode shape. The symmetry of the problem demanded that exact solution was available only for half–filled shells. Approximation to the liquid profile was made for the case of partially filled shells. Similar studies on partially

(internally/externally) filled shell have been reported in the literature [64].

1.2 Objectives

1.2.1 Novelty of the proposed research

It is evident from the review of the literature that unlike circular or rectangular geometries, the sound attenuation in elliptical ducts has not been completely studied. The present work will focus on deriving TL in such geometries with various inlet/outlet configurations using analytical methods such as the Green's function method or the mode matching method. Through the implementation of these methods, the effects of various higher–order modes on sound attenuation characteristics will be clarified. In most muffler applications, duct extends are used to attain better sound attenuation. The analytical model of such configuration for a cylindrical geometry has been reported in the literature; similar work for an elliptical chamber is lacking. The present work will devise a boundary perturbation method to determine TL in elliptic chamber mufflers with extended ducts. The perturbation method will first be implemented to determine TL in an elliptic chamber for various inlet and outlet configurations (without duct extends); comparison with exact solutions will help in determining the limitations of the method. The breakout noise from elliptical chamber has not been extensively studied. It was observed in the literature review that distortion in cylindrical duct resulted in sound attenuation characteristics significantly different from undistorted geometry. In order to gain a better insight to this problem, the breakout noise from a finite elliptic chamber will be studied. The effect of structure–acoustic coupling on breakout noise will be analyzed. In many muffler applications, such as in reciprocating compressors, two–phase fluid might exist in the chamber. The effect on the propagation speed due to the presence of two–phase has been extensively studied in prior works. However, very few works have been reported on the study of sound attenuation in shells containing such two–phase mixtures. Therefore, the present work will also focus on deriving the sound attenuation in a chamber containing two–phase fluids.

1.2.2 Statement of objectives

The objectives of the current research include the following:

- Study of sound attenuation in elliptic chamber mufflers using Green's function method, accounting for various inlet/outlet port locations.
- Extend Green's function method for mufflers having multiple inlets and outlets: Development of analytical model for both circular chamber mufflers as well as elliptical mufflers; comparison of sound attenuation in these two geometries.
- Develop a perturbation method to determine sound attenuation in slightly distorted cylindrical chamber mufflers.
- Extend the perturbation method to study the sound attenuation in moderately eccentric elliptical mufflers with extended inlet/ outlet ports.
- Study the sound radiation from an elliptical duct due to structure–acoustic coupling.
- Develop simple model for sound attenuation in ducts containing two–phase fluid.

1.3 Organization of the thesis

In chapter 2, analytical formulation for the evaluation of the TL in a regular reactive muffler is presented. The word regular implies to geometries for which the Helmholtz equation is solvable by using the method of separation of variables. The three–dimensional Helmholtz equation is solved in such domains, and a Green's function method or a mode matching method is utilized for deriving the TL. transmission loss for multiple inlet and outlets are derived as an extension of the existing method. The influence of various inlet and outlet port location on the TL as well as the relative phase between the incoming fluids are characterized.

In chapter 3, a perturbation–based approach is implemented in order to derive the TL in slightly distorted cylindrical chamber mufflers. Using the method of strained parameters, the eigensolutions to the Helmholtz equation is derived for a perturbed geometry. The eigenvectors are orthogonal up to the order of truncation, implying that the Green's function method employed in chapter 2 can be utilized to study the TL in such distorted geometries. The perturbed results are compared to exact solutions for a moderately eccentric elliptic chamber muffler. The perturbation–based approach is then implemented for extended chamber elliptic mufflers, for which no analytical solution exists otherwise.

The work on distorted mufflers provides the background for studying the sound radiation from finite distorted shells in the presence of an internal acoustic source. Prior works on circumferential distortions in ducts have demonstrated mode–coupling effects that increase the sound radiation. However, simplifications in the models limited the results to very small distortions only. In chapter 4, by using the perturbed eigensolutions for the acoustic field and a Rayleigh–Ritz formulation for the shell displacement, the coupled structure–acoustic response for a moderately eccentric elliptic shell of finite length is derived. The effects of the wall distortion on the radiated sound field is analyzed. The final section of the dissertation examines the effect of a liquid layer on the sound attenuation in a muffler. Chapter 5 summarizes the key contributions of this work.

Chapter 2

Analytical formulation of the transmission loss

A Green's function solution method is implemented to study sound attenuation in single-inlet/ double-outlet (SIDO) and double-inlet/single-outlet (DISO) circular and elliptic chamber mufflers. The mufflers are modeled as piston–driven rigid chambers containing a stationary fluid. The pistons are assumed to perform simple harmonic motion with uniform velocities. Velocity potential in the chamber is derived as a superposition of three dimensional velocity potential due to each piston. Pressure field in the chamber is calculated from the velocity potential through conservation of linear momentum equation. Acoustic pressure acting on each piston is calculated by averaging over the surface of the piston. Transmission loss (TL) is evaluated from incident and transmitted acoustic energy. TL curves for various inlet/outlet orientations derived from this method are validated with results obtained from the literature. The effect of locations of inlet/outlet on TL is studied.

2.1 Analytical determination of the TL

The acoustical performance of a muffler is usually expressed in terms of (i) Insertion loss (IL) or (ii) Transmission loss (TL). The IL is defined as the difference (on a logarithmic scale) in the transmitted power from the source to the receiver with and without the muffler in the transmission line. The IL depends on the sound power radiated from the source, and is specific to a particular system only. Although the IL is a better metric for quantifying the acoustic performance of the whole transmission system, it is not useful from research perspective. The transmission loss (TL) is defined as the difference (on a logarithmic scale) between the incident and the transmitted energy at the muffler proper, keeping an anechoic termination. The TL of a muffler is independent of the source of sound, providing a useful metric for comparing different mufflers. It is for this reason that in subsequent sections, TL has been chosen to characterize the performance of a muffler.

The analysis of a muffler requires the solution of the wave equation within the muffler domain. A linearized from of the wave equation is usually employed for most analytical formulation. Alfredson and Davis [65] studied the wave steepening and the onset of a shock due to a finite wave propagation inside a cavity. They observed that the for a sinusoidal wave of sound pressure level $\sim 167\ dB$, the shock distance was close to 4.5 m at a frequency of 500 Hz. In most muffler applications, the sound pressure level are usually much lower $(130 - 140\ dB)$ than the above, implying that the non–linear effects may be neglected in the mathematical formulation.

A further simplification to the linearized wave equation is made by neglecting any viscous effects. Pierce [66] derived the relations for the vorticity and the entropy–mode–fields boundary layers (see Eq. 10–4.2 in [66]). In most muffler application, the physical dimension of the muffler and the ports (source) are such that these boundary layers are of much smaller orders of magnitude ($\sim 10^{-3}$). Hence by overlooking the viscous effects, the error in the derived field variable is negligible.

2.1.1 Green's function method (GFM)

The linearized wave equation with an arbitrary boundary condition and in absence of any source and viscous effects can be written in terms of velocity potential $\varphi(\vec{x}, t)$ as:

$$\bigtriangledown^2 \varphi(\vec{x}, t) - \frac{1}{c^2} \frac{\partial^2 \varphi(\vec{x}, t)}{\partial t^2} = 0 \tag{2.1}$$

Assuming harmonic time behavior, the velocity potential may be written as:

$$\varphi(\vec{x}, t) = \varphi(\vec{x}) \exp(j\omega t) \tag{2.2}$$

By substituting Eq. (2.2) into Eq. (2.1), the wave equation yields:

$$\bigtriangledown^2 \varphi(\vec{x}) + k^2 \varphi(\vec{x}) = 0 \tag{2.3}$$

Here $k(= \omega/c)$ is the wave number. The acoustic pressure and velocity are related to velocity potential by:

$$\begin{aligned} P(\vec{x}, t) &= -\rho \frac{\partial \varphi(\vec{x}, t)}{\partial t} = -j\rho\omega\varphi(\vec{x}, t) \\ \vec{u}(\vec{x}, t) &= \bigtriangledown \varphi(\vec{x}, t) \end{aligned} \tag{2.4}$$

For the present problem, the walls of the muffler are assumed to be rigid implying that the normal component of velocity at the surface is zero except at inlets and at outlets. The inlets and outlets are assumed to be uniform velocity piston sources performing simple harmonic motion. Therefore, the present problem can be classified as a homogeneous wave problem with inhomogeneous Neumann boundary conditions. Accordingly, the Green's function for the problem can be defined as a solution to the following inhomogeneous problem with a homogeneous Neumann boundary condition [17]:

$$\begin{aligned} &\bigtriangledown^2 G(\vec{x}/\vec{x}_0) + k^2 G(\vec{x}/\vec{x}_0) = -\delta(\vec{x} - \vec{x}_0) \\ &\bigtriangledown G(\vec{x}/\vec{x}_0) \cdot \vec{\eta}|_S = 0 \end{aligned} \tag{2.5}$$

The solutions to the eigenvalue problem defined by Eq. (2.3) form an orthogonal basis. Hence, it is possible to write the Green's function as a series expansion of the eigenfunctions [67]:

$$G(\vec{x}/\vec{x}_0) = \sum_{n=0}^{\infty} \frac{\varphi_n(\vec{x})\varphi_n(\vec{x}_0)}{(k_n^2 - k^2)\int_V \varphi_n(\vec{x})^2 dV} \tag{2.6}$$

Here k_n is eigenfrequency of the nth mode. Using Green's second identity yields:

$$\int_{V_0} \left(\varphi(\vec{x}_0) \bigtriangledown^2 G(\vec{x}/\vec{x}_0) - G(\vec{x}/\vec{x}_0) \bigtriangledown^2 \varphi(\vec{x}_0)\right) dV_0 = \int_{S_0} \left(\varphi(\vec{x}_0) \bigtriangledown G(\vec{x}/\vec{x}_0) - G(\vec{x}/\vec{x}_0) \bigtriangledown \varphi(\vec{x}_0)\right) \cdot d\vec{S}_0 \tag{2.7}$$

By substituting Eq. (2.3) and Eq. (2.5) into Eq. (2.7), and by using reciprocity property, the above equation can be simplified to:

$$\varphi(\vec{x}) = \int_{S_0} G(\vec{x}/\vec{x}_0) \bigtriangledown \varphi(\vec{x}_0) \cdot \vec{\eta} dS_0 \tag{2.8}$$

From the initial assumption that normal component of velocity at the surface of the muffler is zero everywhere except at the piston surfaces, Eq. (2.8) can be written as:

$$\varphi(\vec{x}) = \sum_{i=1}^{m} \frac{1}{S_i} \int_{S_{i0}} G(\vec{x}/\vec{x}_0) \vec{U}_i \cdot \vec{\eta} dS_{i0} \tag{2.9}$$

where, the summation is over m pistons. The ith piston has a surface area S_i and a volume velocity $\vec{U}_i$. For the inlet piston, $\vec{U}_i \cdot \vec{n}$ is negative, and for the outlet piston $\vec{U}_i \cdot \vec{n}$ is positive.

2.1.2 Mode Matching Method (MMM)

The mode matching method relies on the solution of the Helmholtz equation at each region of the muffler discontinuities (inlet ports, outlet ports, chamber). By establishing the continuity of the acoustic pressure and velocity at the interface between two discontinuities, the complete solution of the field variable is possible. A complete description of the method is available in the literature [19, 23, 24]. In order to maintain continuity, a brief summary of the method is presented in the next few paragraphs.

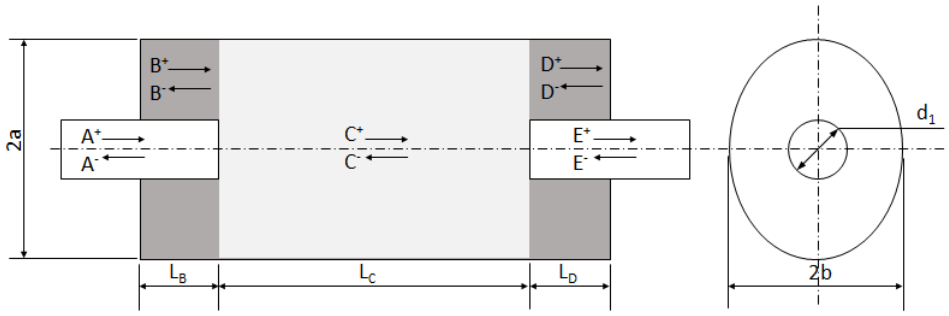

Figure 2.1: Schematic of an extended tube muffler with elliptic chamber.

Consider an extended tube muffler as shown in Fig. 2.1. The inlet and the outlet ports of the muffler are cylindrical in shape. The entire muffler domain can be divided into five zones $A - E$. It is assumed that the incoming wave A^+ is planar. By symmetry, acoustic transverse modes that are symmetric about both the axes of the muffler can only propagate above their cutoff frequency. For the cylindrical and elliptic chamber, the eigenfunctions of the *cosine* type (though not all of them) share such symmetric properties. It is for this reason that the eigenfunctions of the *sine* type are not relevant in the present formulations, and will not be considered further. Assuming harmonic–time dependence the pressure field in each zone Q may therefore be expressed as a series expansion involving all the possible solutions, and truncated to a suitable order (N, M):

$$P_Q(r,\theta,z) = \sum_{n=0}^{N}\sum_{m=1}^{M} Q_{nm}^{+}\exp(-jk_{nm,Q}z)\phi_{nm}(r,\theta;Q) + \sum_{n=0}^{N}\sum_{m=1}^{M} Q_{nm}^{-}\exp(jk_{nm,Q}z)\phi_{nm}(r,\theta;Q); \tag{2.10}$$

At each region $A - E$, ϕ_{nm} needs to be derived based on the geometry. The acoustic velocity at the ports is expressed in terms of the acoustic pressure as:

$$U_Q(r,\theta,z) = -\frac{1}{j\rho\omega}\frac{\partial P_Q}{\partial z}; \qquad Q = A, B, etc., \tag{2.11}$$

At the interface between the ports and the chamber, the continuity of acoustic pressure and velocity is expressed as:

$$P_A = P_C \ \ (\text{on } S_A); \quad P_B = P_C \ \ (\text{on } S_B); \quad P_C = P_D \ \ (\text{on } S_D); \quad P_C = P_E \ \ (\text{on } S_E); \tag{2.12}$$

$$U_A = U_C \ \ (\text{on } S_A); \quad U_B = U_C \ \ (\text{on } S_B); \quad U_C = U_D \ \ (\text{on } S_D); \quad U_C = U_E \ \ (\text{on } S_E); \tag{2.13}$$

Instead of Eq. (2.12) and Eq. (2.13), a more useful form of the continuity conditions are obtained from Eqs. (2.10)-(2.13) by normalizing the equations with the eigenfunctions, and by using the orthogonality properties of the eigenfunctions. As an example, Eq. (2.12) is first multiplied by $\phi_{pq}(r,\theta;A)$ and then the product is integrated over the surface of inlet port S_A. From the orthogonality of the eigenfunctions, the resulting product de-couples the r.h.s. By repeating the same procedure for all $p \in N$, $q \in M$, yields the following $(N+1)M$ number of simultaneous equations involving $(A^+_{nm}, A^-_{nm}, C^+_{nm}, C^-_{nm})$:

$$\begin{aligned} &\left(A^+_{pq} + A^-_{pq}\right) \left\langle \phi^2_{pq}(r,\theta;A) \right\rangle_{S_A} = \sum_{n=0}^{N} \sum_{m=1}^{M} \left(C^+_{nm} + C^-_{nm}\right) \left\langle \phi_{nm}(r,\theta;C) \phi_{pq}(r,\theta;A) \right\rangle_{S_A} \\ &\text{where, } p = 0,1,2,...,N; \quad q = 1,2,3,...,M \end{aligned} \tag{2.14}$$

Similarly, the other normalized continuity conditions may be derived from Eq. (2.12) and Eq. (2.13). In total, six equations similar to Eq. (2.14) are obtained for the present muffler configurations. Therefore, a total of $6(N+1)M$ simultaneous equations are derived. It is assumed that the incoming pressure wave is planar with unit magnitude, and that the exit port of the muffler has anechoic termination; hence, $E^-_{nm} = 0$. If the endplates are assumed to be rigid, an additional $2(N+1)M$ equations from the boundary conditions are obtained:

$$\begin{aligned} &U_B|_{z=-L_B} = 0; && U_D|_{z=L_D} = 0; \\ &\text{or, } B^+_{nm} = B^-_{nm} \exp\left(-2jk_{nm,B}L_B\right); && \text{or, } D^+_{nm} = D^-_{nm} \exp\left(2jk_{nm,D}L_D\right); \end{aligned} \tag{2.15}$$

Solving for the $8(N+1)M$ simultaneous equations involving $(A^-_{nm}, B^+_{nm}, B^-_{nm}, C^+_{nm}, C^-_{nm}, D^+_{nm}, D^-_{nm}, E^-_{nm})$, yields the complete pressure and velocity field within the muffler domain. Finally, the TL is derived as:

$$TL = 20 \log_{10} \left| \frac{d_2}{d_1} \sum_{n=0}^{N} \sum_{m=1}^{M} E^+_{nm} \exp(-jk_{nm,E}L_E) \right| \tag{2.16}$$

2.1.3 Comparison between the GFM and the MMM

In the GFM, it is assumed that the particle velocity is uniform at the inlet and the outlet ports. This assumption implies that for each incident plane–wave at the inlet port, the reflected waves are also planar. Similarly, at the outlet port, the outgoing wave should also be a plane–wave in order to satisfy the above assumption. In the MMM, these conditions may be realized by setting the higher order coefficients $A_n^-,\ n > 0$ and $E_n^+, n > 0$ to zero. Therefore, the GFM may be imagined as a simplification of the MMM for geometries where both the methods are applicable. From Fig. 2.2 it may be observed that the particle velocity at the inlet port is almost uniform when the above restrictions are imposed on the MMM, validating the equivalence with the GFM. In Figs. 2.3–2.4, TL curves derived from the MMM (with and without the restrictions on the coefficients) are compared with the GFM. At smaller duct–length the evanescent higher–order modes have non–negligible effect on the TL curves, causing a difference in the TL. The differences in the TL curves diminish as the length of the muffler is increased. It may be noted that the TL curve obtained from the GFM overlaps with that obtained from the MMM (with restrictions on the coefficients).

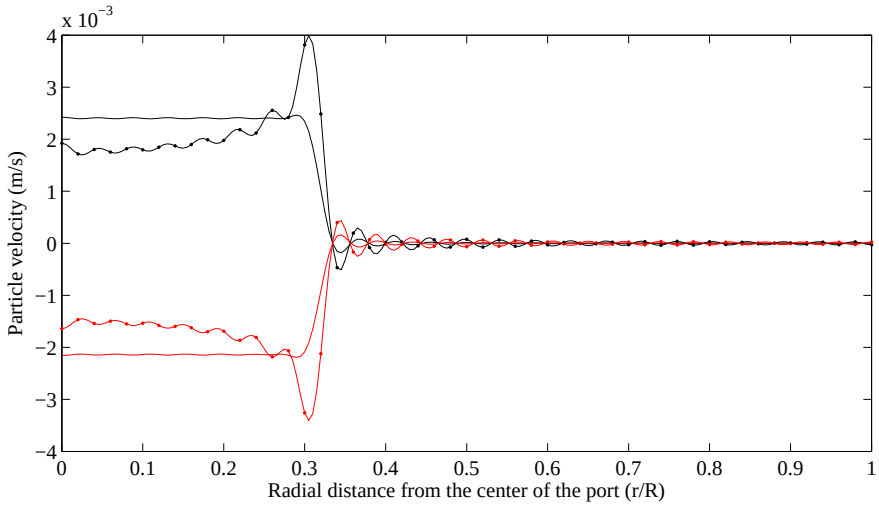

Figure 2.2: Particle velocity along a radial line at the inlet port surface of a cylindrical expansion chamber muffler. Black: real part; Red: imaginary part; -·-·-·- MMM; ——— MMM with $(A_n^-, n > 0)$ and $(E_n^+, n > 0)$ equal to zero; ratio of inlet to chamber diameter is 0.31

For inlet/outlet ports that are located at the side of the muffler, the MMM is not applicable because the shell eigenfunctions $\phi(r, \theta)$ cannot consistently satisfy the velocity conditions at the ports and at the shells. The GFM, avoids such drawbacks by incorporating the effects of

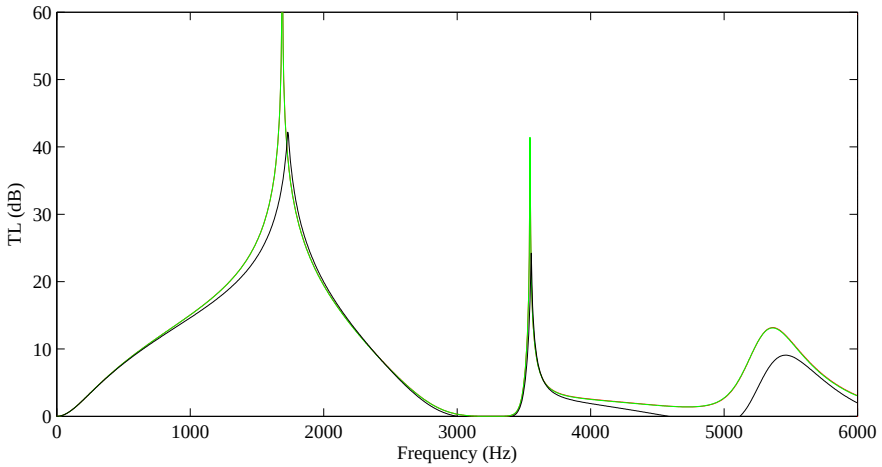

Figure 2.3: Comparison of the TL using the GFM and the MMM for chamber length, $L = 0.05\ m$. Black: MMM; Green: MMM with $(A_n^-, n > 0)$ and $(E_n^+, n > 0)$ equal to zero; Red: GFM. Red and Green are overlapped

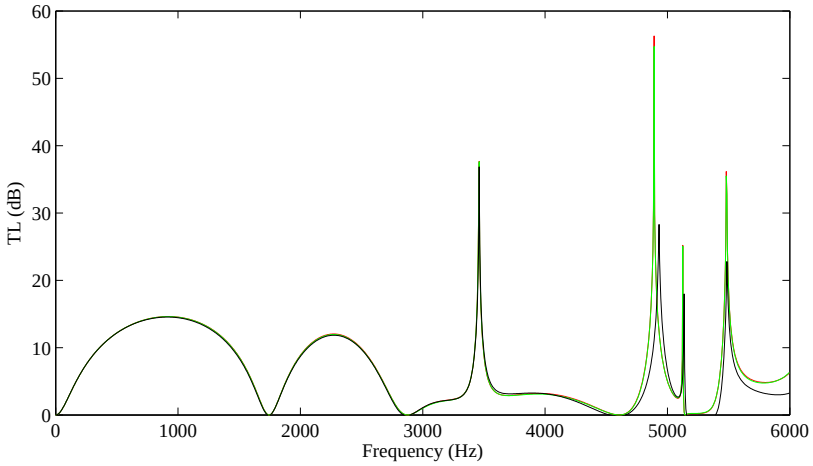

Figure 2.4: Comparison of the TL using the GFM and the MMM for chamber length, $L = 0.10\ m$. Black: MMM; Green: MMM with $(A_n^-, n > 0)$ and $(E_n^+, n > 0)$ equal to zero; Red: GFM. Red and Green are overlapped

surface velocity by using the Green's identities. However, the GFM is not suitable for extended chamber mufflers due to the inhomogeneity inside the muffler domain. An alternative method for deriving the scattered field by two–dimensional inhomogeneous dielectric bodies, known as the Recursive Green's function method (RGFM) was proposed by Jensen and Freeze [68]. In this approach, the Green's function at individual sub–domains of an inhomogenous medium are recursively combined in order to obtain the field variable in the entire domain. At higher–dimensions, this method becomes excessively difficult to construct, and is not suitable for the present formulation.

2.2 Extension of GFM for mufflers with multiple inlet/outlet ports

In many applications, mufflers with multiple inlet and outlet ports are commonly employed. The expansion chamber with two inlets and one outlet is a practical configuration which may be used in the exhaust system of reciprocating engines to merge two gas streams into one common tailpipe [69]. Similarly, by using multiple outlets, detrimental effects of backpressure on the performance of an engine may be reduced. In order to study the sound attenuation in such multi–port chambers, the GFM is utilized in this section.

The average pressure on each piston can be obtained from Eq. (2.4) and Eq. (2.9) as:

$$\begin{aligned} P_k &= -\frac{j\rho\omega}{S_k}\int_{S_k}\varphi(\vec{x})dS_k \\ &= -j\rho\omega\sum_{i=1}^{m}\frac{1}{S_iS_k}\int_{S_k}\int_{S_{i0}}G(\vec{x}/\vec{x_0})\vec{U}_i\cdot\vec{\eta}dS_{i0}dS_k; \quad k=1,2,\cdots,m \end{aligned} \tag{2.17}$$

In a matrix form, the above equations can be written as:

$$\begin{Bmatrix} P_1 \\ P_2 \\ \vdots \\ P_m \end{Bmatrix} = \begin{bmatrix} A_{11} & A_{12} & \cdots & A_{1m} \\ A_{21} & A_{22} & \cdots & A_{2m} \\ \vdots & \vdots & \vdots & \vdots \\ A_{m1} & A_{m2} & \cdots & A_{mm} \end{bmatrix} \begin{Bmatrix} \vec{U}_1\cdot\vec{\eta} \\ \vec{U}_2\cdot\vec{\eta} \\ \vdots \\ \vec{U}_m\cdot\vec{\eta} \end{Bmatrix} \tag{2.18}$$

where, A is the impedance matrix given by:

$$A_{pq} = -\frac{j\rho\omega}{S_pS_q}\int_{S_p}\int_{S_{q0}}G(\vec{x}/\vec{x_0})dS_{q0}dS_p; \quad p,q=1,2,\cdots,m \tag{2.19}$$

2.2.1 Determination of TL for the SIDO configuration.

For SIDO configuration, the inlet is denoted by subscript 1. The outlets are denoted by subscripts 2 and 3, respectively. Assuming anechoic termination, acoustic pressure at the outlet pistons can be written as:

$$P_2 = U_2Z_2; \qquad P_3 = U_3Z_3; \qquad Z_i = \rho c/S_i \tag{2.20}$$

Also, $\vec{U_1} \cdot \vec{n} = -U_1$, $\vec{U_2} \cdot \vec{n} = U_2$, and $\vec{U_3} \cdot \vec{n} = U_3$. Substituting Eq. (2.20) into Eq. (2.18) yields:

$$\begin{Bmatrix} P_1 \\ 0 \\ 0 \end{Bmatrix} = \begin{bmatrix} -A_{11} & A_{12} & A_{13} \\ -A_{21} & A_{22} - Z_2 & A_{23} \\ -A_{31} & A_{32} & A_{33} - Z_3 \end{bmatrix} \begin{Bmatrix} U_1 \\ U_2 \\ U_3 \end{Bmatrix} \tag{2.21}$$

or,

$$P = [A]\{\vec{U} \cdot \vec{n}\}$$

The volume velocity vector $\vec{U}$ may be expressed in terms of P_1 by taking the inverse of the impedance matrix. The incident sound power is expressed as [3]:

$$W_{int} = \frac{1}{2Z_1} \left| \frac{P_1 + Z_1 U_1}{2} \right|^2 \tag{2.22}$$

Similarly, the transmitted power is given by:

$$W_{tr} = \frac{1}{2Z_2} |Z_2 U_2|^2 + \frac{1}{2Z_3} |Z_3 U_3|^2 \tag{2.23}$$

Therefore, using Eqs. 2.21–2.23, the transmission loss can be derived as:

$$TL = 10 \log_{10} \left(\frac{W_{int}}{W_{tr}} \right) \tag{2.24}$$

2.2.2 Determination of TL for the DISO configuration.

For DISO configuration, inlets are denoted by subscripts 1 and 2, respectively. The outlet is denoted by subscript 3. Similar to SIDO configuration, acoustic pressure at the ports is related to velocity as:

$$\begin{Bmatrix} P_1 \\ P_1/P_R \\ 0 \end{Bmatrix} = \begin{bmatrix} -A_{11} & -A_{12} & A_{13} \\ -A_{21} - \frac{Z_1}{P_R} & -A_{22} + Z_2 & A_{23} \\ -A_{31} & -A_{32} & A_{33} - Z_3 \end{bmatrix} \begin{Bmatrix} U_1 \\ U_2 \\ U_3 \end{Bmatrix} \tag{2.25}$$

or,

$$P = [A]\{\vec{U} \cdot \vec{n}\}$$

Here, $P_R = p_1^+/p_2^+$, where p_1^+ and p_2^+ are the strength of incoming waves at ports 1 and 2, respectively [69]. Again, taking inverse of coefficient matrix of U, volume velocities can be expressed in terms of P_1 and P_R. Finally the TL may be derived as:

$$TL = 10\log_{10}\left(\frac{|P_1 + U_1 Z_1|^2 \left\{S_1 + \frac{S_2}{|P_R|^2}\right\}}{4|U_3 Z_3|^2 S_3}\right) \tag{2.26}$$

2.3 Validation: cylindrical geometries

The analytical model outlined in the previous section can be implemented for any muffler having a regular geometry, viz. rectangular, circular, or elliptic. In this chapter, mufflers having circular and elliptic cross–sections have been considered. The eigenfunctions and the eigenfrequencies for a circular chamber are given by:

$$\begin{aligned} &\varphi_j = A_{mn} J_m(k_{mn}^r r)\cos(m\theta)\cos(p\pi z/L) + B_{mn} J_m(k_{mn}^r r)\sin(m\theta)\cos(p\pi z/L) \\ &k_m^2 = (k_{mn}^r)^2 + (p\pi/L)^2; \qquad m, p = 0, 1, 2, \cdots; \qquad n = 1, 2, \cdots \end{aligned} \tag{2.27}$$

For $m > 0$, the eigenfunctions are degenerate due to symmetry of the circular geometry. Here j is an index which corresponds to a unique combination of circumferential, radial, and longitudinal modes m, n, and p, respectively. L is the axial length of the muffler. The radial wave number is obtained from rigid wall boundary condition:

$$\begin{aligned} &\left.\frac{\partial \varphi}{\partial r}\right|_{r=R} = 0 \\ &or, \\ &J_m'(k_{mn}^r R) = 0 \end{aligned} \tag{2.28}$$

Determination of impedance matrix A requires evaluation of the integral of eigenfunctions over the surface of the piston. Each piston can have one of the three possible orientations: (i) end-center inlet/outlet (ii) end-offset inlet/outlet (iii) side-inlet/outlet. The impedance matrix for any possible combinations of muffler orientations is a function of these three integrals only. Thus, the Green's function solution method is very flexible, as any possible inlet/outlet orientations can be studied by evaluating any/all of these three integrals. It must be noted that the intersection of circular piston on the shell would result in an elliptical cross section. However, in order to

simplify the integration, an equivalent (having same area of cross section as the circular piston) rectangular piston has been assumed.

The present method was validated using the works reported by Selamet *et al*., [70, 69]; the geometry of SIDO and DISO muffler considered in their work is shown in Fig. 2.5. For SIDO configuration, inlet (denoted by subscript 1) and outlets (denoted by subscripts 2 and 3) are located at end face of the muffler. The DISO muffler has end inlets (1 and 2) and a side outlet (3). A comparison of present work with results obtained by Selamet *et al*., [70, 69] is shown in Figs. 2.6–2.8. From Fig. 2.7 and Fig. 2.8, it can be observed that an excellent agreement between the present method and the MMM is achieved for an acoustically long muffler with both SIDO and DISO configurations. For the acoustically short chamber, the shift in the resonating peaks in Fig. 2.6 is consistent with the observations made in the previous section. From Fig. 2.8 it can be concluded that by replacing actual section of the piston with an equivalent rectangular section does not cause significant departure from BEM results.

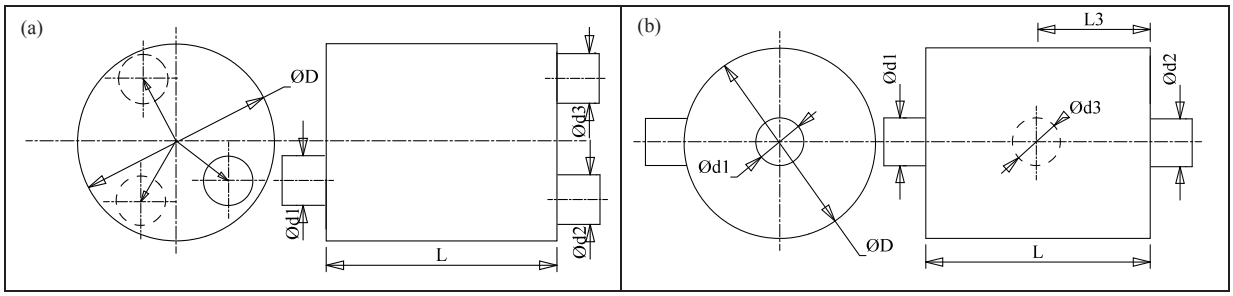

Figure 2.5: Schematic of the mufflers used for validation of the present method [70, 69]; (a) SIDO muffler: $D = 0.153\ m$, $d_1 = d_2 = d_3 = 0.0486\ m$ (b) DISO muffler: $D = 0.153\ m$, $L = 0.54\ m$, $d_1 = d_2 = 0.0486\ m$, $d_3 = 0.0584\ m$

2.3.1 Parametric study: SIDO mufflers

The effects of locations of inlet/outlet on overall muffler performance are examined in this section. In view of the fact that many combinations of inlet/outlet orientations are possible, only a few interesting results are presented. The various inlet/outlet muffler orientations are shown in Fig. 2.9. The diameter of the chambers and the ports were selected to be same as in prior work [15, 16].

The TL curve for the muffler geometry given by Fig. 2.9(a) is shown in Fig. 2.10. The length of the muffler is $L = 0.30\ m$. The offset distance is which corresponds to the pressure nodal radius

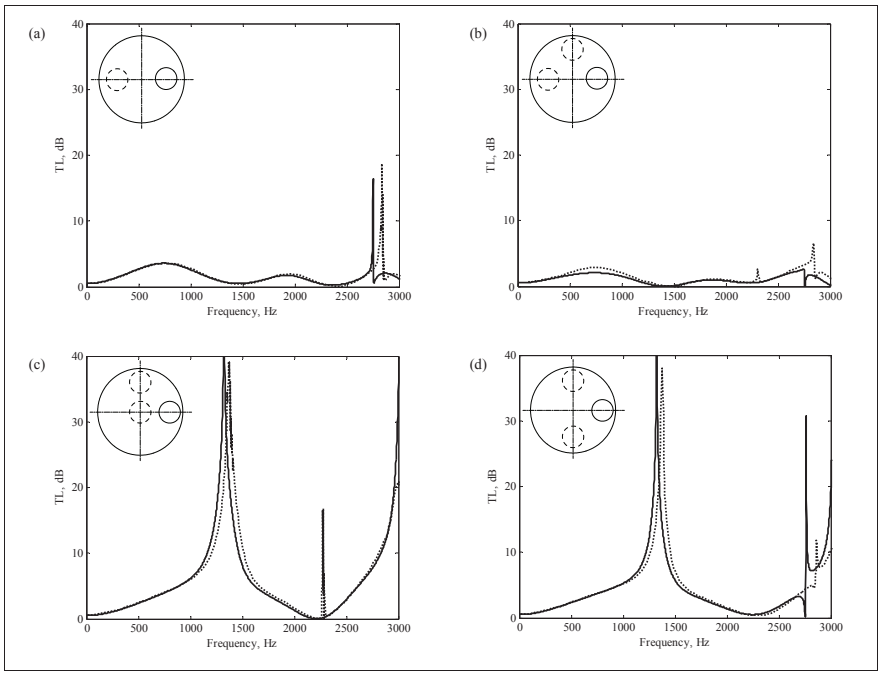

Figure 2.6: TL curve for SIDO mufflers with circular cross section of the chamber, $L/D = 0.205$: —— GFM; $\cdots\cdots$ Selamet and Ji [70] (a) $\delta_1 = \delta_2 = \delta_3 = 0.051\ m,\ \varphi_1 = \varphi_2 = 0,\ \varphi_3 = \pi$ (b) $\delta_1 = \delta_2 = \delta_3 = 0.051\ m,\ \varphi_1 = 0,\ \varphi_2 = \pi/2,\ \varphi_3 = \pi$ (c) $\delta_1 = \delta_2 = 0.051\ m,\ = \delta_3 = 0\ m,$ $\varphi_1 = 0,\ \varphi_2 = \pi/2,\ \varphi_3 = 0$ (d) $\delta_1 = \delta_2 = \delta_3 = 0.051\ m,\ \varphi_1 = 0,\ \varphi_2 = \pi/2,\ \varphi_3 = 3\pi/2$

of $(0, 2)$ mode. The distance of side-outlet from the inlet is $L3 = L/2$. For comparison, TL curves for mufflers having end-center inlet/side-outlet, and having end-center inlet/end-offset outlet have been shown in the figure. From the figure, TL for SIDO muffler is lower than for other two configurations. This result is expected, because an additional outlet port in SIDO muffler causes transmission of extra energy. In the plane–wave limit, for comparable geometries with similar port orientations, the addition of an extra outlet doubles the transmitted energy. The doubling of the transmitted energy results in a 3 dB drop in TL.

The diametral modes in all the three configurations are suppressed due to inlet being located at end-center of the muffler. Therefore, one–dimensional dome behavior is observed in all of the muffler geometries, below the cut-off frequency of first propagating radial (0, 2) mode. Additionally, the location of outlet at the pressure node of (0, 2) mode extends the dome like behavior in end-center inlet/end-offset outlet muffler up to the cut-off frequency $f = 6333\ Hz$ of the next higher–order (0, 3) mode. In the GFM, by conveniently positioning the inlet/outlet ports such that the port's axis of symmetry coincide with the nodal diameter, yields a zero averaged pressure over the surface of the port for that particular mode (Eq. (2.17)). In terms of energy,

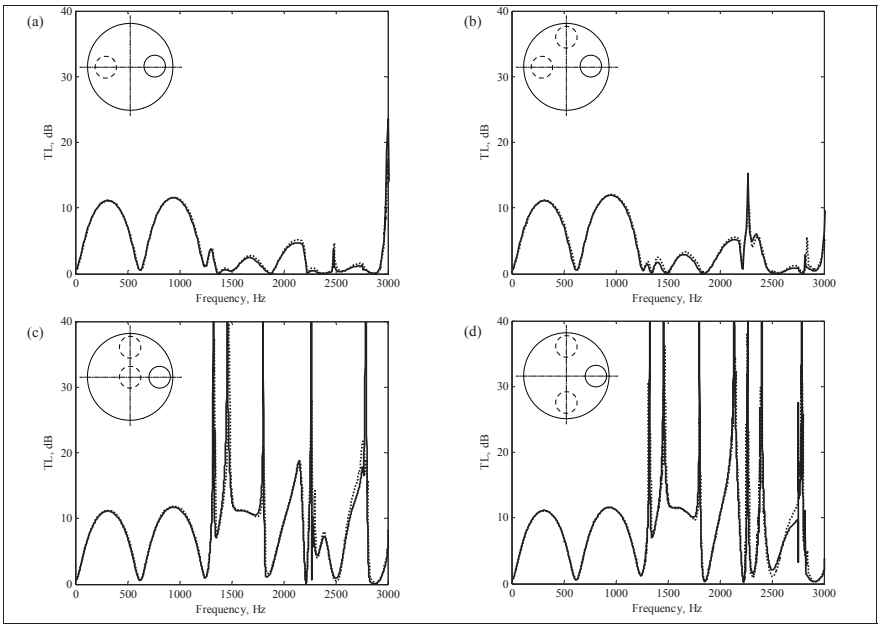

Figure 2.7: TL curve for SIDO mufflers with circular cross section of the chamber, $L/D = 1.84$: —— GFM; $\cdots\cdots$ Selamet and Ji [70] (a) $\delta_1 = \delta_2 = \delta_3 = 0.051\ m,\ \varphi_1 = \varphi_2 = 0,\ \varphi_3 = \pi$ (b) $\delta_1 = \delta_2 = \delta_3 = 0.051\ m,\ \varphi_1 = 0,\ \varphi_2 = \pi/2,\ \varphi_3 = \pi$ (c) $\delta_1 = \delta_2 = 0.051\ m,\ = \delta_3 = 0\ m,\ \varphi_1 = 0,\ \varphi_2 = \pi/2,\ \varphi_3 = 0$ (d) $\delta_1 = \delta_2 = \delta_3 = 0.051\ m,\ \varphi_1 = 0,\ \varphi_2 = \pi/2,\ \varphi_3 = 3\pi/2$

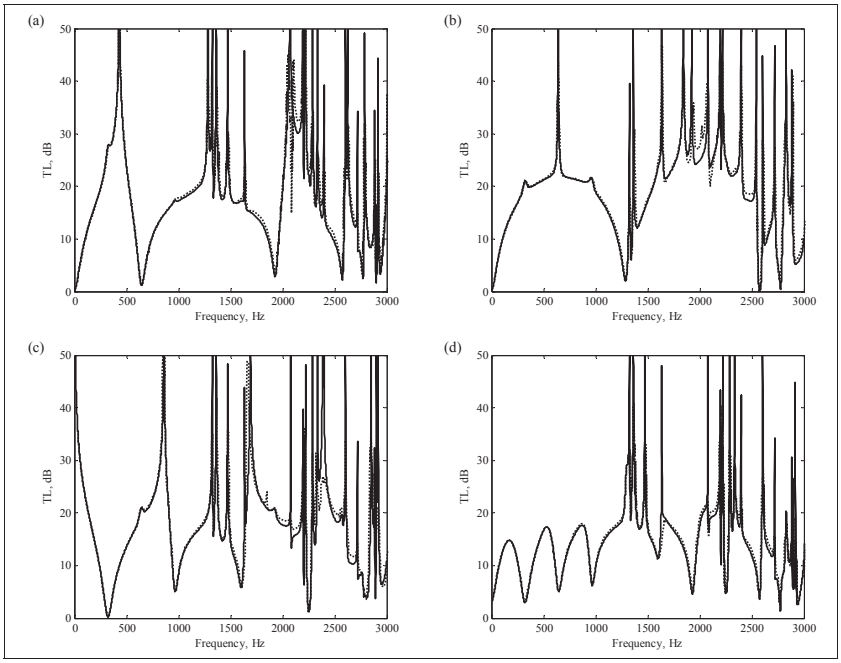

Figure 2.8: TL curve for DISO mufflers with circular cross section of the chamber: —— GFM; $\cdots\cdots$ Selamet and Ji [69] (a) $L_3 = L/8,\ P_1^+/P_2^+ = 1$ (b) $L_3 = 2L/8,\ P_1^+/P_2^+ = 1$ (c) $L_3 = L/8,\ P_1^+/P_2^+ = -1$ (d) $L_3 = L/8,\ P_1^+/P_2^+ = 1i$

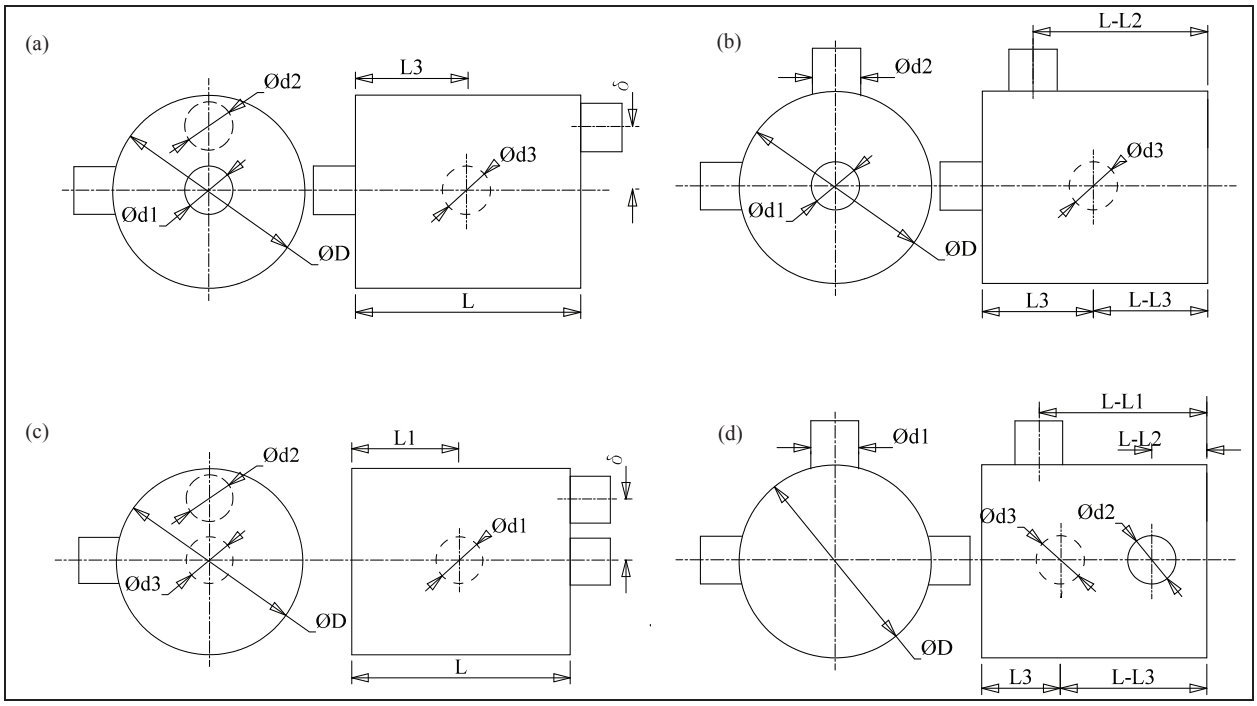

Figure 2.9: Schematic of various SIDO muffler orientations. $L = 0.30\ m$, $D = 0.122\ m$

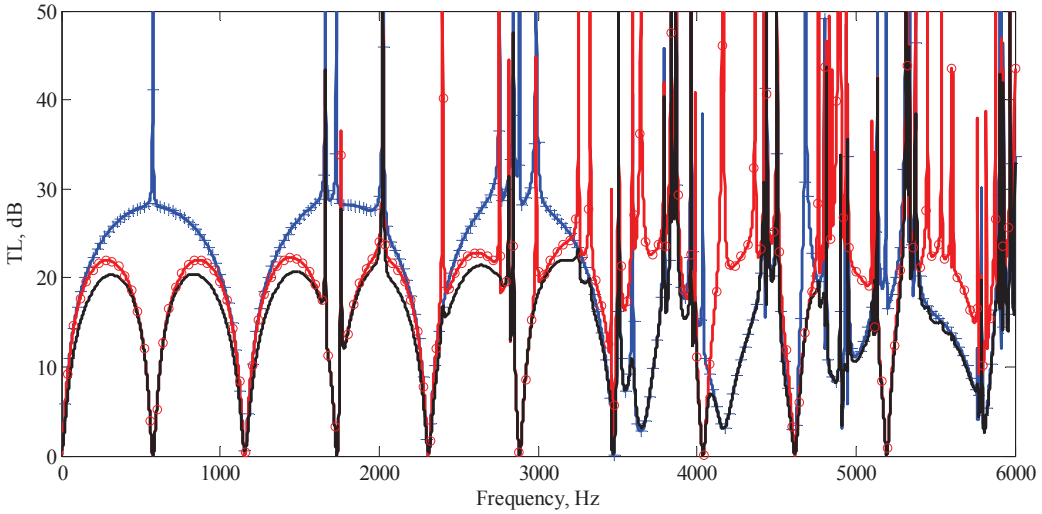

Figure 2.10: TL comparison of mufflers having inlet/outlets as shown in Fig. 2.9(a). $L_3 = L/2,\ \delta = 0.6276R$; ——— SIDO muffler, $d_1 = d_2 = d_3 = D/5$; –o–o–o– End-inlet/end-offset outlet muffler, $d_1 = d_2 = D/5,\ d_3 = 0$; –+–+–+– End-inlet/side-outlet muffler, $d_1 = d_3 = D/5,\ d_2 = 0$

the net energy flux due to this mode is therefore zero, and no observable effects are seen in the TL . Alternatively, the port may be imagined as an infinite number of monopole sources, with the nodal diameter separating the opposing sources. Using the phase–cell cancellation analogy

[44, 50], the adjacent cells of opposite phases cancel and potentially the boundary cells only contribute towards the energy flux. Therefore, the strength of this boundary dipole source is extremely weak and is considered to be absent.

For the end-center inlet/side outlet muffler, there are pressure minima at the outlet corresponding to the longitudinal mode $p = (2m+1),\ m = 0, 1, 2, \cdots$. These minima explain a resonating peak in the TL curve at frequencies ($(2m+1)c/4(L-L_2)\ Hz$) corresponding to these modes. At $p = 2m$, the inlet as well as the outlet are at pressure maxima, which results in dip in the TL curve. Consequently, the width of one dimensional dome for end-center inlet/side outlet configuration is $f = c/L$, where c is the speed of sound and L is the length of the muffler. The SIDO muffler has one of its outlets at end face of the muffler. The longitudinal mode $p = m,\ m = 0, 1, 2, \cdots$, corresponds to pressure maxima at this outlet, which results in a dip in TL at $f = mc/2L\ Hz$. Unlike end-center inlet/end-offset outlet muffler, in SIDO muffler the propagation of (0, 2) mode is not suppressed because the side outlet of the muffler transmits sound energy corresponding to this mode. Therefore, a dip in TL curve at frequencies higher than the cut-off frequency $f = 3459\ Hz$ of the (0, 2) mode can be observed for the SIDO muffler.

A better insight into the resonating peaks and troughs in the end-center inlet/side outlet muffler may be obtained by studying (within the plane–wave limit) the input impedance at the source (inlet) of the muffler. Using one–dimensional analysis, the input impedance at the source can be derived as:

$$Z_{in} = Z_c \frac{\left[Z_p \cos kL + jZ_c \cos k(L-L_3) \sin kL_3\right]}{\left[jZ_p \sin kL + Z_c \cos k(L-L_3) \cos kL_3\right]} \tag{2.29}$$

where, the subscript p indicates the inlet/outlet ports, c corresponds to the chamber. In the limit as $L_3 \to 0$, the end-center inlet/side outlet muffler may be imagined as a side–branch resonator of length L. The side–branch resonators are characterized by the presence of periodic resonating peaks in the TL curve and are commonly employed for reducing tonal noise. The resonating peaks for such systems correspond to branch lengths which are odd–multiples of a quarter–wavelength, i.e.:

$$L - L_3 = (2m+1)\lambda/4,\ m = 0, 1, 2, \cdots \tag{2.30}$$

where, $\lambda = c/f$. At these frequencies, the input impedance observed by the source is extremely small, causing strong vibration. When $L_3 > 0$, the condition in Eq. (2.30) still yields a local minimum in the input impedance. This observation is verified from Fig. 2.11(a), where the input impedance is plotted against the distance of the outlet port from the rigid–termination end

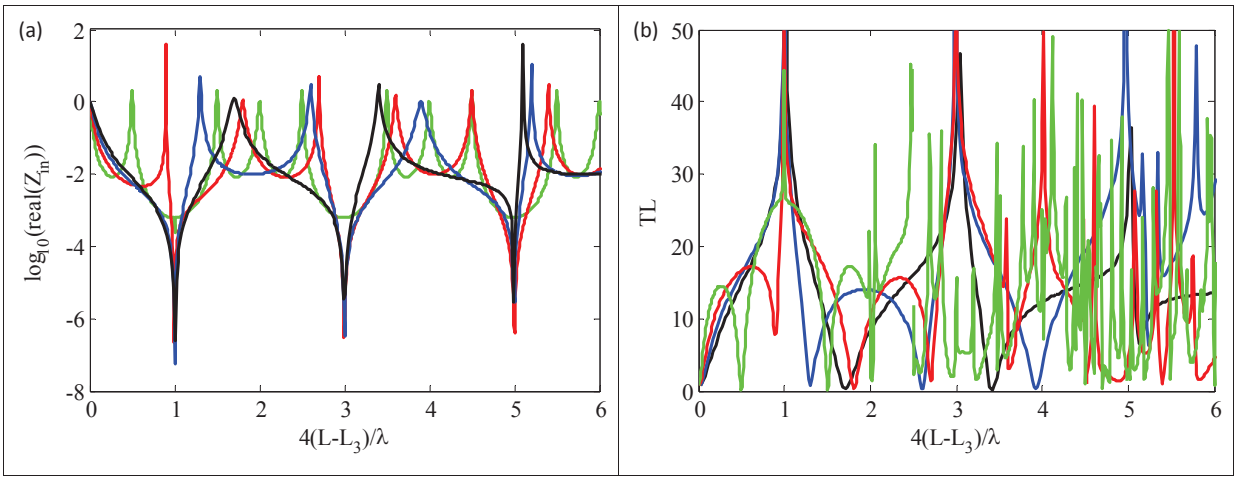

Figure 2.11: Input impedance and TL of an end–inlet/side outlet cylindrical muffler of length $L = 0.30\ m$, $D = 0.122\ m$. The different curves indicate the variation due to the change in the outlet port location L_3; ——, $L_3 = 0.15L$; ——, $L_3 = 0.35L$; ——, $L_3 = 0.55L$; ——, $L_3 = 0.75L$

$(L - L_3)$ for different values of L_3. This distance is normalized w.r.t. $\lambda/4$, such that according to Eq. (2.11), the local minima are observed at $4(L - L_3)/\lambda = 1, 3, 5, \cdots$. The TL curves for identical configurations are plotted in Fig. 2.11(b), with the same normalization on the abscissa. The resonating peaks in the TL validate the observation made in Fig. 2.11(a).

The location of the troughs in the TL in Fig. 2.11(b) may also be explained from Eq. (2.29). The troughs correspond to a condition when the input impedance is same (or atleast of the same order) as the termination impedance Z_p. Under such matched impedance condition, the incident energy is almost entirely transmitted, yielding a zero TL. In the end-center inlet/side outlet muffler, the matched impedance condition is realized for all L_3 when $\sin(kL)$ in the denominator of Eq. (2.29) is zero i.e, $kL = n\pi$, $n = 1, 2, \cdots$, provided that $\cos k(L - L_3) \cos kL_3$ is not zero simultaneously. The denominator remains non–zero for all $L_3/L \neq (2m + 1)/2n$, n, m are integers. In Fig. 2.12, the matched impedance conditioned is observed for different values of L_3. It can be observed that the matched–impedance condition occurs at integer values on the abscissa $(kL/\pi = 1, 2, 3, \cdots)$. The TL curves in Fig. 2.12, correspondingly show a dip at these integer values, except for green curve $(L_3 = 3L/4)$. The green curve in Fig. 2.12 yields a situation at which the denominator in Eq. (2.29) is zero at $kL = 2\pi$, and consequently yielding very high input impedance. The observed results and Eq. (2.29) are valid only in the plane wave–limit.

The SIDO muffler in Fig. 2.9(a) yields a poor TL characteristic compared to end-inlet/side-

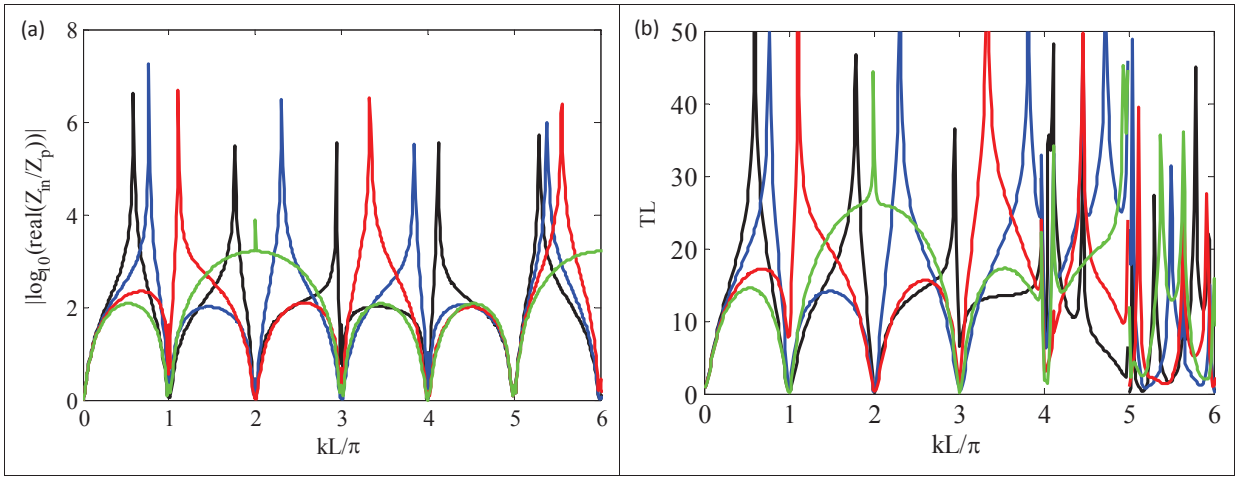

Figure 2.12: Normalized input impedance and TL of an end–inlet/side outlet cylindrical muffler of length $L = 0.30\ m$, $D = 0.122\ m$. The different curves indicate the variation due to the change in the outlet port location L_3; ———, $L_3 = 0.15L$; ———, $L_3 = 0.35L$; ———, $L_3 = 0.55L$; ———, $L_3 = 0.75L$

outlet muffler. Moreover the width of the one dimensional domes for end-inlet/side-outlet muffler is twice as much the SIDO muffler. The poor performance of the SIDO muffler was attributed to the end-outlet location. By moving the end outlet to the side as shown in Fig. 2.9(b), it is possible to nullify the limitations of the previous muffler configuration. The muffler with end center inlet and two side outlets located at a distance $L_2 = L_3 = L/2$ from the end face is shown in Fig. 2.9(b). From Fig. 2.13 it can be observed that in this new configuration, the muffler behaves similar to the end inlet/side outlet muffler and shows broadband attenuation characteristics. However, similar to the previous SIDO configuration in Fig. 2.9(a) , the (0, 2) modes are not attenuated for this muffler. Therefore, mufflers in Fig. 2.9(a) and Fig. 2.9(b) show similar dips in TL characteristics above the cutoff frequency of the (0, 2) mode.

The TL curve for the SIDO muffler with side-inlet and end-outlets (Fig. 2.9(c)) is shown in Fig. 2.14. In this orientation, the (2, 1) mode is not suppressed. The propagation of the (2, 1) mode causes the TL curve to dip at about 2800 Hz. Since the radial modes propagate at frequencies higher than the frequency corresponding to (2, 1) mode, the radial locations of the end outlets bear no significant influence on the TL for acoustically long chambers of this type. From the figure it is evident that the location of the inlet strongly affects the TL. The TL curve is characterized by a broad one dimensional dome having width, $f = c/L\ Hz$. The frequencies corresponding to the resonating peaks of these domes depend on the location of the side inlet. It

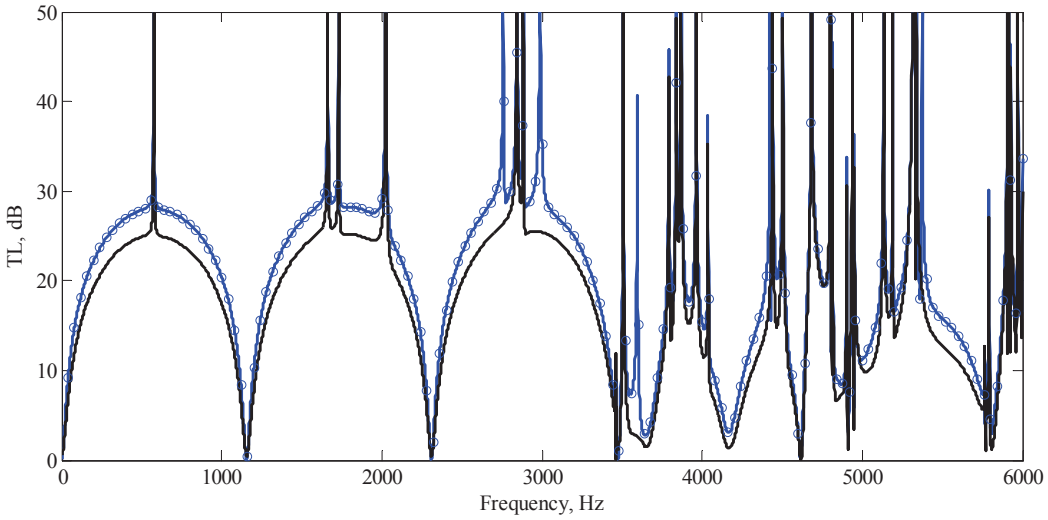

Figure 2.13: TL comparison of mufflers having inlet/outlets as shown in Fig. 2.9(b). $L_2 = L_3 = L/2$; ——— SIDO muffler, $d_1 = d_2 = d_3 = D/5$; –o–o–o– End-inlet/side-outlet muffler, $d_1 = d_3 = D/5,\ d_2 = 0$

can be shown that if the side inlet is located at a distance of $L/2m,\ m = 1, 2, 3, \cdots$, the peaks will be located at frequencies, $f_p = m(2n-1)c/2L, n = 1, 2, 3, \cdots$, provided that f_p is below the cut-off frequency of the first higher–order propagating mode. It must be mentioned that the peaks are not due to resonant condition; the denominator in Eq. (2.29) is zero at these frequencies, resulting in an infinite input impedance.

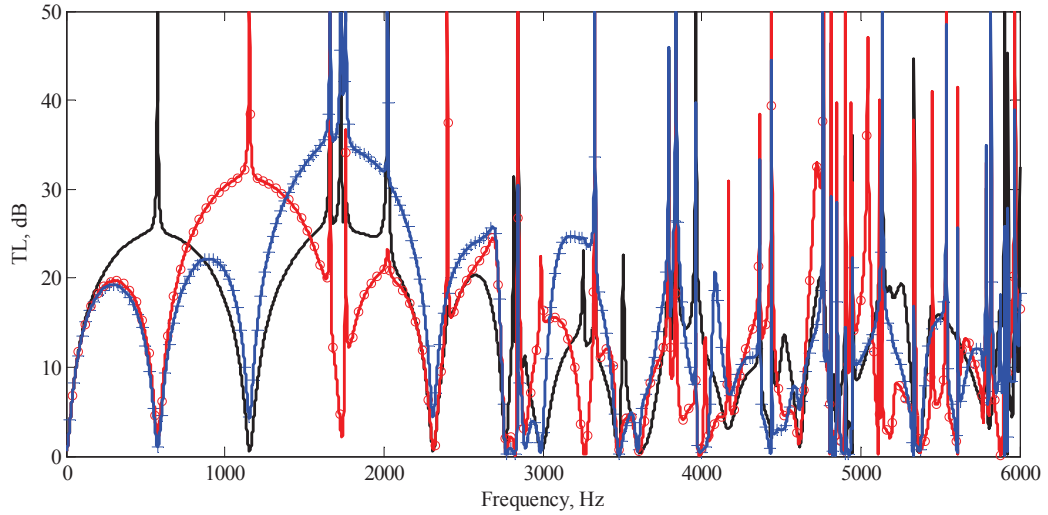

Figure 2.14: TL comparison of mufflers having inlet/outlets as shown in Fig. 2.9(c). $d_1 = d_2 = d_3 = D/5$; ——— $L_1 = L/2$; –o–o–o– $L_1 = L/4$; –+–+–+– $L_1 = L/6$

A broadband attenuation pattern similar to the side-inlet/side-outlet configuration of prior

work [16] is obtained when the inlet and the outlets are positioned according to Fig. 2.9(d). Figure 2.15 shows the TL characteristics for various axial locations of the outlet ports. The inlet is located at $L_1 = L/2$ which corresponds to a pressure minima for $p = (2n+1), n = 0, 1, 2, \cdots$, longitudinal modes. When the outlets are located at distances $L_2 = L_3 = L/4$, pressure minima occur at $p = 2(2n+1), n = 0, 1, 2, \cdots$, at the outlet ports. Therefore, there are pressure minima either at the inlet or at the outlets for $p = 1, 2, 3, \cdots$ This behavior results in a broadband attenuation pattern (solid line in Fig. 2.15) for this inlet/outlet configuration from $f = 0 - 2200$ Hz. By changing the location of the outlets, the broadband attenuation pattern can be shifted along the frequency axis, as shown in Fig. 2.15. Thus, similar to the previous configuration, the side inlet/outlet muffler can be utilized to attenuate sound over a desired frequency range by proper choice of the outlets. However, the effectiveness of such mufflers is limited to the cut-off frequency of the (2, 1) mode beyond which there is a dip in the TL due the propagation of this mode.

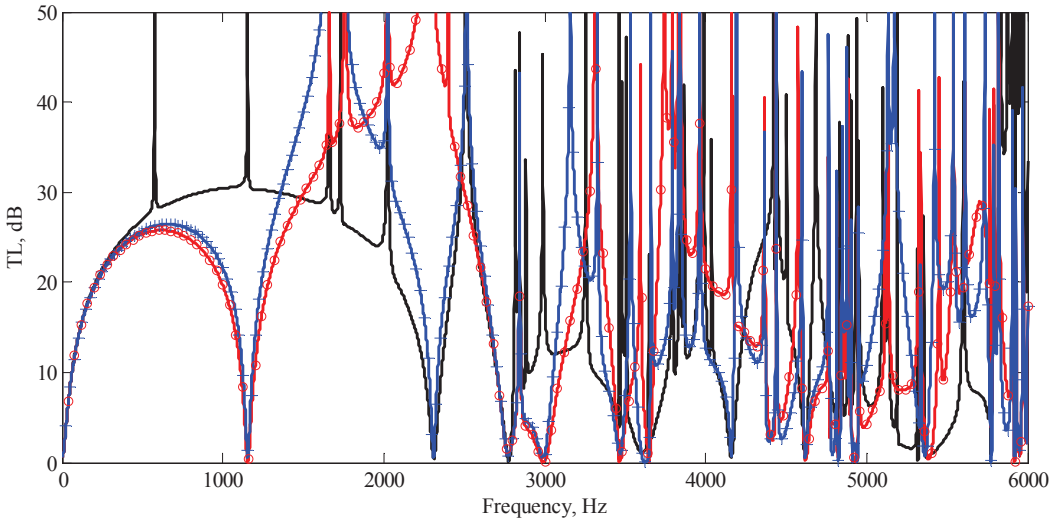

Figure 2.15: TL comparison of mufflers having inlet/outlets as shown in Fig. 2.9(d). $d_1 = d_2 = d_3 = D/5$; ——— $L_1 = L/2,\ L_2 = L_3 = L/4$; -+-+-+- $L_1 = L/2,\ L_2 = L/6,\ = L_3 = 5L/6$; –o–o–o– $L_1 = L/2,\ L_2 = L/8,\ = L_3 = 7L/8$

2.3.2 Parametric study: DISO muffler

Parametric studies on DISO mufflers are performed by considering the same muffler geometries as shown in Fig. 2.9. However, for DISO muffler, subscripts 2 and 3 in Fig. 2.9 indicate inlet ports, and subscript 1 indicates outlet port. For single-inlet/single-outlet mufflers, the principle

of reciprocity holds. As a consequence, by interchanging inlet and outlet, the TL curve remains unchanged. Similar analogy applies for the SIDO/ DISO mufflers under certain conditions. By reversing inlet and outlets, the SIDO muffler acts like a DISO muffler, however the TL curves for these two systems may not be the same (assuming that the other conditions such as geometry, port size etc. are the same). Usually, if inlets and outlet are located symmetrically to each other and if the incoming pressure waves are in phase, i.e., $P_2^+ = P_3^+$, then the DISO muffler will have same TL characteristics as the SIDO muffler. For e.g., in Fig. 2.9(b), if $L_2 = L_3$, then the ports 2 and 3 are symmetrically located w.r.t the port 1. Consequently, the SIDO and the DISO muffler in this configuration will have same TL curve if the incoming waves are in phase. If incoming waves are not in phase, interference between the sources at the outlet will alter TL. In Fig. 2.16, TL for a DISO muffler with same inlets and outlet orientations as in Fig. 2.9(d) is presented. For comparison, TL curve of a SIDO muffler with same port locations is also presented. As previously described, the DISO and the SIDO curves overlap each other when the incoming waves are in phase. When the incoming waves are $\pi/2$ out of phase, the TL increases due to interference between the sources. Since the outlet is symmetrically located from the inlet, when the sources are out π of phase, the outlet location corresponds to a pressure release surface. Hence, complete attenuation is possible for such conditions.

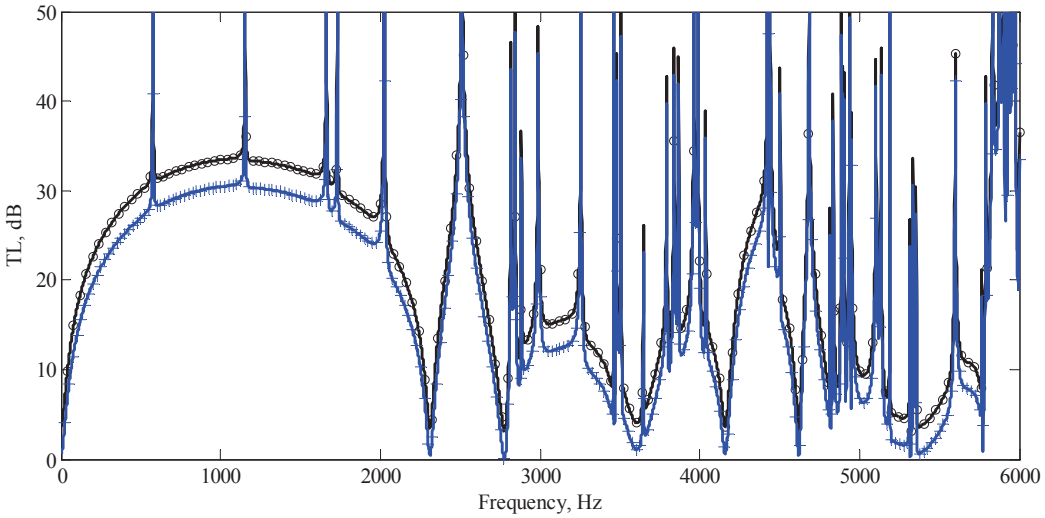

Figure 2.16: TL comparison of mufflers having inlet/outlets as shown in Fig. 2.9(d). $d_1 = d_2 = d_3 = D/5$; ——— DISO, $L_1 = L/2,\ L_2 = L_3 = L/4,\ P_2^+/P_3^+ = 1$; -+-+-+- SIDO, $L_1 = L/2,\ L_2 = L_3 = L/4$; –o–o–o– DISO, $L_1 = L/2,\ L_2 = L_3 = L/4,\ P_2^+/P_3^+ = 1i$

In Fig. 2.17, the TL curve for a DISO muffler with same port orientations as in Fig. 2.9(a) has

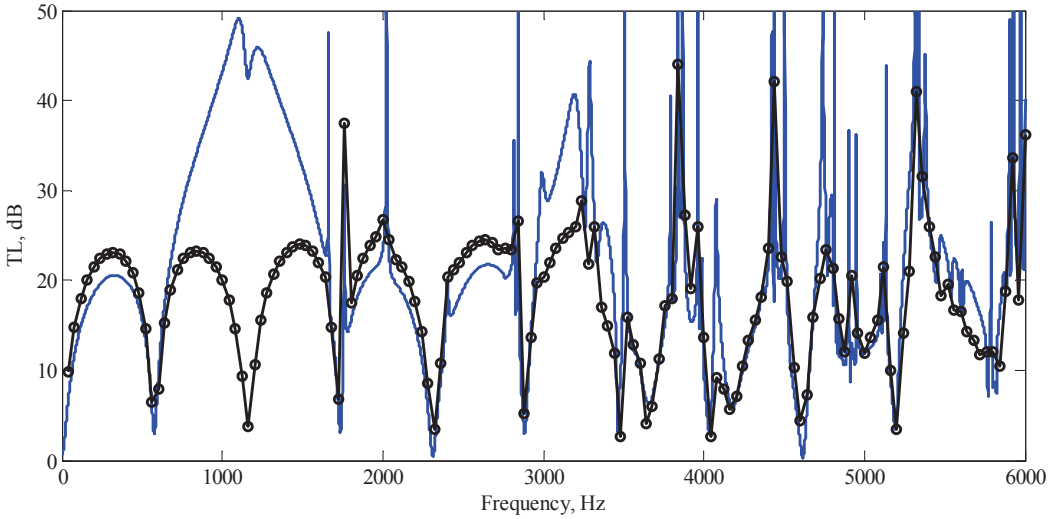

Figure 2.17: TL comparison of mufflers having inlet/outlets as shown in Fig. 2.9(a). $d_1 = d_2 = d_3 = D/5,\ \delta = 0.6276R;$ —— $L_2 = L,\ L_3 = L/2,\ P_2^+/P_3^+ = 1;$ –o–o–o– $L_2 = L,\ L_3 = L/2,\ P_2^+/P_3^+ = 1i$

been depicted. The asymmetric locations of inlet ports results in a different sound attenuation characteristics in DISO muffler from SIDO muffler. As can be observed from the figure, at certain frequencies in-phase incoming waves result in a larger TL compared to out-of-phase waves. At other frequencies, opposite effect occurs. Therefore, sound attenuation characteristics are affected by the phase difference as well as the frequency.

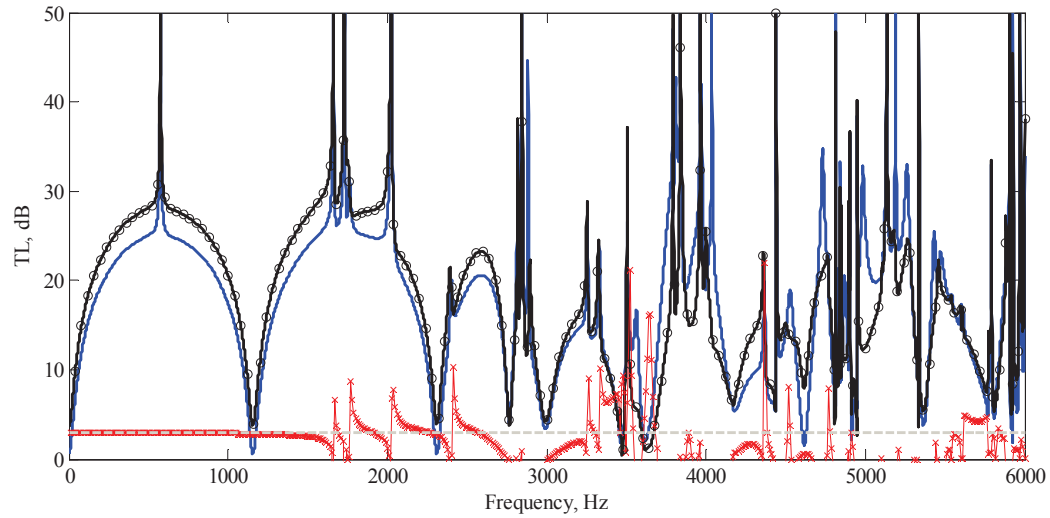

Figure 2.18: TL comparison of mufflers having inlet/outlets as shown in Fig. 2.9(c). $d_1 = d_2 = d_3 = D/5,\ \delta = 0.6276R;$ —— $P_2^+/P_3^+ = 1;$ –o–o–o– $P_2^+/P_3^+ = 1i;$ - - - - - $\triangle TL = 10\log_{10} 2;$ –x–x–x– $\triangle TL$

The TL for the DISO muffler having same port orientations as in Fig. 2.9(c) is shown in Fig. 2.18. As noted previously, phase difference between the incoming waves affects the TL characteristics. At low frequencies, only plane waves propagate. As a result, the radial location of inlet 2 doesn't influence the TL at these frequencies. Therefore, the outlet 'observes' the inlets to be located at the same distance from it (i.e., the axial distance). Selamet and Ji [69] have derived the equation of TL for a DISO muffler using the plane wave approximation (see Eq. 10 in the reference). Using the same equation, the difference in the TL when $P_2^+/P_3^+ = 1$ and when $P_2^+/P_3^+ = 1i$ is (when the inlets have same area):$\triangle TL = TL_{P_2^+/P_3^+=1i} - TL_{P_2^+/P_3^+=1} = 10\log_{10}2$. In Fig. 2.18, this difference is validated in the plane wave limit. At higher frequencies, the propagating waves are no longer planar. Therefore, the inlets are effectively no longer equidistant from the outlet, which causes a departure from the theoretically predicted difference in the TL.

2.4 Validation: elliptic geometries

In an elliptic domain, the general solution of Eq. (2.1) is of the form:

$$\varphi_j = A_{mn}Se_m(q_{mn},\eta)Je_m(q_{mn},\zeta)\cos(p\pi z/L) + B_{mn}So_m(\bar{q}_{mn},\eta)Jo_m(\bar{q}_{mn},\zeta)\cos(p\pi z/L) \quad (2.31)$$

where Se_m and So_m are even and odd Mathieu functions of the first kind. Je_m and Jo_m are the Modified Mathieu function of the first kind [71]. The parameters ζ and η are the radial and circumferential basis–parameters for an elliptic coordinate system. The parameter q is related to the wave number and is given by:

$$\frac{4q^2}{h^2} = k^2 - \left(\frac{p\pi}{L}\right)^2 \quad (2.32)$$

Again, using the rigid boundary condition at the shell surface, the characteristic equations for q and $\bar{q}$ for each m are obtained from the following equations:

$$Je'_m(q,\zeta_1) = 0; \qquad Jo'_m(\bar{q},\zeta_1) = 0 \quad (2.33)$$

It may be noted from Eq. (2.33) that due to the loss of circumferential symmetry, mode–splitting occurs for the elliptical problem [30]. The splitting of the eigenvalues yields eigenvector–pairs that are not symmetric when rotated by $\pi/2$ angle. Therefore, it is possible that one of the eigenmodes may be non-evanescent for a particular port orientations. It will be observed in the

next sections that the propagation of such higher–order modes in an elliptical muffler results in lower TL.

The GFM was implemented for elliptical mufflers in order to determine the TL. The numerical implementation was first verified with the works of Denia *et al.*[72]. The Mode Matching Method was employed in their work for determining the TL in an elliptic SIDO muffler. The inlet and the outlets were located at the end–face of the chamber. The verification of the present implementation with some of the results reported in [72] is presented in Fig. 2.19.

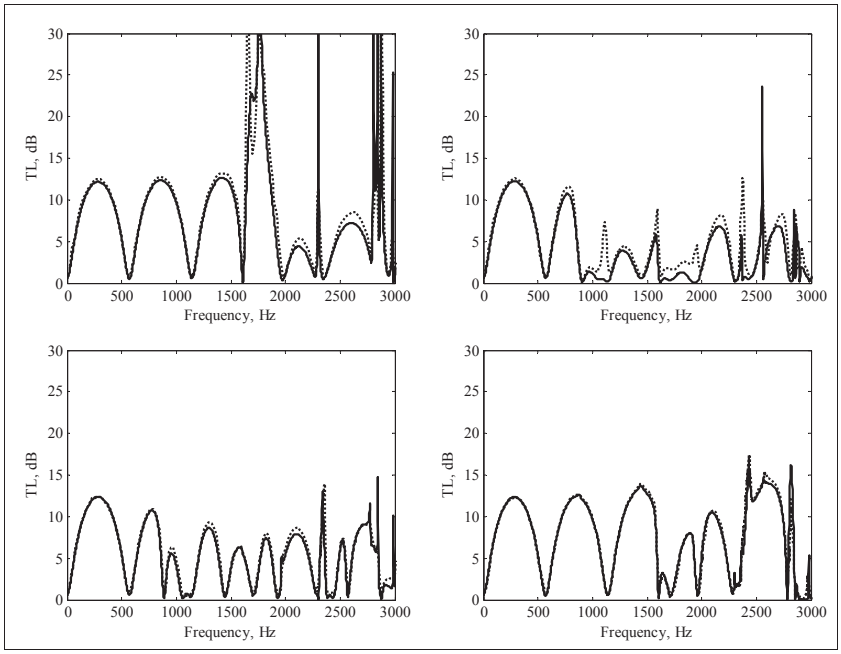

Figure 2.19: Numerical verification of the GFM applied to an elliptic SIDO muffler configuration. —— GFM; ····· MMM in Ref. [72]. $L = 0.3\ m$, semi-major axis $a = 0.115\ m$, semi-minor axis $b = 0.065\ m$, $\varphi_1 = \varphi_2 = 0,\ \varphi_3 = \pi$ (a) $\delta_1 = 0, \delta_2 = \delta_3 = 0.073\ m$ (b) $\delta_1 = \delta_2 = \delta_3 = 0.073\ m$ (c) $\delta_1 = 0.05\ m,\ \delta_2 = 0.06\ m,\ \delta_3 = 0.03\ m$ (d) $\delta_1 = 0,\ \delta_2 = \delta_3 = 0.048\ m$

2.4.1 Parametric study: SIDO

An elliptic chamber muffler with the same inlet and outlet orientations as that in Fig. 2.9 was considered for the present parametric study. The eccentricity of the muffler was $e = 0.8$, and the area of cross–section was same as that of the circular chamber studied in the previous section. From the study of the cylindrical chamber configurations, only the port orientations in Fig. 2.9(b) and (c) yielded improved TL. Hence, only these orientations are considered in the study of the elliptic geometry. In Fig. 2.20 and Fig. 2.21, the TL for the elliptic SIDO geometries are presented.

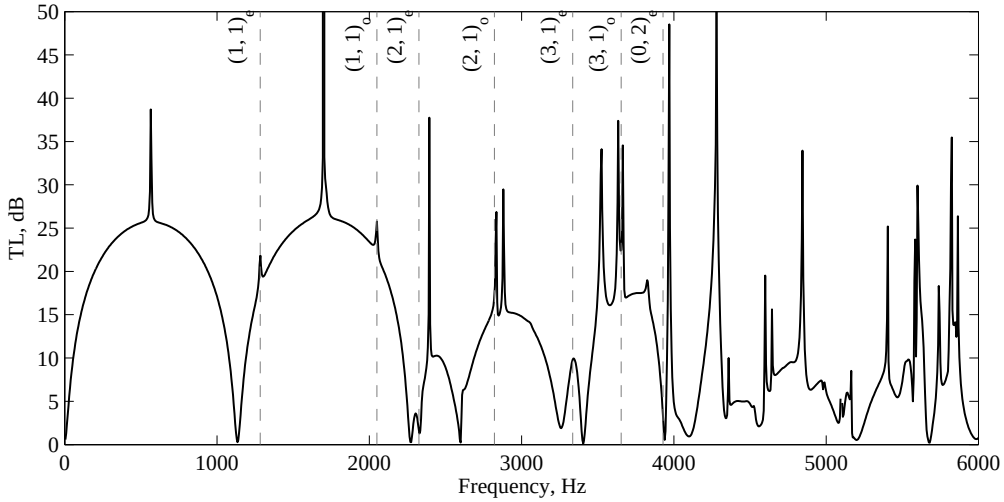

Figure 2.20: TL of an elliptic muffler having inlet/outlets and same area and length as shown in Fig. 2.9(b). $L_2 = L_3 = L/2$; ——— SIDO muffler, $d_1 = d_2 = d_3 = D/5$

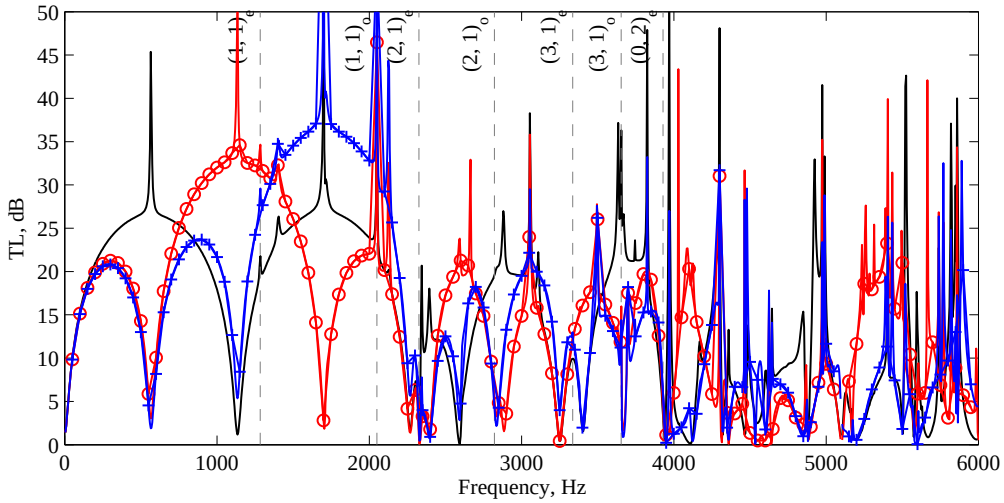

Figure 2.21: TL of an elliptic muffler having inlet/outlets and same area and length as shown in Fig. 2.9(c). $d_1 = d_2 = d_3 = D/5$; ——— $L_1 = L/2$; –o–o–o– $L_1 = L/4$; –+–+–+– $L_1 = L/6$

Similar to the cylindrical chamber, the TL curve is characterized by the presence of broadband domes that depend on the location of the side inlet/outlet. In the plane–wave limit, the TL for the elliptic chamber is expectedly the same as that of the circular chamber muffler. However, unlike the cylindrical geometry, the (2, 1) even mode in the elliptic chamber is non-evanescent above it's cutoff frequency. The propagation of this mode results in a sharp dip in the TL curve, thereby limiting the useful frequency range of the elliptic chamber muffler.

2.4.2 Parametric study: DISO

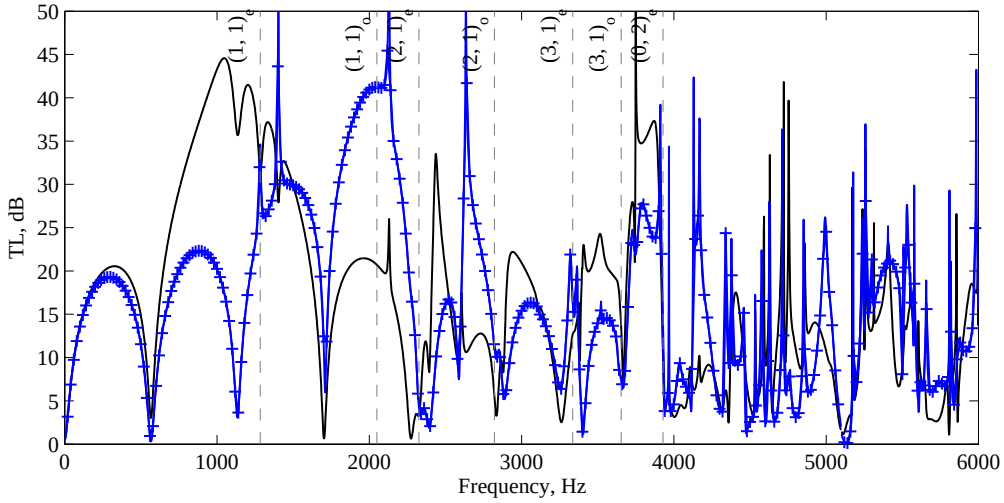

Figure 2.22: TL of an elliptic muffler having inlet/outlets and same area and length as shown in Fig. 2.9(a); $P_2^+/P_3^+ = 1$, $d_1 = d_2 = d_3 = D/5$; ——— $L_3 = L/2$; +++++ $L_3 = 3L/4$

The parametric studies on the DISO elliptic mufflers were performed by keeping the same geometric dimensions as the SIDO configuration. In Fig. 2.22, the TL curve for a DISO muffler with the same port orientation as in Fig. 2.9(a) is presented. As discussed in the previous section, in the DISO muffler, the relative phase between the piston sources affects the TL. For the present configuration in Fig. 2.22, the inlet pistons were in phase with each other. Since the ports were at different locations in the muffler, the incident wave from one of the sources experienced interference due to the other, and $vice - verse$. The mismatch of phase between these two waves resulted in an increased TL. As an example, if Fig. 2.22, a peak in the TL is observed at around 1000 Hz, which corresponds to a frequency when $k(L - L_3) = (2n + 1)\pi,\ n = 0, 1, \cdots$. In other words, the two incident plane waves are in opposite phase at the location of the side–inlet port, thereby resulting in increased sound attenuation. Similarly, when the side–inlet port is shifted to a different location, there is a corresponding shift in the peak TL. Similar to the SIDO mufflers, the useful range of performance in the DISO muffler is restricted to the cutoff frequency of the (2, 1) even mode and hence no peaks are observed beyond 2000 Hz in the present configurations.

The performance of the SIDO and the DISO elliptic muffler for other geometric configurations that are not presented here follow the same TL characteristics as the circular chamber muffler discussed earlier, except for the non–evanescent (2, 1) mode. The mode shapes and the suppression of these higher–order modes are discussed in chapter 3.

2.5 Summary

In this chapter, a general procedure based on three dimensional Green's function was developed in order to study the sound attenuation in SIDO and DISO circular and elliptic chamber mufflers. The Green's function method (GFM) was observed to be a simplification to the Mode Matching Method (MMM). While the GFM was suitable for most muffler geometries where the method of separation of variables are applicable, the MMM could also be employed for studying extended chamber mufflers.

The formulation for the SIDO and DISO configuration was validated through existing TL results in the literature. The method was found to be flexible as both the SIDO and the DISO configurations could be studied by making small changes to the mathematical formulations. Parametric studies were performed to understand the effect of various inlet and outlet configurations on the TL. Deriving knowledge from single inlet/outlet mufflers, broadband attenuation characteristics were observed by proper orientation of inlets/outlets in the SIDO and DISO mufflers. Minor loss in TL was observed for the SIDO muffler when compared to an equivalent single outlet muffler. For the DISO muffler, depending upon the phase difference between the incoming waves, and the orientation of the ports, yielded in a TL curve that exactly matched the TL curve for the corresponding SIDO muffler. This similarity was a consequence of the principle of reciprocity. It was also observed that a pressure release surface could be achieved for certain DISO muffler configurations. Thus, complete attenuation of sound was possible in a DISO muffler. In the elliptic chamber muffler, unlike the cylindrical chamber the (2, 1) even mode was observed to be a non-evanescent mode for most muffler geometries. The propagation of this mode beyond the cutoff frequency resulted in poor TL at higher frequencies. In this respect, the elliptic chamber mufflers may be considered as inferior to cylindrical chamber mufflers.

Chapter 3

Transmission loss in distorted cylindrical mufflers

It can be inferred from the study of elliptic mufflers in chapter 2, that the loss of circular symmetry results in the propagation of certain higher–order modes that are essentially suppressed for the cylindrical configuration. The shape of these eigenmodes depends on the nature of the boundary asymmetry. Motivated by the need to quantify the effects of these asymmetries on the sound attenuation, a general procedure for determining the TL in a distorted circular muffler using a perturbation approach similar to that of Nayfeh *et al.*, [36, 73] is illustrated in this chapter. First, the eigensolutions for a distorted circular annular region is derived based on the method of strained parameters. Since the Helmholtz equation is self-adjoint, the eigenvectors are orthogonal up to the order of truncation of the perturbation parameters. By taking suitable geometric limits, the eigensolutions for the distorted annular region may be extended to the entire muffler domain. Using the perturbed eigensolutions, the TL in the muffler is derived by either implementing a mode matching method or the Green's function method. In order to illustrate the method, elliptical mufflers with moderate eccentricities $(0.4 \sim 0.6)$ are considered. Exact solutions for the natural frequencies and TL in an elliptical muffler have previously been reported in the literature [31, 33, 34]. The perturbation results are compared to the exact/FEM solutions. The solution procedure is general, and may be employed for any symmetric/asymmetric boundary perturbations (within small perturbation limits).

3.1 Mathematical formulation

3.1.1 Determination of the eigensolutions

In this section, the solutions to the Helmholtz equation is derived for an annular geometry as shown in Fig. 3.1. Considering harmonic time-dependence, the wave equation may be expressed

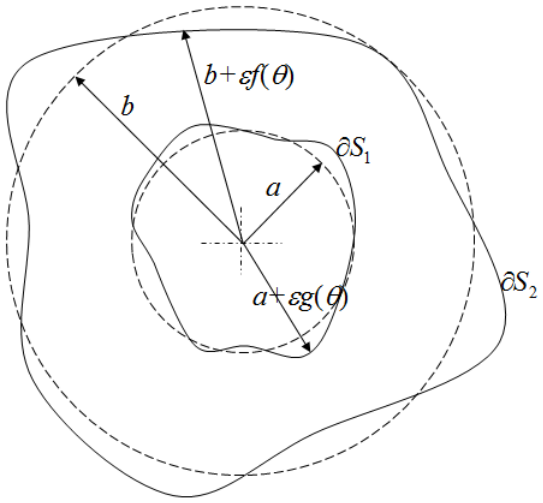

Figure 3.1: Schematic of an annular perturbed cylinder.

in term of the velocity potential as:

$$\bigtriangledown^2 \phi(r,\theta) + k^2\phi(r,\theta) = 0; \quad a + \varepsilon f(\theta) \leq r \leq b + \varepsilon g(\theta) \tag{3.1}$$

where, $k = \omega/c$ is the wave number, ω is the angular frequency, and c is the speed of sound. Assuming that walls of the waveguide are rigid, the normal component of the velocity is zero, implying that:

$$\bigtriangledown \phi(r,\theta) \cdot \vec{\eta}|_S = 0; \tag{3.2}$$

where, η corresponds to the normal vector to the surface of the waveguide. In the present formulation, the radii of curvature of the annular geometry are small perturbations from a circle. The inner radius of curvature is approximated by $r = a + \varepsilon f(\theta)$, where a is the mean radius of curvature, ε is the perturbation parameter, and $f(\theta)$ is the circumferential departure from circular geometry. Similarly, the outer radius of curvature is given by $r = b + \varepsilon g(\theta)$. In the perturbed domain, the normal vectors can be expressed as an expansion involving ε and the circumferential departure parameters. For example, at the inner annular boundary:

$$\vec{\eta} = \left(1 - \frac{1}{2}\left[\frac{\varepsilon}{a}\frac{df}{d\theta}\right]^2 + O(\varepsilon^3)\right)\vec{e_r} - \left(\frac{\varepsilon}{a}\frac{df}{d\theta} - f\frac{df}{d\theta}\left[\frac{\varepsilon}{a}\right]^2 + O(\varepsilon^3)\right)\vec{e_\theta} \qquad : \partial S_1 \tag{3.3}$$

By substituting Eq. (3.3) into Eq. (3.2), the boundary conditions can be expressed as:

$$\left(1-\frac{1}{2}\left[\frac{\varepsilon}{a}\frac{df}{d\theta}\right]^2+O(\varepsilon^3)\right)\frac{\partial\phi}{\partial r}-\frac{1}{a}\left(\frac{\varepsilon}{a}\frac{df}{d\theta}-f\frac{df}{d\theta}\left[\frac{\varepsilon}{a}\right]^2+O(\varepsilon^3)\right)\frac{\partial\phi}{\partial\theta}=0 \qquad :\partial S_1 \tag{3.4}$$

As $\varepsilon \to 0$, the Helmholtz equation and the boundary conditions are that of a circular cylindrical annular shell. Therefore, it is expected that for small values of ε, eigensolutions for distorted waveguides should be perturbations to those of a cylindrical shell. Accordingly, eigensolutions of the distorted geometry is expressed as an expansion in ε and the unperturbed eigensolutions:

$$\begin{aligned}\phi(\vec{r},\varepsilon) &= \phi_0(\vec{r},\varepsilon)+\varepsilon\phi_1(\vec{r},\varepsilon)+\cdots\\ k_r(\varepsilon) &= k_{0r}(\varepsilon)+\varepsilon k_{1r}(\varepsilon)+\varepsilon^2 k_{2r}(\varepsilon)+\cdots\end{aligned} \tag{3.5}$$

The subscript r in Eq. (3.5) signifies radial component. For convenience, the subscript will henceforth be omitted. Substituting Eq. (3.5) into Eq. (3.1) and Eq. (3.4), and separating terms containing each order of ε yields the following sets of equations:

$$\begin{aligned}O(\varepsilon^0): \quad &\bigtriangledown^2\phi_0+k_0^2\phi_0=0;\\ &\left.\frac{\partial\phi_0}{\partial r}\right|_{r=a,b}=0\end{aligned} \tag{3.6}$$

$$\begin{aligned}O(\varepsilon^1): \quad &\bigtriangledown^2\phi_1+2k_0k_1\phi_0+k_0^2\phi_1=0;\\ &\left.\frac{\partial\phi_1}{\partial r}+f\frac{\partial^2\phi_0}{\partial r^2}-\frac{1}{a^2}\frac{df}{d\theta}\frac{\partial\phi_0}{\partial\theta}\right|_{r=a}=0; \quad \left.\frac{\partial\phi_1}{\partial r}+g\frac{\partial^2\phi_0}{\partial r^2}-\frac{1}{b^2}\frac{dg}{d\theta}\frac{\partial\phi_0}{\partial\theta}\right|_{r=b}=0;\end{aligned} \tag{3.7}$$

$$\begin{aligned}O(\varepsilon^2): \quad &\bigtriangledown^2\phi_2+\left(k_1^2+2k_0k_2\right)\phi_0+2k_0k_1\phi_1+k_0^2\phi_2=0;\\ &\left.\frac{\partial\phi_2}{\partial r}+f\frac{\partial^2\phi_1}{\partial r^2}-\frac{1}{a^2}\frac{df}{d\theta}\frac{\partial\phi_1}{\partial\theta}+\frac{f^2}{2}\frac{\partial^3\phi_0}{\partial r^3}+\frac{1}{a^3}\frac{d}{d\theta}\left(\frac{f^2}{2}\right)\frac{\partial\phi_0}{\partial\theta}\right|_{r=a}=0;\\ &\left.\frac{\partial\phi_2}{\partial r}+g\frac{\partial^2\phi_1}{\partial r^2}-\frac{1}{b^2}\frac{dg}{d\theta}\frac{\partial\phi_1}{\partial\theta}+\frac{g^2}{2}\frac{\partial^3\phi_0}{\partial r^3}+\frac{1}{b^3}\frac{d}{d\theta}\left(\frac{g^2}{2}\right)\frac{\partial\phi_0}{\partial\theta}\right|_{r=b}=0;\end{aligned} \tag{3.8}$$

In the above equations, the boundary conditions are obtained by assuming that the annular walls are rigid. A detailed derivation of the above equations may be found in [74]. Equation (3.6) is the Helmholtz equation for a rigid circular annulus of inner radius a, and outer radius b. The solution to Eq. (3.6) may be derived in terms of the Bessel functions and the trigonometric

functions as:

$$\begin{aligned} &\phi_0 = A_{nm}\varphi^0_{nm}(r)\cos\left(n\theta - \psi_n\right) \\ &\text{where, } \varphi^0_{nm}(r) = \left(J_n\left(k_{0,nm}r\right) - \frac{J_n'((k_{0,nm}b)}{Y_n'\left(k_{0,nm}b\right)}Y_n\left(k_{0,nm}r\right)\right) \end{aligned} \tag{3.9}$$

In Eq. (3.9), $k_{0,nm}$ are the characteristic roots of the equation obtained by imposing the rigid boundary condition:

$$J_n'\left(k_{0,nm}a\right) - \frac{J_n'((k_{0,nm}b)}{Y_n'\left(k_{0,nm}b\right)}Y_n'\left(k_{0,nm}a\right) = 0 \tag{3.10}$$

The indices n, m represent circumferential and radial modes. A_{nm} is an arbitrary constant. For a circular geometry, the circumferential modes have no angular preference and ψ_n is an arbitrary phase angle. For radially asymmetric geometries, ψ_n have distinct values if boundary perturbations cause degenerate eigenvalues to split into two distinct eigenvalues [39]. The first-order approximation for each ϕ_0 is assumed to be of the form:

$$\phi_1 = \sum_{s=0}^{\infty} B_s\beta_s(r)\cos(s\theta - \lambda_s) \tag{3.11}$$

The radial term $\beta_s(r)$, and parameter λ_s, are obtained by substituting Eq. (3.9) and Eq. (3.11) into Eq. (3.7):

$$\sum_{s=0}^{\infty} B_s\left(\frac{d^2}{dr^2} + \frac{1}{r}\frac{d}{dr} + k_{0,nm}^2 - \frac{s^2}{r^2}\right)\beta_s(r)\cos(s\theta - \lambda_s) + \left(2k_0k_1A\varphi^0(r)\right)_{nm}\cos(n\theta - \psi_n) = 0; \quad a \le r \le b \tag{3.12}$$

Using orthogonality of *sine* and *cosine* functions, Eq. (3.12) is decoupled into an infinite number of equations in $\beta(r)$:

$$\begin{aligned} &B_q\left(\frac{d^2}{dr^2} + \frac{1}{r}\frac{d}{dr} + k_{0,nm}^2 - \frac{q^2}{r^2}\right)\beta_q(r)\cos(\lambda_q) + \left(2k_0k_1A\varphi^0(r)\right)_{nm}\cos(\psi_n)\delta(n,q) = 0; \\ &B_q\left(\frac{d^2}{dr^2} + \frac{1}{r}\frac{d}{dr} + k_{0,nm}^2 - \frac{q^2}{r^2}\right)\beta_q(r)\sin(\lambda_q) + \left(2k_0k_1A\varphi^0(r)\right)_{nm}\sin(\psi_n)\delta(n,q) = 0; \\ &\text{where, } a \le r \le b; \qquad \delta(n,q) = \begin{cases} 0 & : q \ne n \\ 1 & : q = n \end{cases}; \qquad q = 0, 1, 2, ... \end{aligned} \tag{3.13}$$

When $q \neq n$, Eq. (3.13) is the homogeneous Bessel equation of order q; the general solution is given by:

$$\beta_q(r) = C_qJ_q(k_{0,nm}r) + D_qY_q(k_{0,nm}r); \qquad a \le r \le b \tag{3.14}$$

where, the constants C_q and D_q are derived from the boundary conditions. By substituting Eq. (3.9) and Eq. (3.14) into the boundary conditions given in Eq. (3.7), and by using the orthogonality of the *cosine* and *sine* functions yields the following sets of infinite number of decoupled equations necessary for determining the four unknown parameters B_q, C_q, D_q and λ_q:

$$
\begin{aligned}
&B_q\beta_q'(r)\cos(\lambda_q) = \\
&\frac{A_{nm}}{2e_q}\left[n\left\{(n+q)[*]_{n+q}+(n-q)[*]_{|n-q|}\right\}\frac{\varphi^0_{nm}(r)}{r^2}-\left\{[*]_{n+q}+[*]_{|n-q|}\right\}\varphi^{0\prime\prime}_{nm}(r)\right]\cos(\psi_n)\\
&+\frac{A_{nm}}{2e_q}\left[n\left\{(n+q)[\bar{*}]_{n+q}+|n-q|[\bar{*}]_{|n-q|}\right\}\frac{\varphi^0_{nm}(r)}{r^2}-\left\{[\bar{*}]_{n+q}+\frac{n-q}{|n-q|}[\bar{*}]_{|n-q|}\right\}\varphi^{0\prime\prime}_{nm}(r)\right]\sin(\psi_n)
\end{aligned}
$$

$$
\begin{aligned}
&B_q\beta_q'(r)\sin(\lambda_q) = \\
&-\frac{A_{nm}}{2}\left[n\left\{(n+q)[*]_{n+q}-(n-q)[*]_{|n-q|}\right\}\frac{\varphi^0_{nm}(r)}{r^2}-\left\{[*]_{n+q}-[*]_{|n-q|}\right\}\varphi^{0\prime\prime}_{nm}(r)\right]\sin(\psi_n)\\
&+\frac{A_{nm}}{2}\left[n\left\{(n+q)[\bar{*}]_{n+q}-|n-q|[\bar{*}]_{|n-q|}\right\}\frac{\varphi^0_{nm}(r)}{r^2}-\left\{[\bar{*}]_{n+q}-\frac{n-q}{|n-q|}[\bar{*}]_{|n-q|}\right\}\varphi^{0\prime\prime}_{nm}(r)\right]\cos(\psi_n)\\
&\text{where, } r=a \text{ or } b;\ \ [*]\left([\bar{*}]\right)=\begin{cases}F(\bar{F}) & :r=a\\ G(\bar{G}) & :r=b\end{cases};\ \ e_q=\begin{cases}2 & :q=0\\ 1 & :q\neq 0\end{cases}
\end{aligned}
\tag{3.15}
$$

The coefficients F, $\bar{F}$, G and $\bar{G}$, are the Fourier coefficients of the perturbation functions $f(\theta)$ and $g(\theta)$:

$$
f(\theta)=\sum_{j=1}^{\infty}\left(F_j\cos(j\theta)+\bar{F}_j\sin(j\theta)\right);\qquad g(\theta)=\sum_{j=1}^{\infty}\left(G_j\cos(j\theta)+\bar{G}_j\sin(j\theta)\right) \tag{3.16}
$$

In Eq. (3.15), the general form of $\beta_q(r)$ given by Eq. (3.14) is valid only when $q\neq n$. When $q=n$, Eq. (3.13) is a non-homogeneous second order differential equation; a non-trivial solution to this equation exists only when the solvability conditions [36] are satisfied. By using this solvability condition, the first order approximation to the radial wave number may be derived as:

$$
\begin{aligned}
k_{1,nm}&=-\frac{B_q\left(r\varphi^0_{nm}(r)\ \beta_q'(r)\Big|_{r=a}^{r=b}\right)\cos(\lambda_q)}{2A_{nm}k_{0,nm}\int_a^b\xi\left\{\varphi^0_{nm}(\xi)\right\}^2d\xi\cos(\psi_n)};\qquad q=n\\
k_{1,nm}&=-\frac{B_q\left(r\varphi^0_{nm}(r)\ \beta_q'(r)\Big|_{r=a}^{r=b}\right)\sin(\lambda_q)}{2A_{nm}k_{0,nm}\int_a^b\xi\left\{\varphi^0_{nm}(\xi)\right\}^2d\xi\sin(\psi_n)};\qquad q=n
\end{aligned}
\tag{3.17}
$$

The terms in Eq. (3.17) involving B_q, β_q, and λ_q, are obtained from Eq. (3.15) by setting $q = n$. The substitution of Eq. (3.15) into Eq. (3.17), and by re-arranging terms containing $k_{1,nm}$, $\cos(\psi_n)$ and $\sin(\psi_n)$ yields the following eigenvalue problem:

$$
\begin{aligned}
&k_{1,nm} \left\{ \begin{array}{c} \cos(\psi_n) \\ \sin(\psi_n) \end{array} \right\} = \\
&\Theta_{nm}(a) \left[\begin{array}{cc} F_{2n} & \bar{F}_{2n} \\ \bar{F}_{2n} & -F_{2n} \end{array} \right] \left\{ \begin{array}{c} \cos(\psi_n) \\ \sin(\psi_n) \end{array} \right\} - \Theta_{nm}(b) \left[\begin{array}{cc} G_{2n} & \bar{G}_{2n} \\ \bar{G}_{2n} & -G_{2n} \end{array} \right] \left\{ \begin{array}{c} \cos(\psi_n) \\ \sin(\psi_n) \end{array} \right\} \\
&\text{where, } \Theta_{nm}(r) = \left(\frac{n^2}{r^2} \varphi^0_{nm}(r) - \frac{\varphi^{0\prime\prime}_{nm}(r)}{2} \right) \left(\frac{r \varphi^0_{nm}(r)}{2k_{0,nm} \int_a^b \{\varphi^0_{nm}(\xi)\}^2 \xi d\xi} \right); \quad r = a, \text{or } b
\end{aligned}
\tag{3.18}
$$

Solving Eq. (3.18) yields the first order approximation to $k_{0,nm}$:

$$
k_{1,nm} = \pm \sqrt{\left(\Theta(a)F_{2n} - \Theta(b)G_{2n}\right)^2 + \left(\Theta(a)\bar{F}_{2n} - \Theta(b)\bar{G}_{2n}\right)^2} \tag{3.19}
$$

It may be observed from Eq. (3.16) and Eq. (3.19) that even for a distorted geometry, $k_{1,0m} = 0$. This observation is consistent with the fact that in the absence of a nodal diameter $(n = 0)$, the individual modes have no angular preference; and hence mode splitting does not occur. When $k_{1,0m} \neq 0$, Eq. (3.18) yields the eigenvector pairs $\{\cos(\psi_n), \sin(\psi_n)\}$. The determination of these eigenvector pairs completes the zeroth order solution (Eq. (3.9)). The first order solution is not yet complete as the non-homogeneous Eq. (3.13) remains to be solved for $q = n$. When $q = n$, solution to the first order problem may be obtained by assuming ϕ_1 to be comprised of a homogeneous solution (ϕ_1^h) and a particular integral (ϕ_1^p) [36, 75]:

$$
\begin{aligned}
&\phi_1 = \phi_1^h + \phi_1^p \\
&\text{where, } \phi_1^h = C_{nm} \varphi^0_{nm}(r) \cos(n\theta - \mu_n); \quad \phi_1^p = \sum_{j=1}^{\infty} D_{nm,j} \varphi^{1p}_{nj}(r) \cos(n\theta - \psi_n);
\end{aligned}
\tag{3.20}
$$

The radially dependent terms in the particular integral may be chosen as an orthogonal basis satisfying a boundary condition which is different from that of the homogeneous solution. In this formulation a pressure release boundary condition is chosen as a convenient form of the particular integral terms. Hence,

$$
\varphi^{1p}_{nj}(a) = \varphi^{1p}_{nj}(b) = 0 \tag{3.21}
$$

Therefore, the general form of the function $\varphi_{nj}^{1p}(r)$ satisfying the above boundary conditions may be expressed as:

$$\varphi_{nj}^{1p}(r) = J_n(\varpi_{nj} r) - \frac{J_n(\varpi_{nj} b)}{Y_n(\varpi_{nj} b)} Y_n(\varpi_{nj} r) \tag{3.22}$$

where, ϖ_{nj} are the roots of the characteristic equation:

$$J_n(\varpi_{nj} a) - \frac{J_n(\varpi_{nj} b)}{Y_n(\varpi_{nj} b)} Y_n(\varpi_{nj} a) = 0 \tag{3.23}$$

On substituting Eq. (3.20) into Eq. (3.13), and using the orthogonality of the trigonometric and the Bessel functions, the coefficients D in Eq. (3.20) may be derived as:

$$D_{nm,j} = -\frac{2k_{0,nm}k_{1,nm}\int_a^b \xi \varphi_{nm}^0(\xi)\varphi_{nj}^{1p}(\xi)d\xi}{\left(k_{0,nm}^2 - \varpi_{nj}^2\right)\int_a^b \xi\{\varphi_{nj}^{1p}(\xi)\}^2 d\xi} \tag{3.24}$$

The unique determination of C_{nm} and hence ϕ_1 cannot be obtained unless further restrictions on ϕ_1 is imposed. To this end, an additional condition that ϕ_1 is orthogonal to ϕ_0 is imposed [36, 39]. This condition results in an expression involving C_{nm} and μ_n:

$$C_{nm,j}\cos(\psi_n - \mu_n) = -\sum_{j=1}^{\infty} D_{nm,j}\frac{\int_a^b \xi \varphi_{nm}^0(\xi)\varphi_{nj}^{1p}(\xi)d\xi}{\int_a^b \xi\{\varphi_{nm}^0(\xi)\}^2 d\xi} \tag{3.25}$$

The determination of the unknown coefficients C_{nm} and μ_n requires solving the second order perturbation problem. The second order eigenfunctions are approximated as:

$$\phi_2 = \sum_{s=0}^{\infty} E_s \gamma_s(r)\cos(s\theta - \eta_s) \tag{3.26}$$

By using a solution procedure similar to that employed for determining the first order wave number corrections (i.e. Eq. (3.17)), the second order wave number corrections may be derived as:

$$\begin{aligned} k_2 = &-\frac{\left[rE_n\gamma_n'(r)\cos(\eta_n)\varphi_{nm}^0(r)\big|_a^b + A_{nm}k_{1,nm}^2\int_a^b \xi\left\{\varphi_{nm}^0(\xi)\right\}^2 d\xi\cos(\psi_n)\right]}{2A_{nm}k_{0,nm}\int_a^b \xi\left\{\varphi_{nm}^0(\xi)\right\}^2 d\xi\cos(\psi_n)} \\ &-\frac{\left[2k_{0,nm}k_{1,nm}^1\left(\cos(\psi_n)\sum_{j=1}^{\infty} D_{nm,j}\int_a^b \xi\varphi_{nm}^0(\xi)\varphi_{nj}^{1p}(\xi)d\xi + C_{nm}\cos(\mu_n)\int_a^b \xi\{\varphi_{nm}^0(\xi)\}^2 d\xi\right)\right]}{2A_{nm}k_{0,nm}\int_a^b \xi\left\{\varphi_{nm}^0(\xi)\right\}^2 d\xi\cos(\psi_n)} \end{aligned} \tag{3.27}$$

By substituting for *sine* instead of the *cosine* terms in the above Eq. (3.27), yields the second correction term in k_2. The unknown terms involving E_n is obtained by substituting Eq. (3.26) into the rigid boundary condition term in Eq. (3.8), and by using the orthogonality of the trigonometric and the Bessel functions:

$$\begin{aligned}
&e_n E_n \gamma_n'(r)\cos(\eta_n) + X_{nm}(r) + C_{nm}\left(\frac{\varphi^{0\prime\prime}_{nm}(r)}{2} - \frac{n^2}{r^2}\varphi^0_{nm}(r)\right)\left([*]_{2n}\cos(\mu_n) + [\bar{*}]_{2n}\sin(\mu_n)\right) = 0\\
&E_n \gamma_n'(r)\sin(\eta_n) + Y_{nm}(r) - C_{nm}\left(\frac{\varphi^{0\prime\prime}_{nm}(r)}{2} - \frac{n^2}{r^2}\varphi^0_{nm}(r)\right)\left([*]_{2n}\sin(\mu_n) - [\bar{*}]_{2n}\cos(\mu_n)\right) = 0
\end{aligned} \tag{3.28}$$

where,

$$\begin{aligned}
X_{nm}(r) &= \sum_{p=0}^{\infty} B_p\left[\left\{[*]_{n+p} + [*]_{|n-p|}\right\}\frac{\beta_p''(r)}{2} - p\left\{(n+p)[*]_{n+p} + (p-n)[*]_{|p-n|}\right\}\frac{\beta_p(r)}{2r^2}\right]\cos(\lambda_p)\\
&+ \sum_{p=0}^{\infty} B_p\left[\left\{[\bar{*}]_{n+p} + \frac{(p-n)}{|p-n|}[\bar{*}]_{|n-p|}\right\}\frac{\beta_p''(r)}{2} - p\left\{(n+p)[\bar{*}]_{n+p} + |p-n|[\bar{*}]_{|p-n|}\right\}\frac{\beta_p(r)}{2r^2}\right]\sin(\lambda_p)\\
&+ \frac{A_{nm}}{2}\left(2[\bullet]_0 + [\bullet]_{2n}\right)\varphi^{0\prime\prime\prime}_{nm}(r)\cos(\psi_n) + \frac{A_{nm}}{2}\left([\bar{\bullet}]_{2n}\right)\varphi^{0\prime\prime\prime}_{nm}(r)\sin(\psi_n)\\
&+ \frac{n^2 A_{nm}\varphi^0_{nm}(r)}{r^3}\left\{[\bullet]_{2n}\cos_(\psi_n) + [\bar{\bullet}]_{2n}\sin_(\psi_n)\right\};\\
r = a \text{ or } b;\ \ [*]\left([\bar{*}]\right) &= \begin{cases} F(\bar{F}) & : r = a \\ G(\bar{G}) & : r = b \end{cases};\ \ [\bullet]\left([\bar{\bullet}]\right) = \begin{cases} H(\bar{H}) & : r = a \\ I(\bar{I}) & : r = b \end{cases};\ \ e_n = \begin{cases} 2 & : n = 0 \\ 1 & : n \neq 0 \end{cases}
\end{aligned} \tag{3.29}$$

$$\begin{aligned}
Y_{nm}(r) &= \sum_{p=0}^{\infty} B_p\left[-\left\{[*]_{n+p} - [*]_{|n-p|}\right\}\frac{\beta_p''(r)}{2} + p\left\{(n+p)[*]_{n+p} - (p-n)[*]_{|p-n|}\right\}\frac{\beta_p(r)}{2r^2}\right]\sin(\lambda_p)\\
&+ \sum_{p=0}^{\infty} B_p\left[\left\{[\bar{*}]_{n+p} - \frac{(p-n)}{|p-n|}[\bar{*}]_{|n-p|}\right\}\frac{\beta_p''(r)}{2} - p\left\{(n+p)[\bar{*}]_{n+p} - |p-n|[\bar{*}]_{|p-n|}\right\}\frac{\beta_p(r)}{2r^2}\right]\cos(\lambda_p)\\
&+ \frac{A_{nm}}{2}\left(2[\bullet]_0 - [\bullet]_{2n}\right)\varphi^{0\prime\prime\prime}_{nm}(r)\sin(\psi_n) + \frac{A_{nm}}{2}\left([\bar{\bullet}]_{2n}\right)\varphi^{0\prime\prime\prime}_{nm}(r)\cos(\psi_n)\\
&- \frac{n^2 A_{nm}\varphi^0_{nm}(r)}{r^3}\left\{[\bullet]_{2n}\sin_(\psi_n) - [\bar{\bullet}]_{2n}\cos_(\psi_n)\right\};
\end{aligned} \tag{3.30}$$

Equations (3.25) and Eq. (3.27) are three linear simultaneous equations involving three unknowns C_{nm}, μ_n and k_2. By substituting Eq. (3.28) into Eq. (3.27), Eq. (3.25) and Eq. (3.27) may be

simplified to a matrix form as:

$$\begin{bmatrix} \frac{[\Omega_{nm}(b)G_{2n}-\Omega_{nm}(a)F_{2n}]}{e_n} - 2k_{0,nm}k_1\frac{\Lambda_{nm}}{A_{nm}} & [\Omega_{nm}(b)\bar{G}_{2n} - \Omega_{nm}(a)\bar{F}_{2n}] & -2k_{0,nm}\Lambda_{nm}\cos(\psi_n) \\ [\Omega_{nm}(b)\bar{G}_{2n} - \Omega_{nm}(a)\bar{F}_{2n}] - 2k_{0,nm}k_1\frac{\Lambda_{nm}}{A_{nm}} & -[\Omega_{nm}(b)G_{2n} - \Omega_{nm}(a)F_{2n}] & -2k_{0,nm}\Lambda_{nm}\sin(\psi_n) \\ -2k_{0,nm}\Lambda_{nm}\cos(\psi_n) & -2k_{0,nm}\Lambda_{nm}\sin(\psi_n) & 0 \end{bmatrix}$$

$$\times \begin{Bmatrix} C_{nm}\cos(\mu_n) \\ C_{nm}\sin(\mu_n) \\ k_2 \end{Bmatrix} = \begin{Bmatrix} k_1^2\Lambda_{nm}\cos(\psi_n) + k_1\frac{\Gamma_{nm}\cos(\psi_n)}{A_{nm}} + \frac{a\varphi^0_{nm}(a)}{e_n}X_n(a) - \frac{b\varphi^0_{nm}(b)}{e_n}X_n(b) \\ k_1^2\Lambda_{nm}\sin(\psi_n) + k_1\frac{\Gamma_{nm}\sin(\psi_n)}{A_{nm}} + a\varphi^0_{nm}(a)Y_n(a) - b\varphi^0_{nm}(b)Y_n(b) \\ \Gamma_{nm} \end{Bmatrix} \tag{3.31}$$

where, $r = a$, or b; $\Omega_{nm}(r) = r\varphi^0_{nm}(r)\left(\frac{\varphi^{0\prime\prime}_{nm}(r)}{2} - \frac{n^2}{r^2}\varphi^0_{nm}(r)\right)$

$$\Lambda_{nm} = A_{nm}\int_a^b \xi\{\varphi^0_{nm}(\xi)\}^2 d\xi; \quad \Gamma_{nm} = 2k_{0,nm}A_{nm}\left(\sum_{j=1}^{\infty} D_{nm,j}\int_a^b \xi\varphi^0_{nm}(\xi)\varphi^{1p}_{nj}(\xi)d\xi\right) \tag{3.32}$$

The solution of Eq. (3.31) completes the first order eigensolutions. It also provides a second order correction to the radial wave number. Using a procedure analogous to that outlined above, the complete solution to the second order eigenfunctions may be derived. However the higher order solutions become cumbersome and may not be useful, especially when an approximate understanding of the problem is more desirable than getting a more accurate solution. The present formulations is therefore restricted to a first order approximation to the eigenfunctions (and hence a second order approximation to the wave number). The error in the solutions due to such truncations is compared with numerical results.

The focus of the present work is on studying the TL in mufflers with elliptic chambers (within moderate eccentricity limits). In the context of elliptic geometries, it is worthwhile to present some simplifications to the above general formulations. For an elliptic cavity, it may be observed that the Fourier expansion terms $\bar{F}, \bar{G}, \bar{H}$ and $\bar{I}$, are identically zero. Since these terms are zero, it may be shown that the phase terms ψ, λ, and μ are either zero or $\pi/2$. Hence, for

$n \neq 0$, the eigenfunctions are of the either form:

$$\phi_{nm} = A_{nm}\varphi^0_{nm}(r)\cos(n\theta) + \varepsilon\sum_{s=0}^{\infty} B_s\beta_s(r)\cos(s\theta) + \varepsilon\left(C_{nm}\varphi^0_{nm}(r) + \sum_{j=1}^{\infty} D_{nm,j}\varphi^{1p}_{nj}(r)\right)\cos(n\theta)$$

$$k_{r,nm} = k_{0r,nm} + \varepsilon k_{1,nm}\big|_{\psi=0} + \varepsilon^2 k_{2,nm}\big|_{\psi=0}$$

$$\phi_{nm} = \bar{A}_{nm}\varphi^0_{nm}(r)\sin(n\theta) + \varepsilon\sum_{s=0}^{\infty} \bar{B}_s\beta_s(r)\sin(s\theta) + \varepsilon\left(\bar{C}_{nm}\varphi^0_{nm}(r) + \sum_{j=1}^{\infty} \bar{D}_{nm,j}\varphi^{1p}_{nj}(r)\right)\sin(n\theta)$$

$$k_{r,nm} = k_{0r,nm} + \varepsilon k_{1,nm}\big|_{\psi=\pi/2} + \varepsilon^2 k_{2,nm}\big|_{\psi=\pi/2} \tag{3.33}$$

3.2 Numerical verification: TL in expansion chamber elliptic mufflers

The numerical accuracy of the method is demonstrated by determining natural frequencies and TL of an elliptical muffler with eccentricity varying between $0.4 \sim 0.6$. The results are compared to exact solutions for such cross–sections [31, 33, 34]. The exact solutions were developed by solving the wave equation in an elliptical coordinate system. For the present analysis, four different muffler configurations are considered for comparison (Fig. 3.2): (a) Concentric chamber muffler (b) Concentric-inlet-offset-outlet muffler (c) Reversing chamber muffler (d) End-inlet-side-outlet (EISO) muffler. For all mufflers, dimensions of major/minor axes at different eccentricities are derived such that the area of cross–section is constant. This area of cross–section corresponded to a circle of radius $0.09\ m$. The inlet and outlet ports are $d = 0.033\ m$ in diameter. Two muffler lengths $L = 0.10\ m$, and $L = 0.25\ m$ are considered. The offset distance is $0.05\ m$. For the EISO muffler, the outlet port is located at a distance of $L_1 = L/2$ from inlet port. The speed of sound is taken as $c = 340\ ms^{-1}$.

3.2.1 Validation of the perturbation method with exact solutions

The Green's function method discussed in section 2.1 is employed for determining the TL in elliptic mufflers. The TL curves for different muffler lengths, inlet/outlet locations, and eccentricities are presented in Figs. 3.3–3.6. For comparison, TL curves obtained through exact solution of Helmholtz equation in an elliptical domain are also plotted. The perturbation results may be seen

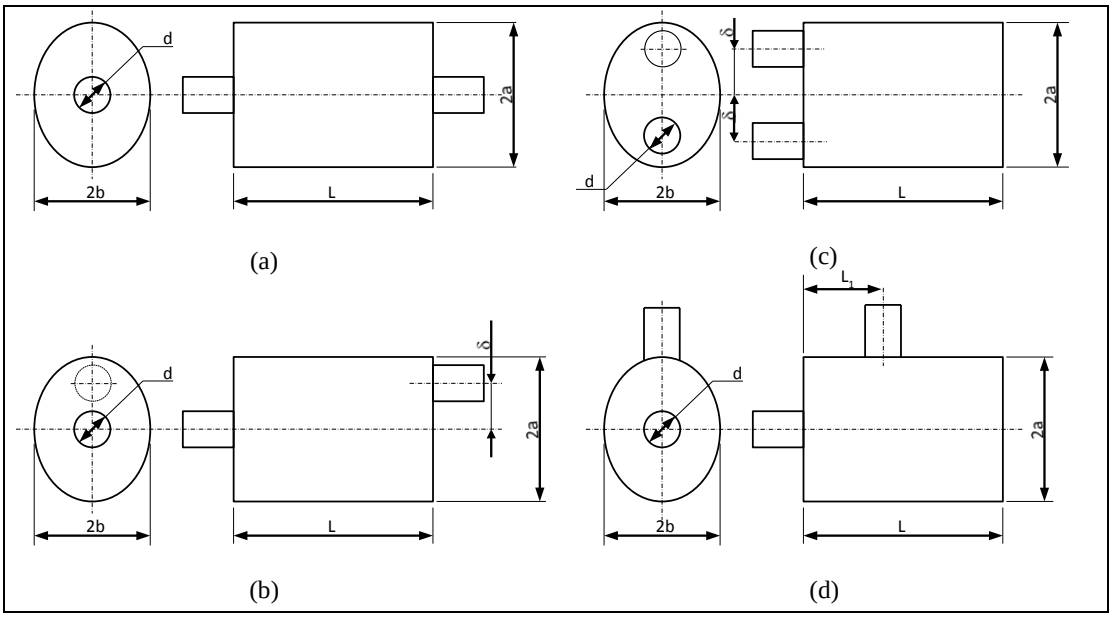

Figure 3.2: Schematic diagram of elliptical mufflers with different inlet/outlet configurations: (a) Concentric chamber muffler (b) Concentric-inlet-offset-outlet muffler (c) Reversing chamber muffler (d) End-inlet-side-outlet (EISO) muffler.

to agree well with the exact solutions for all muffler orientations. The maximum departure from exact solution is about 3 dB (ignoring resonating peaks). Except for reversing chamber muffler, locations of inlet and outlet ports in all other mufflers ensure modes that are symmetric about both axes of the ellipse only can propagate. The even modes of type $(2j, k)$ $j = 0, 1, 2, \cdots$ $k = 1, 2, \cdots$ are symmetric about the axes. Consequently, near propagation of first such transverse mode ((2, 1) even mode), TL curves show significant deterioration. In the frequency range of interest, next such higher order propagating mode is (0, 2) even mode. The offset location of ports in reversing chamber muffler causes excitation of all even modes above their cutoff frequency. As a result, reversing chamber muffler shows poorer sound attenuation characteristic in comparison to other configurations, since the (1, 1) even mode starts to propagate at much lower frequency compared to (2, 1) even mode. For EISO muffler, location of outlet port from inlet port results in a broadband sound attenuation.

In Fig. 3.7, mode shapes for first few even modes have been compared to the exact solution. Within the frequency range of interest ($\sim$3000 Hz), only modes that are expected to influence

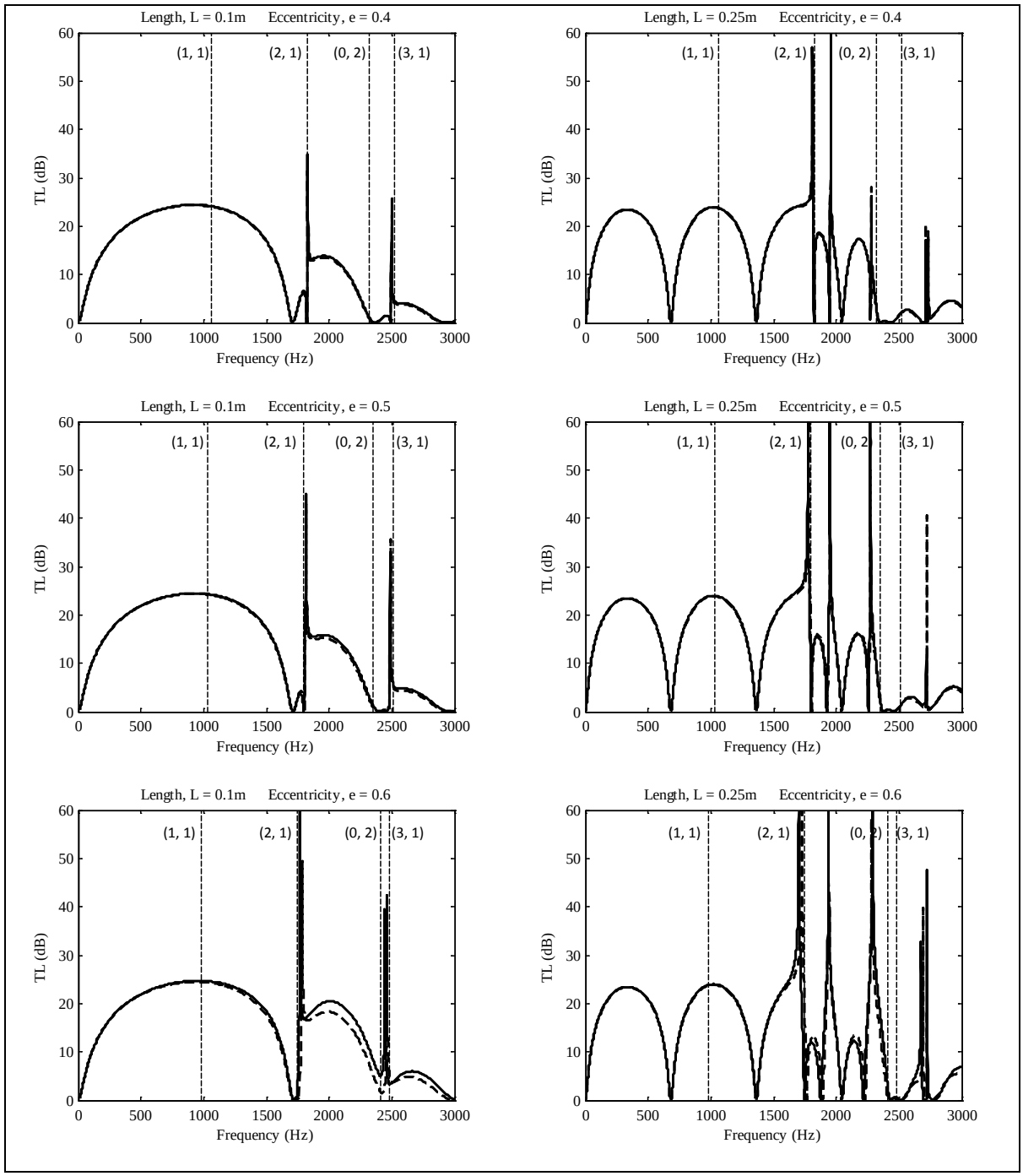

Figure 3.3: Transmission loss characteristics at different eccentricities (e), and chamber lengths (L) for concentric chamber configuration. $\cdots\cdots$, Perturbation solution; ——— Exact solution.

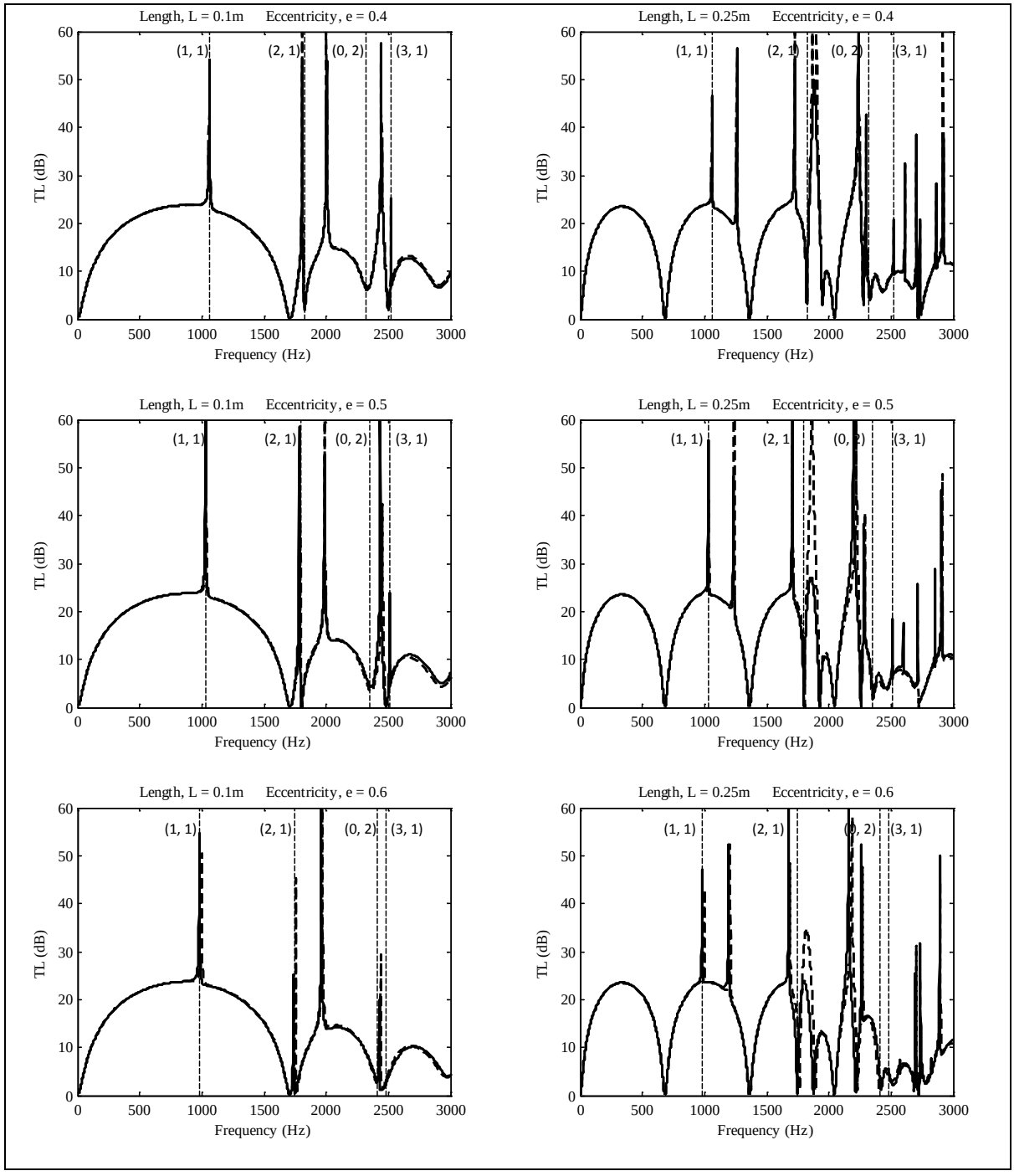

Figure 3.4: Transmission loss characteristics at different eccentricities (e), and chamber lengths (L) for concentric-inlet-offset-outlet chamber configuration. · · · · · · ·, Perturbation solution; ——— Exact solution.

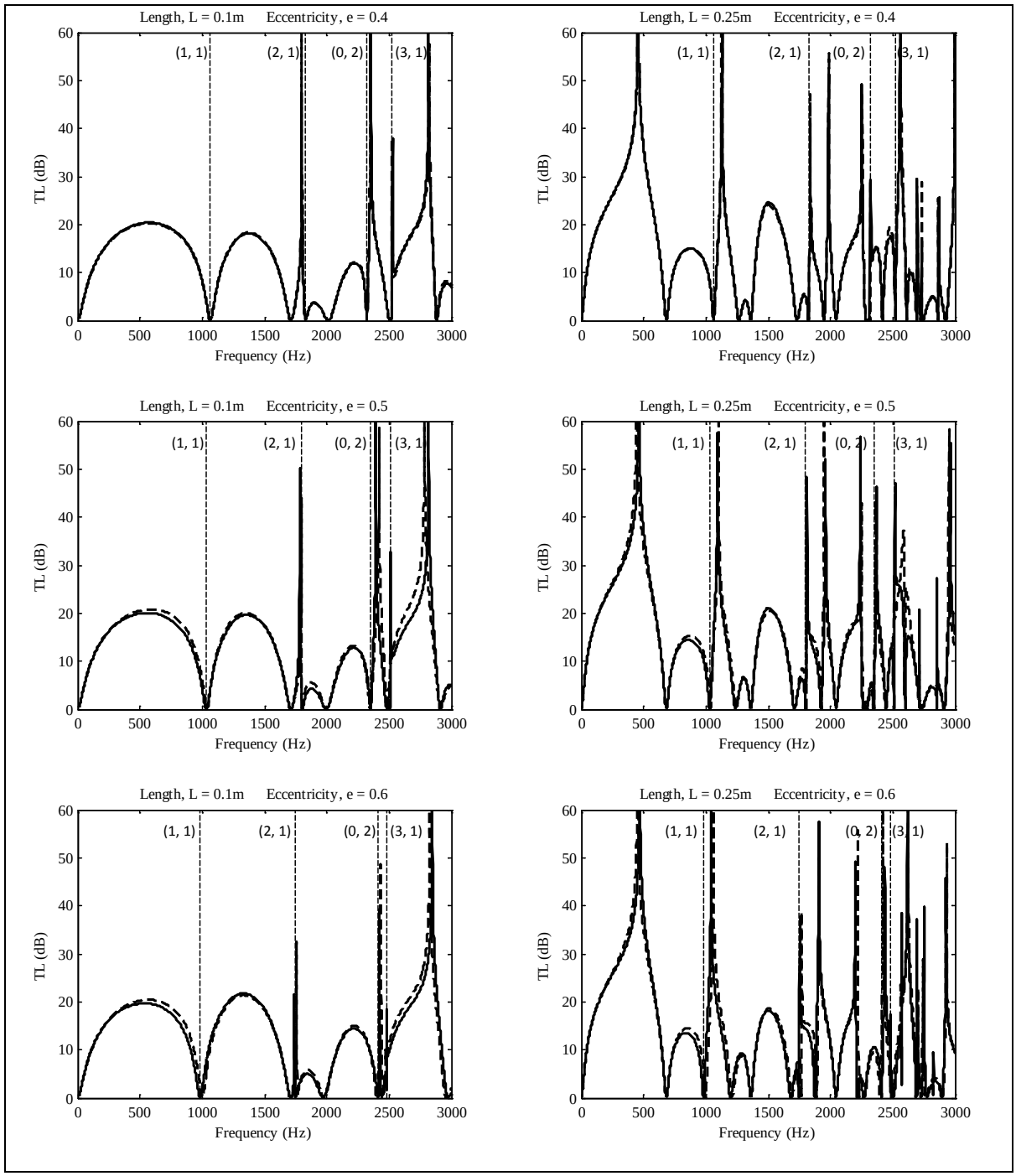

Figure 3.5: Transmission loss characteristics at different eccentricities (e), and chamber lengths (L) for reversing chamber configuration. · · · · · · ·, Perturbation solution; ——— Exact solution.

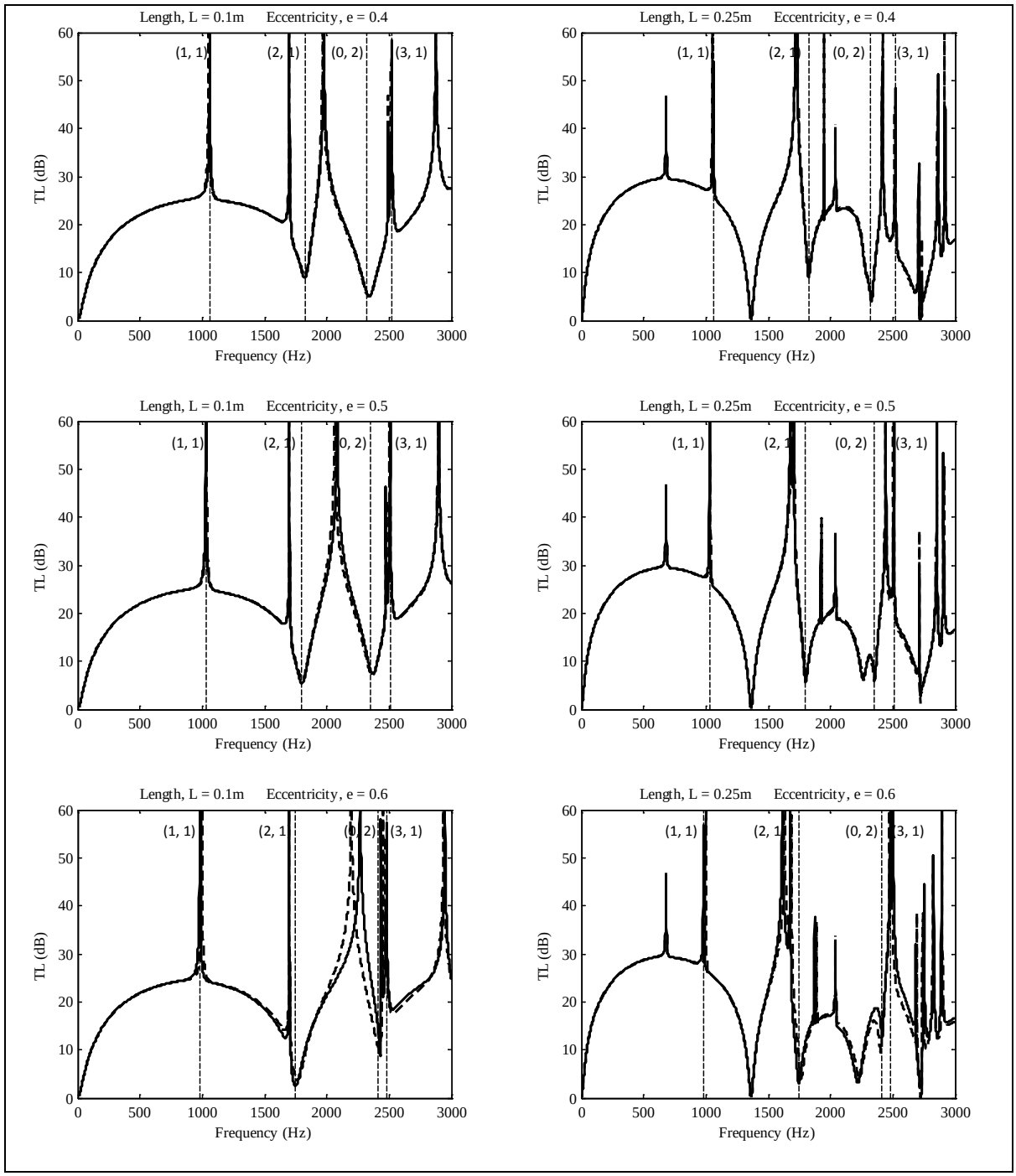

Figure 3.6: Transmission loss characteristics at different eccentricities (e), and chamber lengths (L) for EISO chamber configuration. · · · · · · ·, Perturbation solution; ——— Exact solution.

the TL in the mufflers (Fig. 3.2) have been shown. The (0, 1) and (1, 1) even modes have not been presented as the comparison was trivial. In a circular chamber muffler the nodal diameters pass through the center, thereby suppressing the propagation of such modes in a concentric-inlet (or outlet) muffler configuration. As is evident from Fig. 3.7, some of the nodal diameters in an elliptic muffler are located at an offset from the center, therefore causing the propagation of certain higher order modes which would not have propagated in a circular muffler with similar inlet/outlet configuration. The (2, 1) even mode is the first such mode which propagates in an ellipse, resulting in a poorer sound attenuation compared to an equivalent circular muffler.

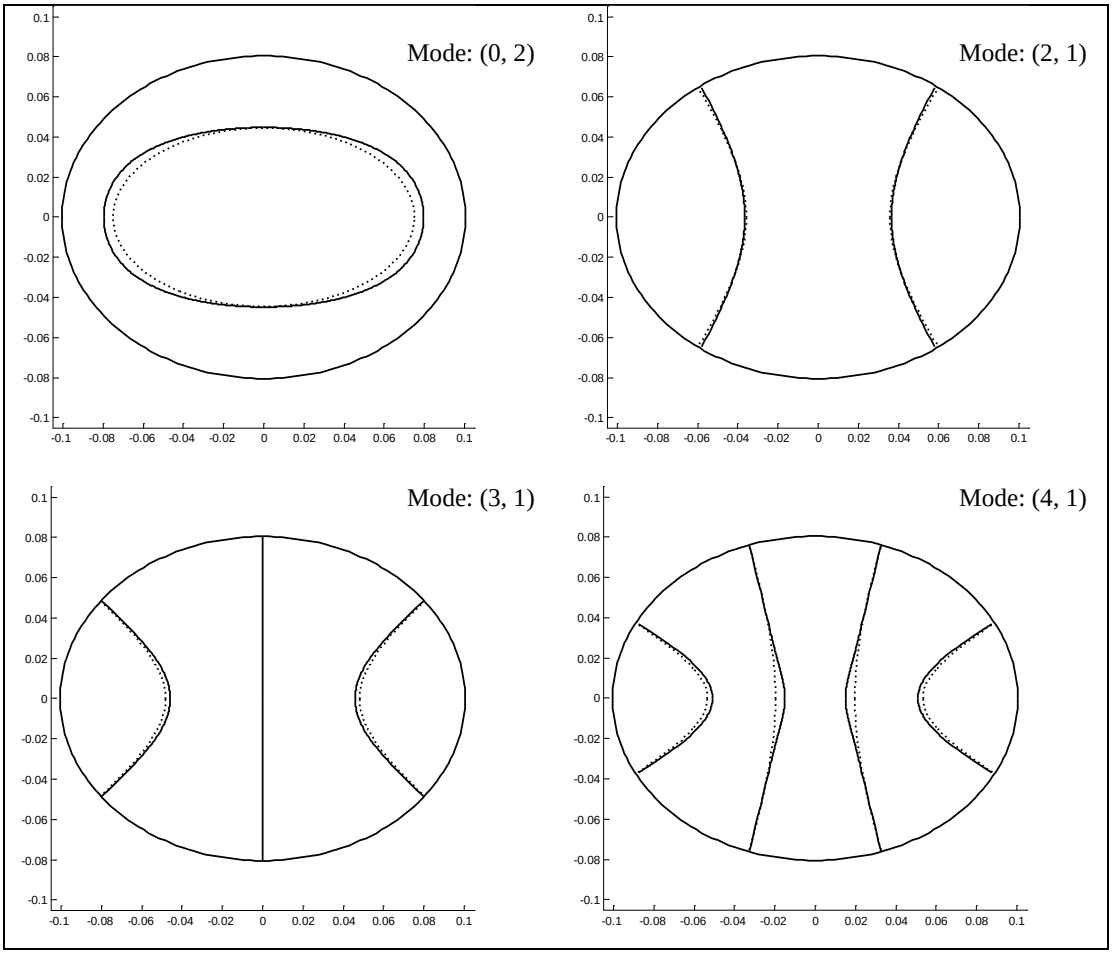

Figure 3.7: Cross-section view of even mode shapes of ellipse with eccentricity, · · · · · · ·, Perturbation solution; ——— Exact solution.

In Table 3.1 and Table 3.2, comparison of natural frequencies for different modes is presented. It is observed that the natural frequency of an odd mode is higher than the corresponding even mode. Hong and Kim [30] argued that such behavior was due to the relative time taken by waves to travel across the axes. Even modes traveling along the minor axis require more time to propagate; hence a lower natural frequency results. In general, the perturbation results show good agreement with exact solutions. However, at some higher modes, significant departure from the exact solutions (e.g. (2, 3) even mode) are observed. This deviation may be attributed to the fact that assumption of uniformly valid asymptotic expansion might not hold true for these modes. Approximation to eigensolutions is influenced by geometric perturbations. Therefore, depending on the nature of asymmetry, only certain higher order modes show significant departure from the exact solution. This behavior is evident from Table 3.1, where the $(2, n)$ even mode, $n > 1$, modes show considerable departure in comparison to other higher order modes. Parker and Mote [75], studied the cause of such divergences for a plate vibration problem involving perturbed eigenfunctions solutions. Using a procedure similar to one presented in this paper, they showed that the solutions converge. However, natural frequencies up to (1, 3) mode was reported in their work, rendering any qualitative comparison of the divergence with present work improbable. Propagation of higher order modes in a muffler adversely affects sound at-

Table 3.1: Comparison of cut-off frequency (Hz) of different even modes at various eccentricities. Area of cross section is same as a circle of radius 0.09 m for all cases.

Mode	FEM	Analytical	% Diff.
(0, 1)	0	0	–
(0, 2)	2602.2	2604.9	0.10
(0, 3)	4839.4	4846	0.14
(1, 1)	942.4	924	-1.99
(1, 2)	2941.1	2905.7	-1.22
(1, 3)	5147.4	5169.4	0.43
(2, 1)	1781.7	1770.4	-0.64
(2, 2)	3944.5	3936.6	-0.20
(2, 3)	6089.1	6436.9	5.40
(3, 1)	2460.9	2463.6	0.11
(3, 2)	4554.9	4459.8	-2.13
(3, 3)	6657.2	6773.1	1.71

Table 3.2: Comparison of cut-off frequency (Hz) of different even modes at various eccentricities. Area of cross section is same as a circle of radius 0.09 m for all cases.

Mode	FEM	Analytical	% Diff.
(0, 1)	0	0	–
(0, 2)	2602.2	2604.9	0.10
(0, 3)	4839.4	4846	0.14
(1, 1)	942.4	924	-1.99
(1, 2)	2941.1	2905.7	-1.22
(1, 3)	5147.4	5169.4	0.43
(2, 1)	1781.7	1770.4	-0.64
(2, 2)	3944.5	3936.6	-0.20
(2, 3)	6089.1	6436.9	5.40
(3, 1)	2460.9	2463.6	0.11
(3, 2)	4554.9	4459.8	-2.13
(3, 3)	6657.2	6773.1	1.71

tenuation. In most muffler applications, design conditions limit the frequency range to first few higher order modes. Therefore, deviation in higher order eigensolutions does not induce any significant error in TL curves, as is evident from Figs. 3.3–3.6. However, for acoustically short mufflers, higher order modes generated at duct discontinuities do not completely decay. These evanescent modes may interact with plane-wave modes giving rise to TL characteristics different from a long-chamber muffler.

3.2.2 Parametric study: improved sound attenuation

From Figs. 3.3–3.6, it is evident that the propagation of first few higher order transverse modes causes significant decrease in sound attenuation characteristics. In most muffler designs, the propagation of a higher order mode may be suppressed by positioning the inlet and/or the outlet port at a pressure node corresponding to the particular mode of interest. Hence from a design perspective, it is important to determine the natural frequency and nodal positions of higher order modes. For rigid circular geometries the radial wavenumber when non-dimensionalized w.r.t. the radius, yields a constant value which depends on the mode number; thereby providing a convenient way of determining the natural frequency. For an elliptic geometry, the determination of the radial wave number is more involved (due to the eccentricity of the geometry). In

order to aid easy determination of the natural frequency, a curve-fit for the first few higher order modes is presented in Fig. 3.8. The radial wavenumber is non-dimensionalized w.r.t. the mean radius a of the perturbed geometry. The variation of the non-dimensional wavenumber is plotted for eccentricities varying from 0.2 to 0.6. The equation for the curve-fit is given by Eq. (3.34)

$$
\begin{aligned}
(k_r a)_{(1,1)} &= -4.889\exp^6 + 8.657\exp^5 - 7.341\exp^4 + 3.027\exp^3 - 1.156\exp^2 + 0.0937\exp^1 + 1.841 \\
(k_r a)_{(2,1)} &= -14.786\exp^6 + 26.310\exp^5 - 22.075\exp^4 + 9.217\exp^3 - 2.234\exp^2 + 0.285\exp^1 + 3.054 \\
(k_r a)_{(0,2)} &= 11.976\exp^6 - 20.727\exp^5 + 17.418\exp^4 - 7.147\exp^3 + 1.724\exp^2 - 0.219\exp^1 + 3.832 \\
(k_r a)_{(3,1)} &= -14.277\exp^6 + 26.139\exp^5 - 21.647\exp^4 + 9.261\exp^3 - 2.253\exp^2 + 0.289\exp^1 + 4.201
\end{aligned}
\tag{3.34}
$$

It can be observed from Eq. (3.34) that as the eccentricity approaches zero, the non-dimensional wavenumber correspond to that of a circle of radius a.

The propagation of the (2, 1) even mode resulted in a decrease in TL for most of the muffler configurations considered in Fig. 3.2. The propagation of the (2, 1) even mode may be prevented by positioning the center of the inlet/outlet port on the nodal line ($ABCDE$ or $A'B'C'D'E'$ on Fig. 3.9) corresponding to this mode. In Fig. 3.10, the locus of the nodal position on the major-axis (point C or C' on Fig. 3.9) for the (2, 1) mode is presented. The TL curve for a concentric-inlet-offset-outlet muffler with the outlet port located at this nodal point is presented in Fig. 3.11. It can be observed that when the length of the muffler is $L = 0.25$ m, the TL curve in Fig. 3.11 shows a broadband sound attenuation patter below the cutoff frequency of the (0, 2) even mode, therefore extending the effectiveness of the muffler beyond the cutoff frequency of the (2, 1) mode. In the present configuration, when the length of the muffler is $L = 0.1$ m, the first axial cutoff frequency is very close to the (2, 1) cutoff frequency; hence no significant improvement is observed.

$$
\begin{aligned}
\delta/a &= -2.532\exp^6 + 4.311\exp^5 - 2.112\exp^4 + 0.368\exp^3 + 0.0639\exp^2 - 0.0198\exp^1 + 0.628 \\
\theta &== -15.058\exp^6 + 29.836\exp^5 - 21.099\exp^4 + 6.458\exp^3 - 1.033\exp^2 + 0.019\exp^1 + 0.786
\end{aligned}
\tag{3.35}
$$

In Fig. 3.9, the curve $BFDD'F'B'B$ corresponds to the pressure node of the (0, 2) even mode. It can be observed that the (2, 1) and the (0, 2) nodal curves intersect at points B, D, D' and B'. If the

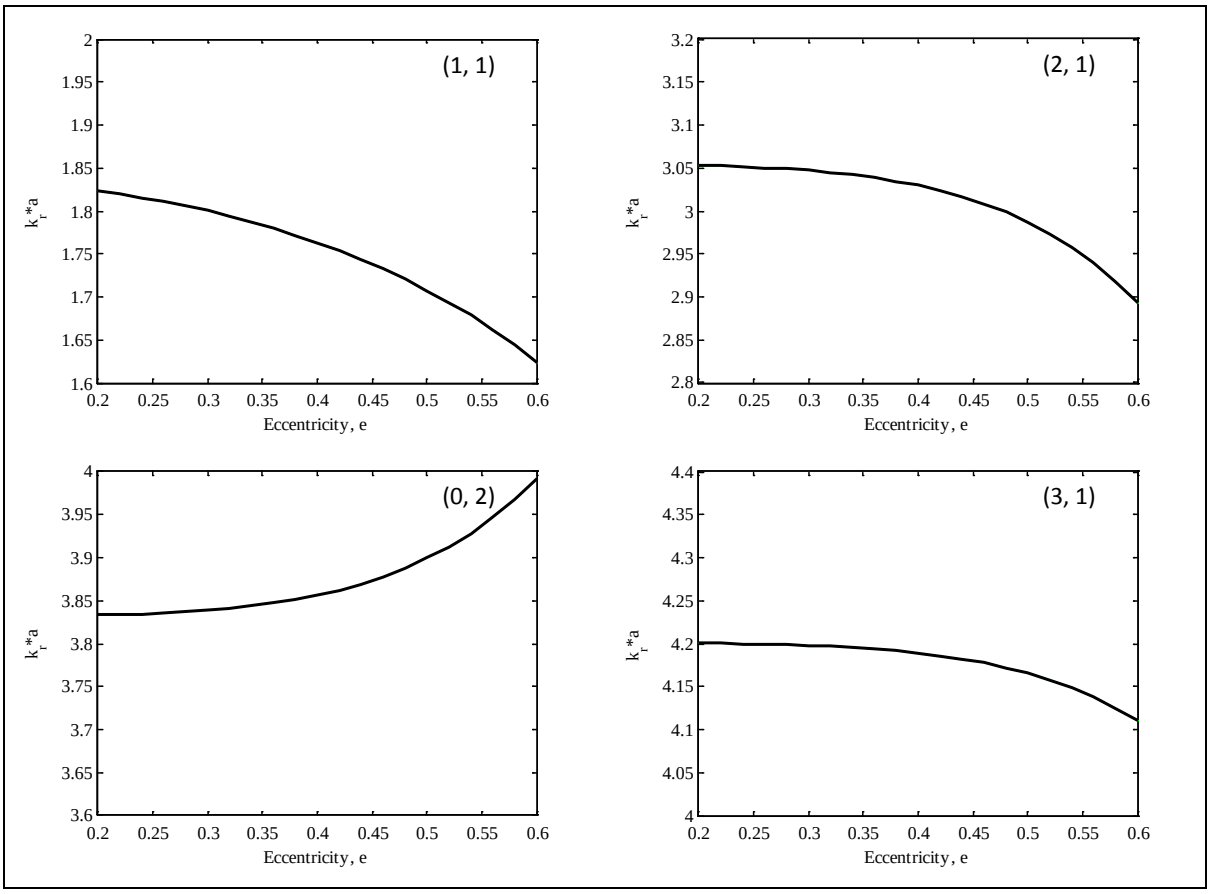

Figure 3.8: Variation of the non-dimensional radial wavenumber with eccentricity, for various even order modes.

outlet port of the muffler is centered at one of these points, and the inlet is located at the center of the ellipse (or vice versa), then all the higher order modes up to the (0, 2) even mode will get suppressed, thereby resulting in a broadband attenuation pattern (see Fig. 3.12). In Fig. 3.13, the radial distance of point B from the center of the ellipse, and its angular position is presented as a function of the eccentricity. By using a sixth order polynomial, variation of this nodal point with the eccentricity is given by Eq. (3.35) The suppression of the (2, 1) and the (0, 2) mode may similarly be extended to a reversing chamber muffler. However, the close proximity of inlet and outlet port may result in significant increase in backpressure. For the EISO muffler configuration, the (2, 1) and the (0, 2) mode cannot be suppressed, thereby limiting its use to a lower frequency range.

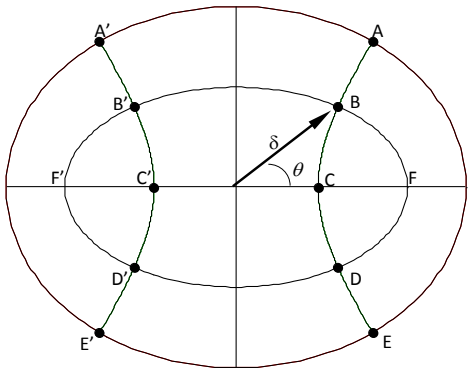

Figure 3.9: Locus of the pressure nodes for the (2, 1) and the (0, 2) even modes: $ABCDE$, $A'B'C'D'E'$ are the pressure nodal lines for the (2, 1) mode; $BFDD'F'B'B$ is the pressure nodal circle for the (0, 2) mode.

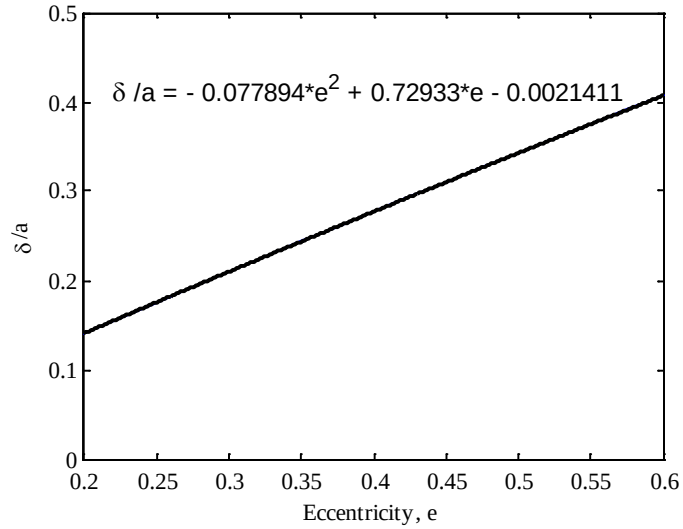

Figure 3.10: Locus of the (2, 1) pressure nodal point on the major-axis of the ellipse as a function of eccentricity.

3.3 Numerical implementation: TL in extended tube elliptic chamber mufflers

The mathematical model developed in the previous section is implemented to study the TL in an elliptic chamber muffler with extended inlet/outlet ports. The Mode Matching Method

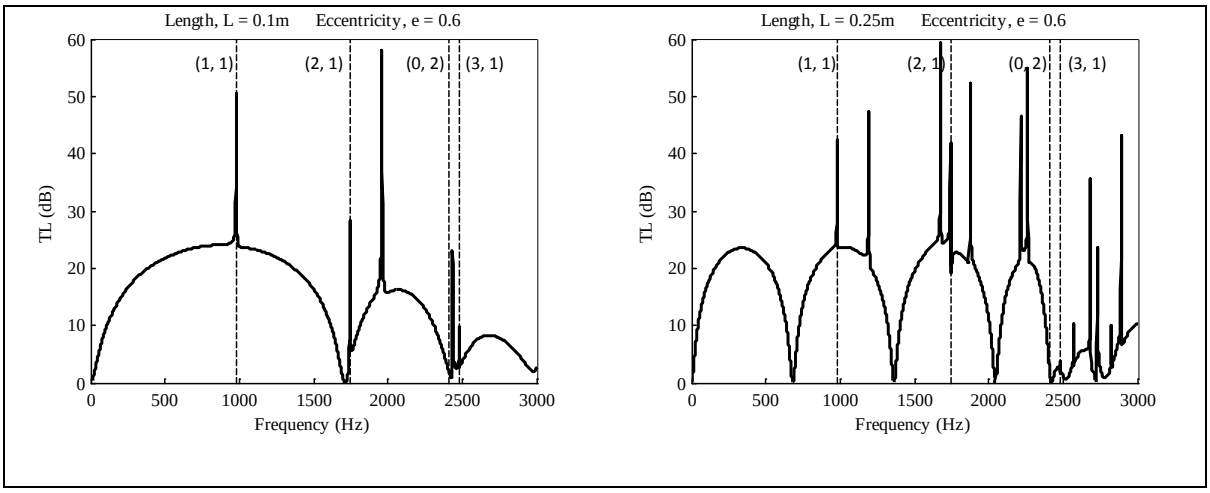

Figure 3.11: Transmission loss characteristics at different chamber lengths (L) for the concentric-inlet-offset-outlet chamber configuration; the outlet port is located at the (2, 1) pressure node on the major-axis.

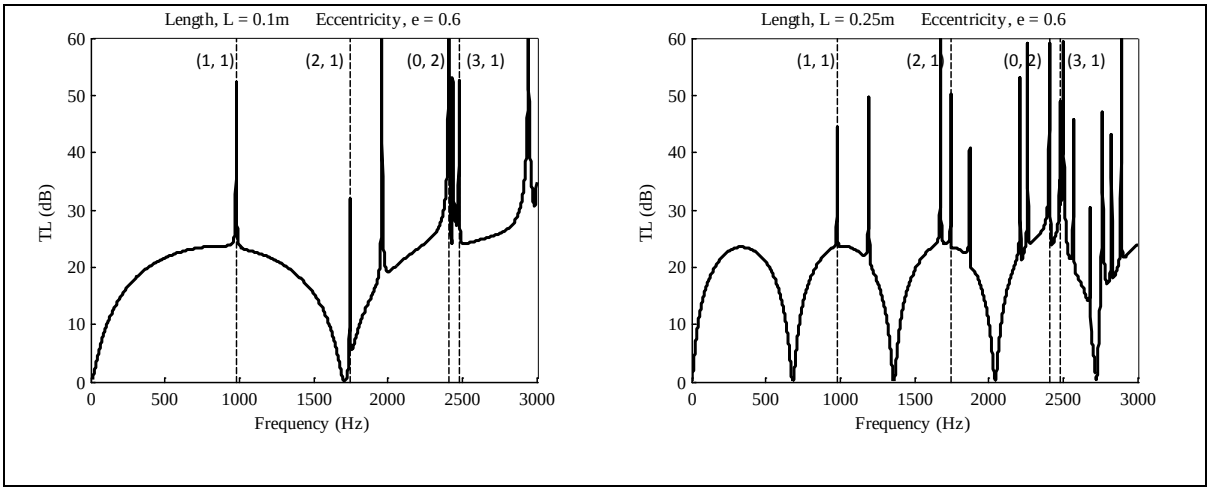

Figure 3.12: Transmission loss characteristics at different chamber lengths (L) for the concentric-inlet-offset-outlet chamber configuration; the outlet port is located at the intersection of the (2, 1) and the (0, 2) pressure node.

(MMM) discussed in section 2.1 is used for deriving the TL. The length of the chamber, L is 25 cm; the inlet and the outlet ports have diameters, $d_1 = d_2 = 3.3$ cm. The chamber has an eccentricity, $e = 0.6$, and the semi-major axis, $a = 10$ cm. In Figs. 3.14-3.16 , the TL for various

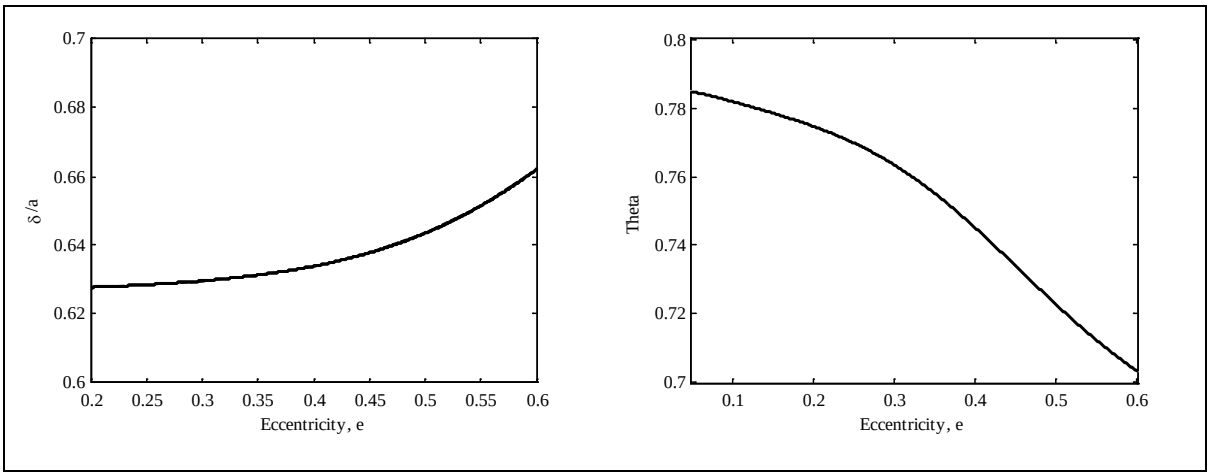

Figure 3.13: Radial distance δ and angular position θ, of the point of intersection of the (2, 1), and (0, 2) even modes.

duct extends are presented. In order to compare the accuracy of the mathematical model, results from a finite element (FEM) simulation is also presented. The transverse natural frequencies for various higher order even modes for the chamber are given in Tables 3.3-3.4. As can be observed from the figures and the tables, errors due to truncating the eigenfunctions to first order and the wave numbers to second order are small within the desired frequency range. Some of the higher order wave numbers (e.g. (2, 2) even mode in Table 3.3), show significant deviation from the FEM results. However, these higher order modes are cut-on at comparably larger frequencies and therefore have diminishing effects at lower frequencies, especially in an acoustically long muffler.

From Figs. 3.14–3.16 it can be observed that the TL curve is characterized by the presence of domes and resonating peaks. These domes are usually observed in acoustically long expansion chamber mufflers; the number of repeating domes depends on the cutoff frequency of the first higher order propagating mode, and on the length of the chamber [24]. The resonating peaks in the TL curves for an extended chamber muffler results in better sound attenuation in comparison to the dome-shaped TL curves in expansion chamber mufflers. The location of the resonating peaks depends on the length of the duct extends. Qualitatively, the annular region surrounding the extended part of the duct may be imagined as a side branch resonator (of length L_B or L_D), thereby leading to a resonating peak corresponding to an odd multiple of a quarter wavelength

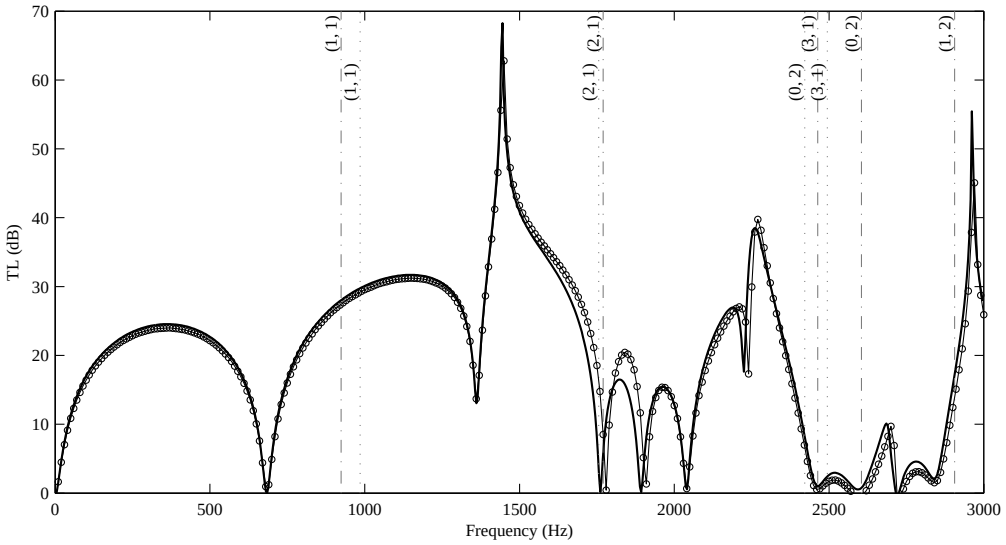

Figure 3.14: TL in an elliptic chamber muffler with extended inlet/outlet ports: $L = 25$ cm, $L_B = 10$ cm, $L_D = 0$ cm, $d_1 = d_2 = 3.3$ cm, $e = 0.6$, $a = 10$ cm; ———, Perturbation result; ~~o o o o o~~, FEM result.

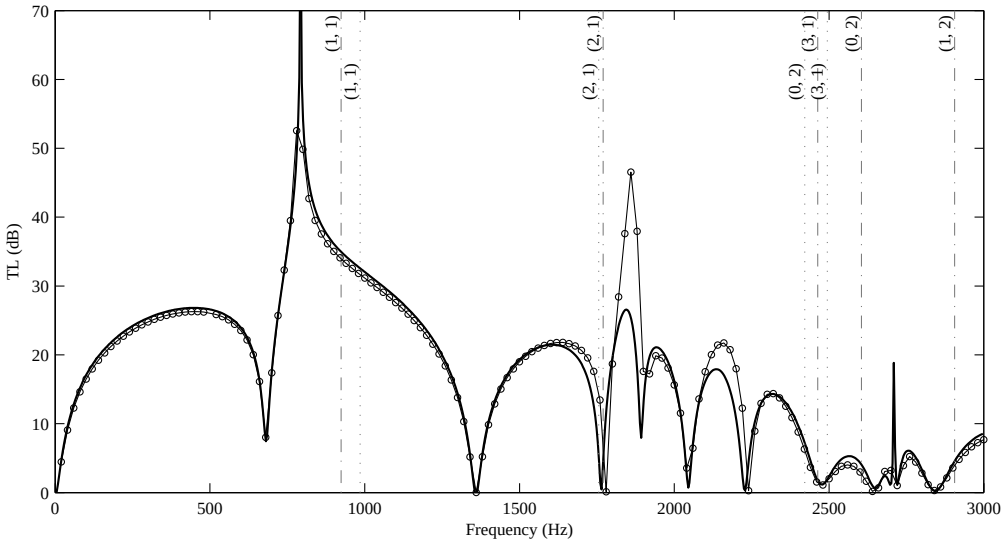

Figure 3.15: TL in an elliptic chamber muffler with extended inlet/outlet ports: $L = 25$ cm, $L_B = 10$ cm, $L_D = 0$ cm, $d_1 = d_2 = 3.3$ cm, $e = 0.6$, $a = 10$ cm; ———, Perturbation result; ~~o o o o o~~, FEM result.

($f = c/4L_B$). This observation can be substantiated from Fig. 3.15, where a resonating peak occurs close to 850 Hz (c = 340 m/s), which corresponds to the resonating peak for a side branch resonator of length 10 cm. However, the location of the peaks are not exactly at the quarter wavelength frequencies. The shift in the resonating peaks occurs due the non-decaying effects of evanescent higher order modes. At low frequencies, these higher order modes have much

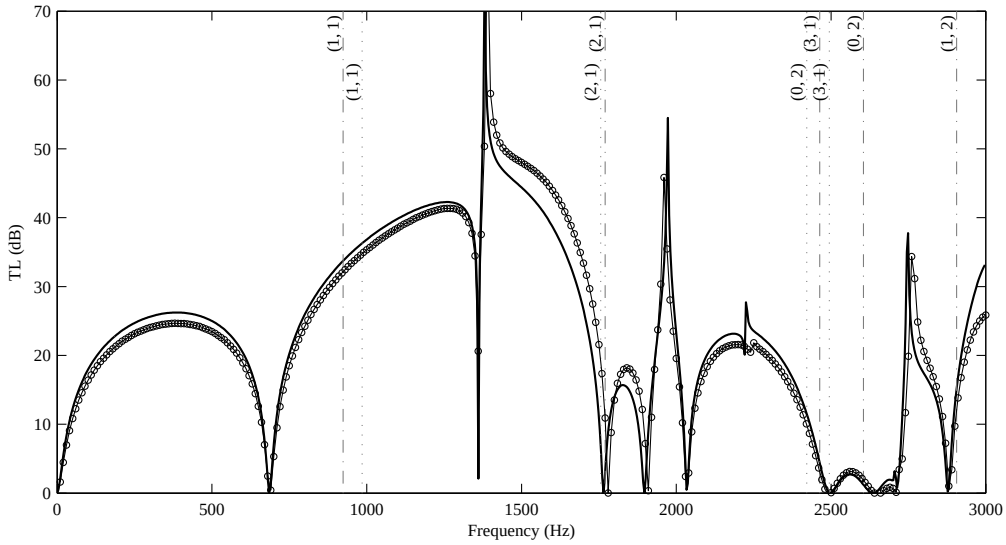

Figure 3.16: TL in an elliptic chamber muffler with extended inlet/outlet ports: $L = 25$ cm, $L_B = 5$ cm, $L_D = 5$ cm, $d_1 = d_2 = 3.3$ cm, $e = 0.6$, $a = 10$ cm; ———, Perturbation result; ~~o o o o~~, FEM result.

smaller effects on the overall TL, and hence the resonating peaks are much closer to the quarter wavelength frequencies. At higher frequencies, the evanescent modes considerably shift the location of the resonating peaks from the quarter wavelength frequencies, as can be observed from Fig. 3.15.

In the present muffler configuration, the first higher order propagating mode is the (2, 1) even mode having a cutoff frequency of 1755.7 Hz. The propagation of this mode above the cutoff frequency results in a dip in the TL curves, thereby affecting the sound attenuation in such geometries. Except for the (0, 2) mode, the other higher order modes as shown in Figs. 3.14–3.16 are non-propagating, and hence do not affect the TL curve. In comparison, the first higher order propagating mode in a circular chamber extended muffler is the (0, 2) transverse mode instead of the (2, 1) mode; the cutoff frequency being approximately 2500 Hz for same average radius. Therefore, for similar dimensions, the circular cylinder extended muffler is useful over a wider frequency range that the corresponding elliptic chamber extended muffler. The reason for the (2, 1) mode being a propagating mode in the elliptic configurations, and non-propagating for the circular cylinder may be explained in terms of the location of the nodal diameters for these modes. For an elliptic geometry, the (2, 1) nodal diameters are located at an offset from the center. The inlet/outlet ports being concentric, there is a net energy transfer by the (2, 1) mode when they are cut-on. However, the (2, 1) nodal diameters for the cylindrical chamber pass through

Table 3.3: Natural frequencies of different even modes for the annular elliptic chamber

Mode	FEM	Analytical	% Diff.
(0, 1)	0	0	–
(0, 2)	2602.2	2604.9	0.10
(0, 3)	4839.4	4846	0.14
(1, 1)	942.4	924	-1.99
(1, 2)	2941.1	2905.7	-1.22
(1, 3)	5147.4	5169.4	0.43
(2, 1)	1781.7	1770.4	-0.64
(2, 2)	3944.5	3936.6	-0.20
(2, 3)	6089.1	6436.9	5.40
(3, 1)	2460.9	2463.6	0.11
(3, 2)	4554.9	4459.8	-2.13
(3, 3)	6657.2	6773.1	1.71

Table 3.4: Natural frequencies of different even modes for the elliptic chamber

Mode	FEM	Analytical	% Diff.
(0, 1)	0	0	–
(0, 2)	2410.1	2421.4	0.47
(0, 3)	4546.1	4890.5	7.04
(1, 1)	1004.2	985.4	-1.91
(1, 2)	3118.1	3093.1	-0.81
(1, 3)	5205.9	5177.2	-0.55
(2, 1)	1774.8	1755.7	-1.09
(2, 2)	3873.7	3520.3	-10.04
(2, 3)	5896.3	4394.4	-34.18
(3, 1)	2489.9	2494.2	0.17
(3, 2)	4650	4645	-0.11
(3, 3)	6616.3	6348	-4.23

the center and make an angle of $\pi/4$ with each other, resulting a net zero energy transfer for the concentric inlet/outlet configurations.

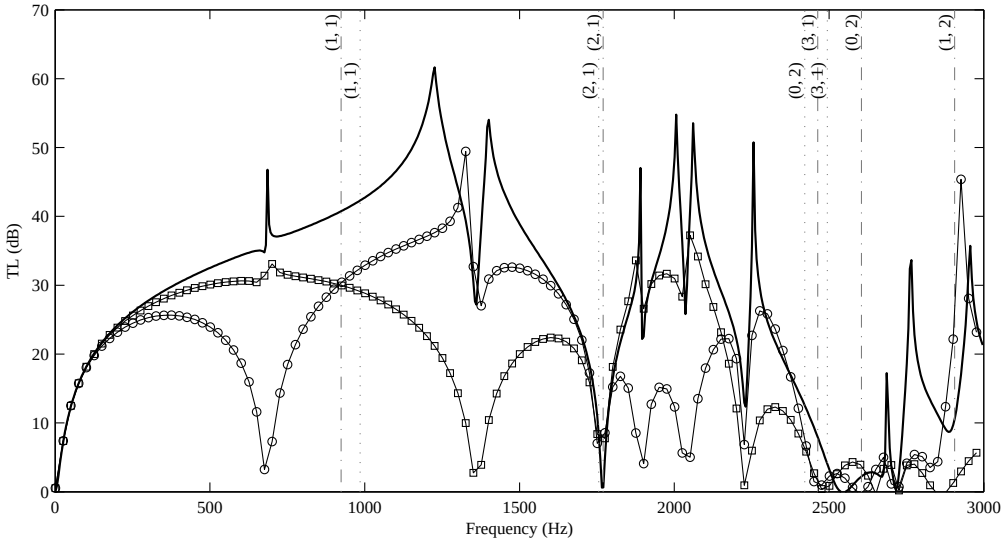

Figure 3.17: TL in an elliptic chamber muffler with extended inlet/outlet ports: $L = 25$ cm, $d_1 = d_2 = 3.3$ cm, $e = 0.6$, $a = 10$ cm; ~~o o o o o~~, $L_B = 5.5$ cm, $L_D = 0$ cm; ~~□ □ □ □ □~~, $L_B = 11.6$ cm, $L_D = 0$ cm; ———, $L_B = 11.6$ cm, $L_D = 5.5$ cm.

In Fig. 3.17, a parametric study involving different inlet/outlet duct extends are presented

for improved attenuation characteristics below the (2, 1) cutoff frequency. The improvement in the sound attenuation in the TL curves is achieved by determining the length of the duct extends such that the resonating peaks correspond to the zero attenuation frequencies (f = multiples of $c/2L$) for the muffler. The length of the duct extends based on the quarter wavelength frequencies act as an initial guess for further refinement. As can be observed from Fig. 3.17, a broadband sound attenuation is possible by properly selecting the length of the duct extends.

3.4 Summary

A perturbation based approach has been implemented in order to study the TL in moderately eccentric elliptic chamber mufflers with extended inlet and outlet. The annular regions formed by the inlet/outlet ports and the chamber are non-confocal, thereby making it impossible to formulate an exact analytical solutions in terms of the elliptical eigenfunctions. In order to circumvent this limitation, a regular perturbation method is employed to derive the eigensolutions for the entire muffler domain. The mathematical formulation for the eigensolutions are general, and can be employed for any small symmetric/asymmetric distortions from a cylindrical geometry. The perturbed eigensolutions derived in this manner are used in obtaining the field variables (acoustic pressure, acoustic velocity etc.,) within the muffler by using a three-dimensional mode matching method. The TL for such geometries are characterized by the presence of repeating domes and resonating peaks. It is observed that the resonating peaks are due to the side-branch resonator like behavior of the annular portion of the chamber. The location of the peaks may be approximated by the quarter wavelength frequency of the side-branch resonator. The presence of the resonating peaks improves the sound attenuation characteristics of the extended muffler. However, the TL is affected by the propagation of the (2, 1) even mode, thereby limiting its ability to attenuate sound over a broad frequency range. At frequencies below the (2, 1) cutoff frequency, the extended muffler may be used to attenuate sound within a desired narrow frequency band by tuning the length of the duct extends. The present approach is restricted to moderate eccentricities and diverges for $e > 0.65$. However, useful insights derived from studying the TL at moderate eccentricities may be used in predicting the nature of the TL at higher chamber eccentricities.

Chapter 4

Study of wall compliance on the radiation and transmission

The perturbation–based approach derived in the previous chapter is implemented in order to study the sound radiation from a distorted circular cylinder with compliant surfaces. An acoustic point source located inside the shell sets the compliant surface into vibration. The vibrating surface can be imagined to be an infinite number of point sources. These sources create an external acoustic field, as well as effectively modifies the strength of the internal acoustic source. The method for solving this structure-acoustic coupled problem is based on the eigenfunction expansion of the *in–vacuo* acoustic and structural modes as suggested by Dowell *et al*. [45]. The internal acoustic field in the distorted cavity is approximated by the perturbation–based approach discussed in the previous chapter. The shell–displacements are quantified by a Rayleigh–Ritz approach [35]. Using the modal solutions, the structural vibration and the internal acoustic fields are derived. The effects of the duct distortion on the radiated sound power is discussed.

In the second part of this chapter, the sound attenuation effects of a liquid layer on at the bottom of a muffler is discussed.

4.1 Structure–acoustic coupled formulation of radiation field from a distorted shell

4.1.1 Determination of the pressure field inside the cavity

Consider a slightly distorted cylindrical cavity, terminated by rigid cylindrical baffles and surrounded by a fluid. The shell has a volume V, thickness h and length L. The cavity is subject to an excitation from a point–source of strength $Q_{vol}\delta(\vec{x}-\vec{x}')$. Assuming harmonic time dependence, the acoustic pressure inside the cavity may be derived from the inhomogeneous Helmholtz equa-

tion, and a compliant boundary condition at the shell surface S.

$$
\begin{aligned}
(\bigtriangledown^2 + k^2) P_{int}(\vec{x}) &= -j\rho_{int}\omega Q_{vol}\delta(\vec{x} - \vec{x_0}') \\
\frac{\partial P(\vec{x})}{\partial \eta} &= \begin{cases} -j\rho_{int}\omega \dot{w}(\vec{x}) & : on \;\; S \\ 0 & : on \;\; baffle \end{cases}
\end{aligned} \tag{4.1}
$$

where, P_{int} is the acoustic pressure field inside the cavity, Q_{vol} is the strength of the point excitation situated at $\vec{x_0}'$, ρ_{int} is the density of the fluid enclosed by the cavity, and $k = \omega/c_o$ is the wave number. The present formulation may be applied for any small asymmetric perturbation about the cylindrical shell. However, a moderately elliptic chamber is considered throughout the mathematical derivation. This simplification is taken partly due to the study of elliptic–chamber mufflers in the previous sections, and also due to the fact that the Rayleigh–Ritz formulation for the $in - vacuo$ shell displacements are readily available in the literature. Analogous to Eq. 2.5, the Green's function for a point source can be defined that also satisfies a rigid boundary condition. For the perturbed geometry, the Green's function is expressed in terms of the perturbed eigenvectors (Eq. 3.33). Using Green's identities, the internal pressure field may be derived as:

$$
P(\vec{x}) = \int_{V'} j\rho_{int}\omega \; Q_{vol} G(\vec{x}/\vec{x}') dV' + \int_{S'} \left(\frac{\partial P(\vec{x}')}{\partial \eta} G(\vec{x}/\vec{x}') - P(\vec{x}') \frac{\partial G(\vec{x}/\vec{x}')}{\partial \eta} \right) dS' \tag{4.2}
$$

In Eq. (4.2), the assumed form of the Green's function ensures the normal derivative of $G(\vec{x}/\vec{x}')$ on the shell is zero. The continuity of the particle velocity on the shell surface yields:

$$
\left. \frac{\partial P(\vec{x}')}{\partial \eta} \right|_{S'} = -j\rho_{int}\omega \dot{w}(\vec{x}') \tag{4.3}
$$

where, $\dot{w}(\vec{x}')$ is the normal velocity at the surface of the shell. The assumed form of the normal velocity is a weighted sum of some basis functions:

$$
\dot{w}(\vec{x}) = \sum_{m=0}^{\infty} b_m \psi_m(\vec{x}) \tag{4.4}
$$

In Eq. (4.4), an infinite sum of the basis functions should match the boundary conditions. The mathematical implementation demands that the series must be truncated to a suitable order. For circular cylinder shell, the basis functions are orthogonal and truncating the series to a sufficiently large order minimizes the error. In a distorted geometry, the basis functions may not

be orthogonal, implying that the choice of representing and truncating the displacement field is not obvious. Diperna and Stanton [38] proved that basis functions that satisfy the governing equation (here it is the shell equation) is appropriate for minimizing the error. The order of truncation is determined from a convergence study. By using Eq. (4.3) and Eq. (4.4), the pressure field inside the cavity, Eq. (4.2) is expressed as:

$$P(\vec{x}) = \sum_{n=0}^{N_A} \left(\frac{j\rho_{int}\omega c_o^2}{\omega_n^2 - \omega^2} Q_{vol} \varphi_n(\vec{x_0}') - \frac{j\rho_{int}\omega c_o^2}{\omega_n^2 - \omega^2} \int_{S'} \varphi_n(\vec{x}') \sum_{p=0}^{N_S} b_p \psi_p(\vec{x}') dS' \right) \varphi_n(\vec{x}) \tag{4.5}$$

In Eq. (4.5), the acoustic and the structural modes are truncated to order N_A and N_S, respectively. The transverse dependence of each acoustic mode is defined by Eq. (3.33) in chapter 3. Assuming that the end faces of the shell are rigid, the axial modes are of the form $\cos(p\pi z/L)$. Therefore, each acoustic mode of order n' is expressed as:

$$\begin{aligned}
&\varphi_{n'}(\vec{x}) \rightarrow \phi_{nm}(r,\theta)\cos(p\pi z/L) \\
&= \left[(A_{nm} + \varepsilon C_{nm})\, \varphi_{nm}^0(r)\cos(n\theta) + \varepsilon \sum_{s=0}^{\infty} B_s \beta_s(r)\cos(s\theta) + \varepsilon \sum_{j=1}^{\infty} D_{nm,j} \varphi_{nj}^{1p}(r)\cos(n\theta) \right] \cos(p\pi z/L) \\
&k_{r,nm} = k_{0r,nm} + \varepsilon k_{1,nm}\big|_{\psi=0} + \varepsilon^2 k_{2,nm}\big|_{\psi=0}
\end{aligned}$$

$$\begin{aligned}
&\varphi_{n'}(\vec{x}) \rightarrow \phi_{nm}(r,\theta)\cos(p\pi z/L) \\
&= \left((\bar{A}_{nm} + \varepsilon \bar{C}_{nm})\, \varphi_{nm}^0(r)\sin(n\theta) + \varepsilon \sum_{s=0}^{\infty} \bar{B}_s \beta_s(r)\sin(s\theta) + \varepsilon \sum_{j=1}^{\infty} \bar{D}_{nm,j} \varphi_{nj}^{1p}(r)\sin(n\theta) \right) \cos(p\pi z/L) \\
&k_{r,nm} = k_{0r,nm} + \varepsilon k_{1,nm}\big|_{\psi=\pi/2} + \varepsilon^2 k_{2,nm}\big|_{\psi=\pi/2}
\end{aligned} \tag{4.6}$$

In a matrix representation, Eq. (4.5) can be written as [47]

$$P_{int}(\vec{x}) = \Phi(\vec{x})^T [\mathbf{Z_a}] \left(\mathbf{q_{vol}} - \mathbf{Cb} \right) \tag{4.7}$$

where, the diagonal matrix $[\mathbf{Z_a}]_{(\mathbf{N_A} \times \mathbf{N_A})}$ is the modal acoustic impedance matrix, $\mathbf{q_{vol}}$ is the acoustic source strength vector and $\mathbf{Cb}$ is the equivalent acoustic source due the vibrating structure. The matrix $[\mathbf{C}]_{N_A \times N_S}$ represents the mode–coupling between the structure and the acoustic

duct modes:

$$\Phi(\vec{x}) = \left\{ \begin{array}{c} \varphi_1(\vec{x}) \\ \varphi_2(\vec{x}) \\ \vdots \\ \varphi_n(\vec{x}) \\ \vdots \end{array} \right\}_{N_A \times 1} ; \quad \mathbf{q_{vol}} = \left\{ \begin{array}{c} Q_{vol}\varphi_1(\vec{x_0}) \\ Q_{vol}\varphi_2(\vec{x_0}) \\ \vdots \\ Q_{vol}\varphi_n(\vec{x_0}) \\ \vdots \end{array} \right\}_{N_A \times 1} ; \quad \mathbf{b} = \left\{ \begin{array}{c} b_1 \\ b_2 \\ \vdots \\ b_p \\ \vdots \end{array} \right\}_{N_S \times 1} \tag{4.8}$$

$$\mathbf{Z_a}_{ij} = \left\{ \begin{array}{cc} \frac{j\rho_{int}\omega c_o^2}{(\omega_j^2 - \omega^2)\int_V \varphi_j^2(\vec{x})dV}; & i = j \\ 0; & i \neq j \end{array} \right. ; \quad i, j = 1, 2, 3, \cdots, N_A$$

$$\mathbf{C}_{ij} = \int_S \varphi_i(\vec{x})\psi_j(\vec{x})dS \quad i = 1, 2, 3, \cdots, N_A; \quad j = 1, 2, 3, \cdots, N_S$$

4.1.2 Structural response to the internal acoustic field

The shell equation of motion when subject to a mechanical excitation and an acoustic load can be expressed as [76]

$$[L] \left\{ \begin{array}{c} u(\vec{x},t) \\ v(\vec{x},t) \\ w(\vec{x},t) \end{array} \right\} - \left(m_s \frac{\partial^2}{\partial t^2} + j\omega\lambda \right) \left\{ \begin{array}{c} u(\vec{x},t) \\ v(\vec{x},t) \\ w(\vec{x},t) \end{array} \right\} = - \left\{ \begin{array}{c} F_u(\vec{x},t) \\ F_v(\vec{x},t) \\ F_w(\vec{x},t) \end{array} \right\} + \left\{ \begin{array}{c} 0 \\ 0 \\ P(\vec{x},t)_{ext} - P(\vec{x},t)_{int} \end{array} \right\} \tag{4.9}$$

where, $u(\vec{x},t)$, $v(\vec{x},t)$ and $w(\vec{x},t)$ are the longitudinal, tangential and radial displacement; $F_u(\vec{x},t)$, $F_v(\vec{x},t)$ and $F_w(\vec{x},t)$ are the longitudinal, tangential and radial components of the driving force. $P_w(\vec{x},t)$ are the acoustic pressure on the shell due to the excitation of the internal and the external fluid. L is the shell differential operator that depends on the shell theory considered for the modeling purpose and λ is a structural damping coefficient.

In order to solve Eq. (4.9), the normal modes and the natural frequencies of the shell need to be evaluated first. In a circular shell, for every circumferential (n) and axial (m) mode combination, there are three natural frequencies that correspond to the longitudinal, torsional and flexural vibration modes. For the elliptic shell, the loss of circular symmetry results in mode–splitting similar to that observed for the acoustic modes in chapter 3, resulting in frequency–pairs

for $n > 0$. The equations for the free vibration of an elliptic cylindrical shell of constant thickness were derived using a Ritz approach by Sewall *et al.* [35]. Using their approach, the circumferential dependence of the shell displacements was expressed as a summation of the elementary trigonometric functions, and the longitudinal dependence was chosen to satisfy the boundary conditions at the shell faces. Accordingly, the free vibration shell displacement components are expressed in the following form:

$$U_{nm}^{(i,\alpha)} = \left\{ \begin{array}{l} u_{nm}^{(i,\alpha)}(\vec{x}) \\ v_{nm}^{(i,\alpha)}(\vec{x}) \\ w_{nm}^{(i,\alpha)}(\vec{x}) \end{array} \right\} = \left\{ \begin{array}{l} \sum_{p=0} A_p^{nm,i,\alpha} \cos(p\theta - \pi\alpha/2)\gamma_{mu}(z) \\ \sum_{p=0} B_p^{nm,i,\alpha} \sin(p\theta + \pi\alpha/2)\gamma_{mv}(z) \\ \sum_{p=0} C_p^{nm,i,\alpha} \cos(p\theta - \pi\alpha/2)\gamma_{mw}(z) \end{array} \right\} \tag{4.10}$$

where, the subscripts (n) and axial (m) are the circumferential and axial modes, $i = 1, 2, 3$ are the three vibration modes for each (n, m) mode, $\alpha = 0, 1$ represents the symmetric $(\alpha = 0)$ or the anti–symmetric $(\alpha = 1)$ modes. The axial component $\gamma(z)$ for a simply–supported shell is given by:

$$\gamma_{mu}(z) = \cos(m\pi z/L); \qquad \gamma_{mv}(z) = \gamma_{mw}(z) = \sin(m\pi z/L) \tag{4.11}$$

The velocity vectors for forced vibration problem, Eq. (4.9) is expanded in terms of Eq. (4.10)

$$\dot{U}^{\alpha,i} = \frac{\partial}{\partial t} \left\{ \begin{array}{l} u(\vec{x}, t) \\ v(\vec{x}, t) \\ w(\vec{x}, t) \end{array} \right\} = \sum_n \sum_m b_{nm}^{\alpha,i} U_{nm}^{(i,\alpha)} \tag{4.12}$$

where, the harmonic dependence is implicitly applied to the coefficient $b_{nm}^{\alpha,i}$. Substituting Eq. (4.11) into Eq. (4.9), and using the solution for the free vibration [50], Eq. (4.9) is simplified to the following form:

$$\begin{aligned} &\frac{1}{j\omega} \sum_{n=0}^{N} \sum_{m=1}^{M} m_s \left(\omega_{nm}^2 - \omega^2 + 2j\zeta_s \omega_{nm}\omega\right) b_{nm}^{\alpha,i} U_{nm}^{(i,\alpha)} = \{F\}_s + \{P\}_{int} - \{P\}_{ext} \\ &\textit{where, } (N+1) \times M = N_S \text{ (for each } \alpha,\ i) \end{aligned} \tag{4.13}$$

In Eq. (4.7) and Eq. (4.12), the symmetric and the anti–symmetric modes are decoupled by appropriate orthogonalization of the circumferential terms, implying that the unknown symmetric modal coefficients are not influenced by the corresponding antisymmetric coefficients. The su-

perscript α may therefore, be omitted from the subsequent analysis. Using the same procedure as the mode matching method, the unknown coefficients b^i_{nm} are obtained from the following sets of linear–simultaneous equations:

$$\int_S \frac{1}{j\omega} \sum_{n=0}^{N} \sum_{m=1}^{M} m_s \left(\omega^2_{nm} - \omega^2 + 2j\zeta_s\omega_{nm}\omega\right) b^i_{nm} {U^{(i)}_{pq}}^T U^{(i)}_{nm} dS = \int_S {U^{(i)}_{pq}}^T \left(\{F\}_s + \{P\}_{int} - \{P\}_{ext}\right) dS$$
$$where,\ p = 0, 1, 2, \cdots, N; \qquad q = 1, 2, \cdots, M; \tag{4.14}$$

Similar to Eq. (4.7), the matrix representation of the structural modal coefficients can be expressed as:

$$\begin{aligned} &\mathbf{b} = \mathbf{Y_s F_s} + \mathbf{Y_s}\left(\mathbf{C^T Z_a}\left(\mathbf{q_{vol}} - \mathbf{Cb}\right)\right) - \mathbf{Y_s Z b} \\ &where, \\ &\mathbf{Y_s}_{pq} = \frac{j\omega}{\left(\omega^2_p - \omega^2 + 2j\zeta_s\omega_p\omega\right) m_s \int_S {U^{(i)}_{n'm'}}^T U^{(i)}_{nm} dS}; \quad p \rightarrow nm; \quad q \rightarrow n'm' \end{aligned} \tag{4.15}$$

where, $\mathbf{Y_s}$ is the modal mobility matrix and $\mathbf{Z}$ is the radiation impedance due to the external fluid. The determination of the radiation impedance term is discussed in the next section. In the above equation, the structural response may be observed to be comprised of the structural excitation, the excitation due to the equivalent internal acoustic field, and the inertia and damping offered by the external fluid.

4.1.3 Determination of the external acoustic field

The external acoustic field P_{ext} due to the acceleration distribution of the distorted cylinder is obtained form the solution of the Helmholtz equation applicable to an appropriate coordinate system. In this formulation, since the geometric distortions are small, it is expected that the far–field pressure distribution due to the distorted cylinder will be similar to that obtained from an equivalent circular cyinder. Therefore, the pressure field due to the distorted cylinder may be considered as a weighted sum of all the possible solutions due to a circular cylinder. The contribution (weights) due to each mode will be governed by the acceleration distribution $(\ddot{w})$. When a Fourier transform in z is applied to the Helmholtz equation in the cylindrical coordinates, the pressure transform is obtained as [51]:

$$\tilde{P}_{ext}(r, \theta; k_z) = \sum_q B_q H^{(2)}_q(k_r r) \cos(q\theta) \tag{4.16}$$

where, $k_r = \sqrt{k^2 - k_z^2}$, and $H_q^{(2)}$ is the Hankel function of the second kind. The assumed harmonic form of the present formulation is $\exp(j\omega t - k_r r)$. Using this convention, the Hankel function of the second kind may be shown to be the appropriate form of the solution in order to capture the propagation of an outward traveling plane wave at large distances from the cylinder. When k_r is imaginary, the negative complex root should be considered for finite solution. Similar to the pressure transform, the Fourier transform of the surface normal displacement yields:

$$\tilde{w}_{nm}(\theta; k_z) = \frac{1}{j\omega} \sum_n \sum_m \left(\sum_p C_p^{nm} \cos(p\theta) \Gamma_m(k_z) \right) b^{nm} \tag{4.17}$$

The coefficients B_q is obtained from the velocity boundary conditions. The normal component of the pressure at the surface of the elliptic shell is given by Eq. 3.4. However, when the external fluid is light the effect of the fluid loading on the structure is expected to be small, implying that the $O(\varepsilon)$ term may be neglected from Eq. 3.4. Using this assumption, the coefficients B_q is derived as:

$$B_q = -j\rho_{ext}\omega \sum_n \sum_m \left[C_q^{nm} \frac{\Gamma_m(k_z)}{k_r H_q^{'(2)}(k_r a)} \right] b^{nm} \tag{4.18}$$

Substituting Eq. 4.18 into Eq. 4.16 and taking the inverse Fourier transform, the external pressure field is expressed as:

$$P_{ext}(r, \theta, z) = -\frac{j\rho_{ext}\omega}{2\pi} \sum_i \sum_j \left[\sum_q C_q^{ij} \int_{-\infty}^{\infty} \frac{\Gamma_j(k_z) H_q^{(2)}(k_r r)}{k_r H_q^{'(2)}(k_r a)} \exp(-jk_z z) dk_z \cos(q\theta) \right] b^{ij} \tag{4.19}$$

The external pressure field is substituted into Eq. (4.14) and the inner product with the shell velocity is taken. In matrix notation, this can be written as:

$$\int_S {U_{nm}}^T \{P\}_{ext} \, dS = \langle P_{ext}(r, \theta, z), U_{nm} \rangle = \begin{bmatrix} \langle P_{11}, U_{nm} \rangle & \langle P_{12}, U_{nm} \rangle & \cdots \end{bmatrix}_{1 \times N_S} \begin{Bmatrix} b_{11} \\ \vdots \\ b_{ij} \\ \vdots \end{Bmatrix}_{N_S \times 1}$$

$$\textit{where}, \langle P_{ij}, U_{nm} \rangle = \mathbf{Z}_{ij,nm}$$

$$= -\frac{j\rho_{ext}\omega}{2\pi} \left[\sum_q \sum_s C_q^{ij} C_s^{nm} \int_{-\infty}^{\infty} \frac{\Gamma_j(k_z) \Gamma_m^*(k_z) H_q^{(2)}(k_r r)}{k_r H_q^{'(2)}(k_r a)} dk_z \int_0^{2\pi} \cos(q\theta) \cos(s\theta) r(\theta) d\theta \right] \tag{4.20}$$

The above equation is the acoustic radiation impedance on the shell due to the external fluid loading. The radiation impedance for a cylindrical shell was derived by Stephanishen [50]. In the limit of a cylindrical shell the summation over q and s in Eq. (4.20) reduces to a single term due to the orthogonality of the cosine function, and exactly matches with the form derived in the literature [50, 53]. This orthogonality condition also implies that although the modal coefficients b of different longitudinal wavenumber (j and m) are coupled, coupling of modal coefficients with different circumferential wavenumber is not possible. However for a perturbed cylinder, the dependence of the radius of curvature r on the circumferential perturbation allows for coupling of different circumferential orders as well. The power radiated by the shell is obtained as:

$$P_{rad} = \frac{1}{2}\mathrm{Re}\sum_{\alpha}\sum_{i}\left(\mathbf{b}^{*\mathrm{T}}\mathbf{Z}\mathbf{b}\right)^{(\alpha,i)} \tag{4.21}$$

4.2 Numerical verification: Radiation from simply–supported cylindrical shell

The present formulation was verified with existing work by Laulagnet and Guyader [53]. Forced–structural excitation of a simply–supported circular cylindrical shell was considered in their work. A steel shell of 1.2 m length (L), 0.4 m radius, and 3 mm thickness was excited at a location of $2L/5$ from one of the end faces. The structural damping coefficient was 0.01. In order to realize the same conditions in the present formulation, the internal acoustic source and coupling terms ($\mathbf{q_{vol}}$ and $\mathbf{C}$), and the eccentricity e, were zero. The radiated power from the shell is presented in Fig. 4.1. It may be observed that the present numerical implementation matches well with the prior work, except for the shift in the peaks. This shift may be attributed to the differences material properties that were not mentioned in [53].

4.3 Numerical implementation: Radiation from an elliptic shell

The problem of interest is an elliptic steel shell of length $L = 1.2\ m$. The eccentricity of the shell is $e = 0.6$. The major and the minor axis of the shell is such that the area of cross section corresponds to that of a circle of radius 0.2 m. The shell is excited by an acoustic point source located at the geometric center of one of the end faces. The ends of the shell are assumed to be simply supported and are terminated in infinitely long baffles. The shell is assumed to be

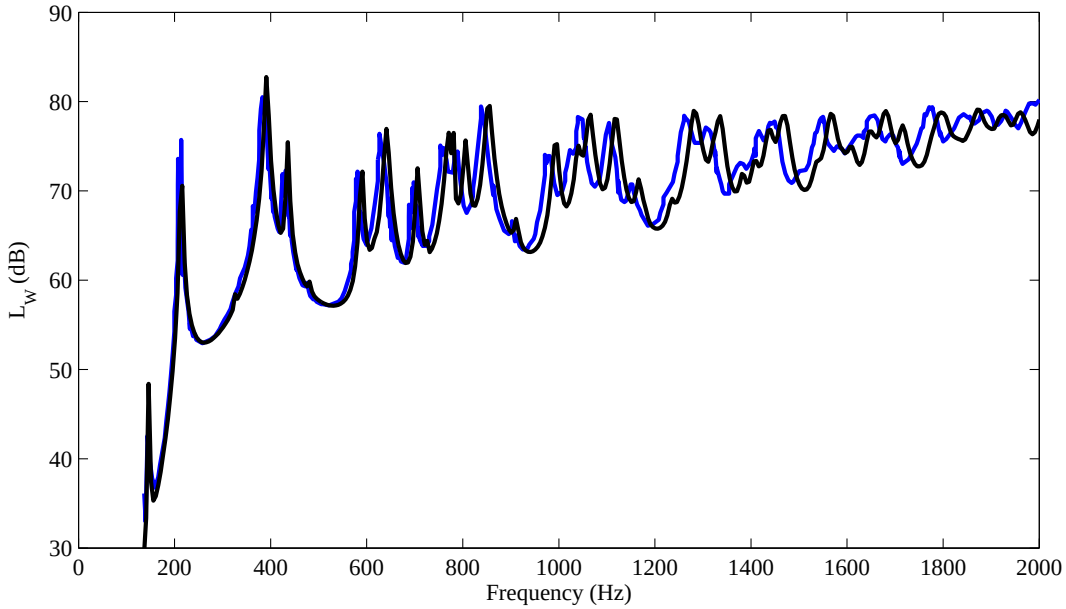

Figure 4.1: Validation of the perturbation–based sound radiation model when eccentricity, $e \rightarrow 0$; ———, present formulation; ———, Laulagnet and Guyader[53]

surrounded by air. The following material parameters are employed in the present formulation:

$$\rho_{air} = 1.21\ kg/m^3 \quad \rho_{str} = 7850\ kg/m^3 \quad c_{air} = 343\ m/s$$
$$h = 1.5\ mm \qquad E = 210\ GPa \qquad \mu = 0.3 \qquad \zeta = 0.01$$

In Fig. 4.2, the radiated sound power level for the elliptic cylinder is compared to an equivalent circular cylinder of same area of cross–section. From the figure, it can be observed that the radiated sound power from the elliptic cylinder is approximately 10-15 dB higher than the corresponding circular cylinder. At low frequencies the two curves overlap, which is expected because higher order acoustic or structural modes are not excited at these frequencies. At a frequency of about 150 Hz, the $(2,1)$ structural mode in the elliptic duct is excited by the plane acoustic wave, resulting in much higher sound radiation when compared to the cylindrical shell. The excitation of the higher order structural mode by a plane wave is termed as mode–coupling and has been discussed by Yousri and Fahy [58] (see Eq. 7 in [58]). A qualitative understanding of the mode–coupling effect may be realized by considering Eq. (4.8) and Eq. (4.10). In Eq. (4.10), the (2, 1) structural mode for the distorted shell has a breathing mode contribution implying that the coefficient $C_0^{n=2,m,i,\ sym}$ is non–zero. For an elliptic shell, the radius of curvature may be approximated as $r \approx R + \varepsilon\cos(2\theta)$. Therefore, the coupling matrix defined by Eq. (4.10) will

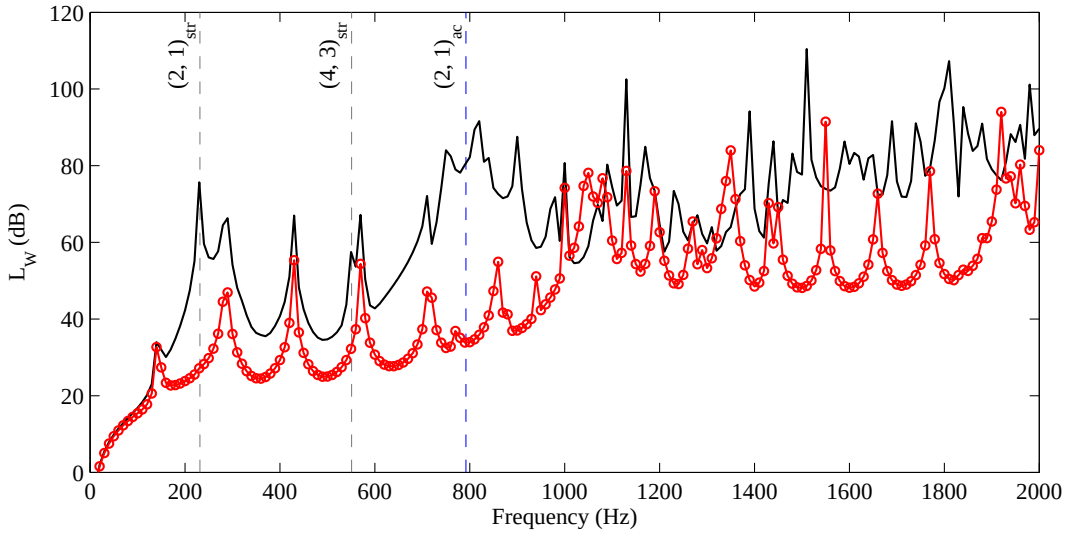

Figure 4.2: ———, Sound power level from an elliptic shell with simply–supported boundary conditions, $e = 0.6$, $L = 1.2\ m$; –o–o–o–, cylindrical shell of same area of cross-section ($r = 0.2\ m$) as the elliptic shell

have a non–zero component when the surface intergral is performed over the (2, 1) structural mode and the plane– wave acoustic mode. This non–zero component acts on the generalized force term $\mathbf{q_{vol}}$ through Eq. (4.15), yielding a non–zero value for $\mathbf{b}_{(\mathbf{2,1})}$. The (2, 1) structural mode has a peak displacement near its resonating frequency $(\approx 231Hz)$, which lead to a peak in the radiated power response as seen in Fig. 4.2.

In order to further validate the mode–coupling effects, a hypothetical situation is considered whereby the shell is treated as a circular cylinder, while the elliptic boundary is considered for the internal acoustic field. The sound power level for such problem is presented in Fig. 4.3. In this new configuration, the plane acoustic wave no longer excites the (2, 1) or the (4, 3) structural modes, yielding a radiation power level similar to the equivalent cylindrical–shell.

The ellipticity of the shell allows for the propagation of the higher order (2, 1) acoustic mode as demonstrated in chapter 3. The propagation of this mode strongly affects the sound radiation inasmuch as a difference in 30–35 dB is observed in Fig. 4.1. The excitation of the higher order acoustic modes increases the strength of the generalized source term, and also causes higher–order mode coupling effects, thereby resulting in increased sound power levels in comparison to the cylindrical shell. The effect of the propagating (2, 1) acoustic mode is verified from Fig. 4.4. In this figure, the shell is considered as an ellipse; the internal acoustic field is due to a point source inside an equivalent circular cylinder. The circular cylinder approximation for the acoustic field

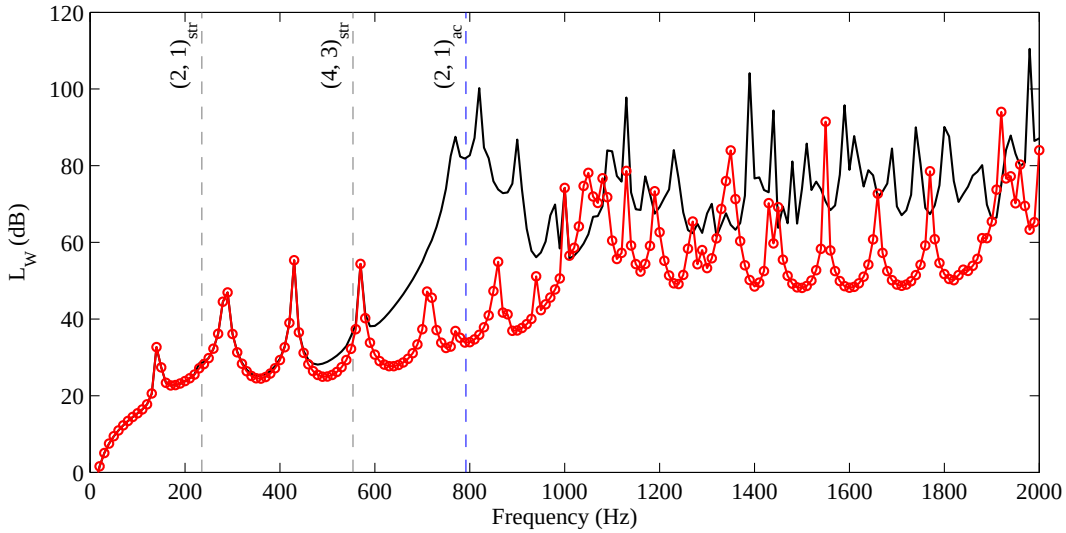

Figure 4.3: Sound power level from an elliptic shell with simply–supported boundary conditions:———, equivalent cylindrical shell is considered for the structure, $e = 0.6$, $L = 1.2\ m$; –o–o–o–, cylindrical shell of same area of cross-section ($r = 0.2\ m$) as the elliptic shell

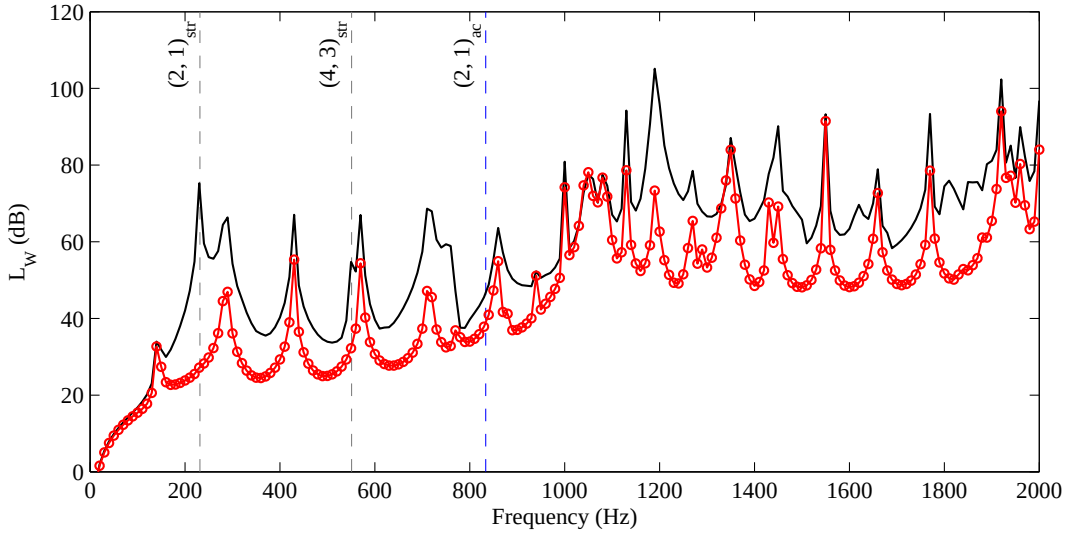

Figure 4.4: Sound power level from an elliptic shell with simply–supported boundary conditions:———, equivalent cylindrical is considered for the internal acoustic field, $e = 0.6$, $L = 1.2\ m$; –o–o–o–, cylindrical shell of same area of cross-section ($r = 0.2\ m$) as the elliptic shell

prevents the propagation of the (2, 1) mode, resulting in lower sound radiation. Figure 4.4 also provides the relative influence of the shell distortion on the radiated sound due to a plane wave excitation only. At frequencies below 800 Hz, it may be observed that the ellipticity of the shell results in approximately 15–20 dB difference in the radiated sound power level when compared to the equivalent cylindrical shell.

4.4 Effects of a liquid layer on the TL in a duct

The final section of this dissertation is focused on studying the effects of a liquid on the overall sound attenuation in a duct. The presence of a liquid phase is a muffler or a duct may be a common occurrence due to accumulation of condensate, or due to the presence of a lubricating oil. The present objective is to understand the effects of the liquid phase on the sound attenuation. Unlike previous studies, a rectangular duct is considered for the present analysis. The limitation of the analytical solution to rectangular domain is due to the fact that for circular or elliptical ducts the method of separation of variable may not be applied when there is a discontinuity along a non–constant basis.

4.4.1 Mathematical modeling

Consider a rigid square cavity of length L and edge a as shown in Fig. 4.5. The cavity is comprised of an air–water system. The height of the water layer is h. For a square cavity, the solution to the Helmholtz equation for each phase i is expressed as:

$$
\begin{aligned}
P_{air}(x,y,z) &= \sum_{n=0}^{\infty}\sum_{m=1}^{\infty}\left(A^{+}_{air,\,nm}\exp(-jk_{nm,\,z}z) + A^{-}_{air,\,nm}\exp(jk_{nm,\,z}z)\right)\cos(n\pi x/a)\cos(k^{air}_{nm,\,y}(a-y)) \\
P_{liq}(x,y,z) &= \sum_{n=0}^{\infty}\sum_{m=1}^{\infty}\left(A^{+}_{liq,\,nm}\exp(-jk_{nm,\,z}z) + A^{-}_{liq,\,nm}\exp(jk_{nm,\,z}z)\right)\cos(n\pi x/a)\cos(k^{liq}_{nm,\,y}y)
\end{aligned}
\tag{4.22}
$$

The above form of the solutions ensures that the rigid boundary conditions are satisfied. The axial wavenumber $k_{nm,\,z}$ is expressed in terms of the transverse wavenumbers as:

$$
k^2_{nm,\,z} = k^2_{air} - (n\pi/L)^2 - (k^{air}_{nm,\,y})^2 = k^2_{liq} - (n\pi/L)^2 - (k^{liq}_{nm,\,y})^2 \tag{4.23}
$$

where, $k_{air} = (\omega/c_{air})$ and $k_{liq} = (\omega/c_{liq})$. It is assumed that the acoustic pressure and the velocity are the same at the interface $y = h$, which yields the following dispersion relation:

$$
k^{air}_{nm,\,y}\tan\left(k^{air}_{nm,\,y}(a-h)\right) + \frac{\rho_{air}}{\rho_{liq}}k^{liq}_{nm,\,y}\tan\left(k^{liq}_{nm,\,y}h\right) = 0 \tag{4.24}
$$

As $\rho_{air}/\rho_{liq} << 1$, the second term in Eq. (4.24) can be neglected as a first approximation. Therefore the transverse wavenumber in the y direction is given by:

$$\begin{aligned} &\tan\left(k^{air}_{nm,\,y}(a-h)\right) = 0 \\ &or,\ k^{air}_{nm,\,y} = m\pi/(a-h); \quad m = 0, 1, 2, \cdots \end{aligned} \tag{4.25}$$

The above equation is the characteristic equation for a rigid chamber of height $(a-h)$, implying that the liquid layer effectively acts as a rigid surface and has no influence on the sound attenuation. A better approximation of the effects of the liquid layer is obtained by taking a higher order approximation. Since the effects of the second term in Eq. (4.24) is small, the higher–order approximation to the wavenumber may be expressed as:

$$k^{air}_{nm,\,y} \approx m\pi/(a-h) + \varepsilon k; \quad m = 0, 1, 2, \cdots \tag{4.26}$$

where, εk is a small approximation to the leading order term. By substituting Eq. (4.26) into Eq. (4.24) and by expanding the *tan* functions for small arguments, εk is expressed as:

$$\begin{aligned} \varepsilon k &\approx \sqrt{\frac{\rho_{air} k_{air} \tanh(k_{air} h)}{\rho_{liq}(a-h)}}; \qquad m = 0; \\ \varepsilon k &\approx \frac{\rho_{air} k_{air} \tanh(k_{air} h)}{\rho_{liq} m\pi}; \qquad m \neq 0; \end{aligned} \tag{4.27}$$

From the above equation, and from Eq. (4.23), it is evident that even the fundamental acoustic mode is dispersive resulting a non–uniform pressure field along the y axis. Since the differences in density of the liquid and the gas phase are large, the deviation from the non–dispersive effects may be considered as negligible.

4.4.2 Determination of TL and experimental validation

The mode matching method was employed for a square duct with edge $a = 0.108\ m$, length $L = 0.292\ m$ as shown in Fig. 4.5. The inlet and outlet ports were located at the center of the end-faces. For numerical simplicity, the ports were taken to be square sections with edge $a_1 = 0.023\ m$. In order to validate the numerical results, a test muffler was made from acrylic. In the test muffler, the inlet and outlet ports were circular, with same area of cross–section as

the square ports. In the numerical model, two approaches were followed. In the first approach, the MMM was employed over the entire muffler domain (air and the water) using the dispersion relation from Eq. (4.24). In the second approach, the liquid layer was considered as rigid, thereby changing the aspect ratio of the geometry as shown in Fig. 4.5(b). In both of the approaches, the TL was observed to the same and were not affected by the liquid layer (except for the change in the effective size of the muffler).

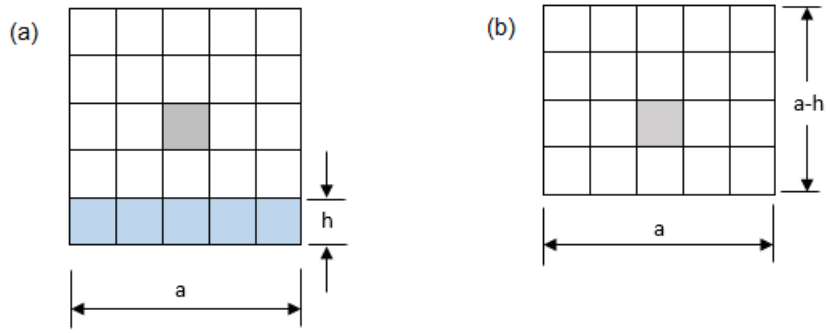

Figure 4.5: Schematic of the cross–section of a square duct of edge a. (a) The duct is filled with water upto a height of h; (b) Equivalent duct cross–section when the liquid layer is treated as a rigid layer

The above observation was further verified through experiments based on the ASTM E2611-09 standard method for measuring the TL [77]. A schematic of the experimental apparatus as shown in Fig. 4.6 consisted of an impedance tube configuration, where the muffler was subjected to a broad–frequency noise from a source. A weakly anechoic termination was imposed at the other end of the tube. The measured reflection coefficient due to this termination is shown in Fig. 4.7. Two microphones were placed at the upstream and at the downstream locations in order to decompose the incident and the reflected waves. The transfer function between the microphones was utilized in order to determine the TL. In Figs. 4.8–4.10, the comparison between the numerical and the experimental results are presented for different heights of the water layer. The numerical results are based on the GFM applied to the equivalent geometry (Fig. 4.5(b)). The experimental results agree with the numerical results, validating the observation that the dispersive nature of the fundamental acoustic mode does not affect the TL, and that the liquid layer only modifies the geometry.

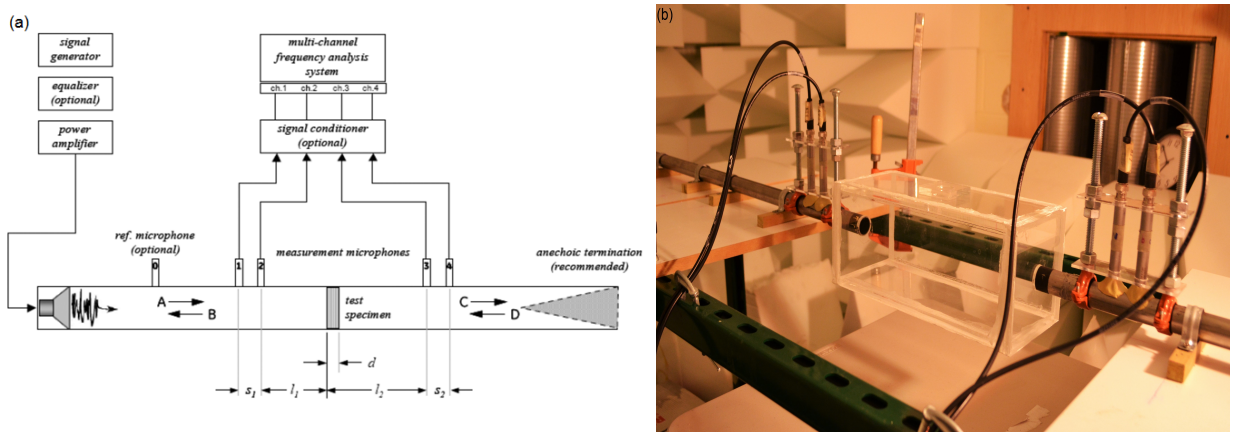

Figure 4.6: Schematic diagram of the experimental apparatus for measuring the TL

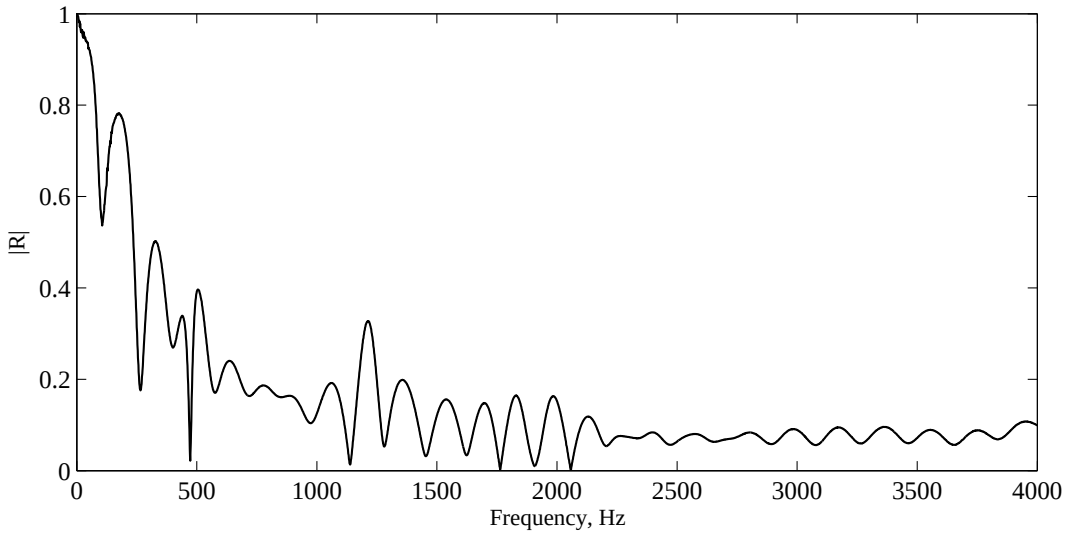

Figure 4.7: Measured reflection coefficient at a downstream location in the test apparatus

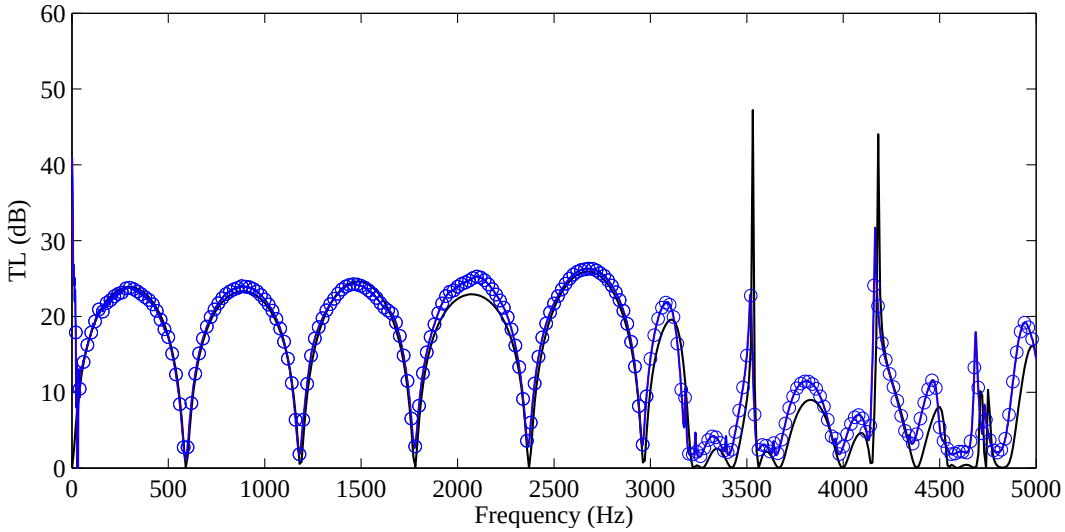

Figure 4.8: Transmission loss in a square muffler of edge $a = 0.108\ m$, length, $L = 0.292\ m$. The height of water level, $h = 0\ m$. ———, Analytical model based on the equivalent geometry in Fig. 4.5(b); –o–o–o–, Experimental results

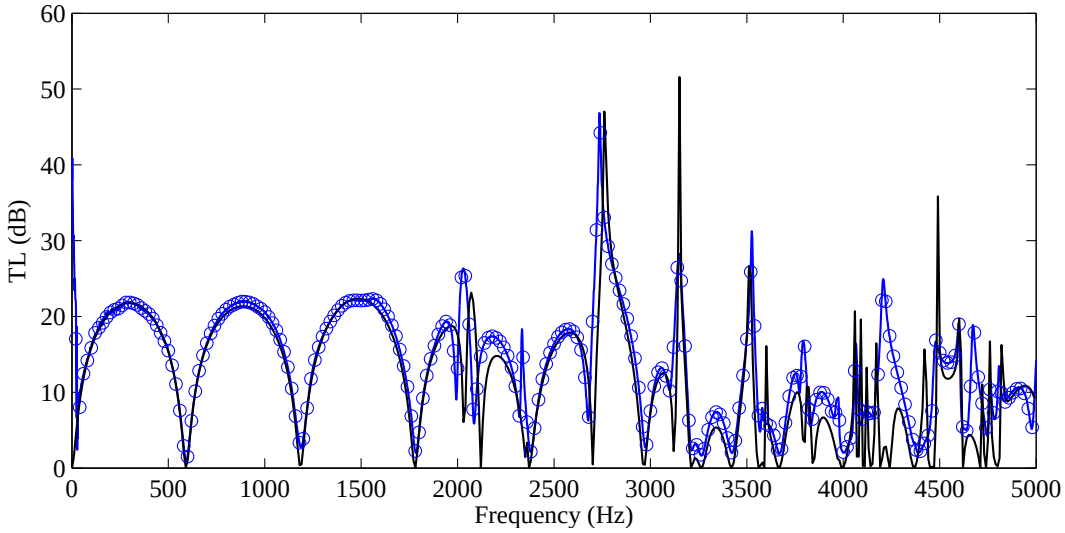

Figure 4.9: Transmission loss in a square muffler of edge $a = 0.108\ m$, length, $L = 0.292\ m$. The height of water level, $h = 0.023\ m$. ———, Analytical model based on the equivalent geometry in Fig. 4.5(b); –o–o–o–, Experimental results

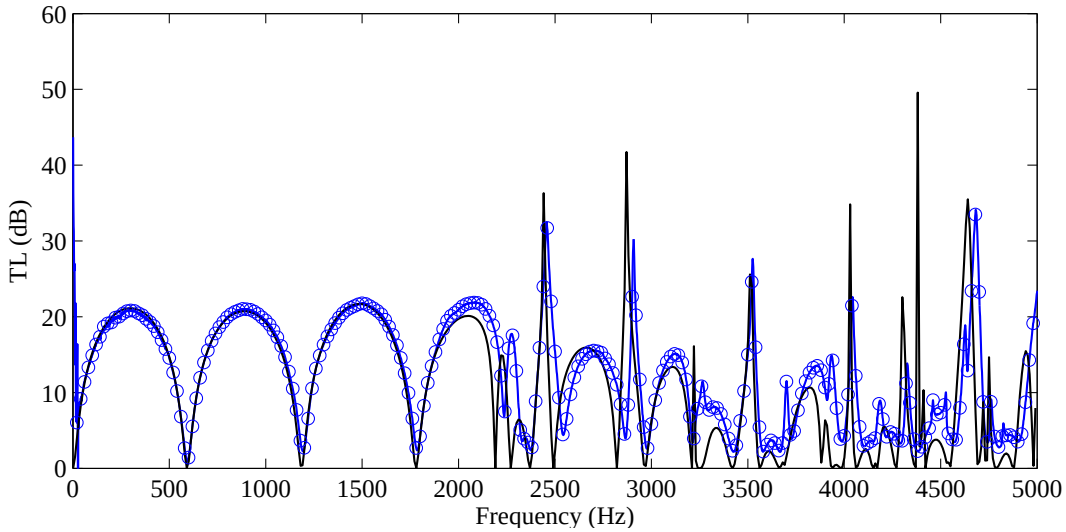

Figure 4.10: Transmission loss in a square muffler of edge $a = 0.108\ m$, length, $L = 0.292\ m$. The height of water level, $h = 0.029\ m$. ———, Analytical model based on the equivalent geometry in Fig. 4.5(b); –o–o–o–, Experimental results

4.5 Summary

The sound radiation from an elliptic duct of eccentricity $e = 0.6$, when excited by an internal acoustic field was studied. Using the perturbation based method, the internal acoustic field was determined for a simply–supported elliptic shell. The shell displacements were governed by the shell equations applied to an elliptic geometry. The external loading due to the ambient fluid was also considered in the present formulation. The shell displacements were coupled with the internal acoustic field. By solving for these two coupled equations, the external radiation from the shell was quantified. The sound radiation from the elliptical shell was influenced by two primary factors. At frequencies lower than the cutoff frequency of the first higher–order propagating acoustic mode, the plane acoustic wave was observed to excite the shell higher–order mode. The excitation of these modes increased the radiated power by 10–15 dB. Near the cutoff frequency of the (2, 1) acoustic mode, the structural radiation was observed to be about 30–35 dB higher than that of a cylindrical shell of comparable dimensions. This observation leads to the conclusion that the effects of higher–order propagating acoustic modes are more dominant in sound radiation from such shells.

The second part of the chapter was focused on studying the effects of a liquid layer on the TL in a muffler. A dispersion equation for the transverse wave number suggested that although the fundamental mode was dispersive, the effects of the liquid layer is weak and may not affect the

TL. It was observed from the dispersion relation that the liquid layer essentially performed like a solid boundary. transmission loss analysis based on a numerical approach further strengthened the idea that indeed the liquid layer altered the size of the muffler, and had no other effects. An experimental setup based on the ASTM standard method for measuring TL was developed to verify the numerical model. Close agreement between the experimental and numerical solutions proved that the presence of the liquid layer may be accounted by only altering the size of the muffler.

Chapter 5

Conclusions

The present work explored an analytical treatment of the sound transmission and radiation from ducts that are slightly distorted from the cylindrical geometry. Such distortions are commonly observed in different noise attenuation as well as noise generation devices such as mufflers and flow–ducts.

The first part of this work focused on the study of sound attenuation in muffler geometries, especially mufflers having circular or elliptical cross–sections. The sound attenuation characteristics of a muffler is dependent on various factors like shape and size of the muffler, orientations of inlet/ outlet ports, and number of inlet/outlet ports. In order to understand the effects of these parameters on the transmission loss (TL), a general procedure based on three dimensional Green's function was developed. The Green's function method (GFM) utilized the properties of the Green's identities by treating the inlet and the outlet ports as uniformly vibrating pistons. The assumption of uniformly vibrating piston sources implied that higher–order modes were suppressed at the inlet and at the outlet. The GFM was observed to be a simplification of the Mode Matching Method (MMM). By forcibly setting the higher–order contributions at the inlet/outlet, the MMM was observed to yield exactly the same TL characteristics as the GFM. The error due to the simplification was observed to be extremely small for long–chamber mufflers. For short mufflers, the differences in the TL was observed as a shift in the resonating peaks. While the GFM was suitable for most muffler geometries where the method of separation of variables are applicable, presence of discontinuity inside the muffler such as duct extensions could not be analyzed using the GFM. On the other hand, the MMM could not be employed for mufflers having side outlets.

Using the GFM, TL for multiple inlets/outlets configuration was validated through existing TL results in the literature. The method was found to be flexible as both the SIDO (single–inlet/ double–outlet) and the DISO (double–inlet/ single–outlet) configurations could be studied by

making small changes to the mathematical formulations. Parametric studies were performed to understand the effect of various inlet and outlet configurations on the TL. Deriving knowledge from single inlet/outlet mufflers, broadband attenuation characteristics were observed by proper orientation of inlets/outlets in the SIDO and DISO mufflers. Minor loss in TL was observed for the SIDO muffler when compared to an equivalent single outlet muffler. For the DISO muffler, depending upon the phase difference between the incoming waves, and the orientation of the ports, yielded in a TL curve that exactly matched the TL curve for the corresponding SIDO muffler. This similarity was a consequence of the principle of reciprocity. It was also observed that a pressure release surface could be achieved for certain DISO muffler configurations. Thus, complete attenuation of sound was possible in a DISO muffler. In the elliptic chamber muffler, unlike the cylindrical chamber the (2, 1) even mode was observed to be a non-evanescent mode for most muffler geometries. The propagation of this mode beyond the cutoff frequency resulted in poor TL at higher frequencies. In this respect, the elliptic chamber mufflers may be considered as inferior to cylindrical chamber mufflers.

It can be inferred from the study of elliptic mufflers, that the loss of circular symmetry results in the propagation of certain higher–order modes that are essentially suppressed for the cylindrical configuration. The shape of these eigenmodes depends on the nature of the boundary asymmetry. Motivated by the need to quantify the effects of boundary asymmetry on the overall sound attenuation, a perturbation–based approach was implemented for studying the TL is slightly distorted cylindrical muffler geometries. The perturbation approach was validated for an elliptic muffler of eccentricity $e = 0.4 \sim 0.6$. Within the moderate eccentricity limits, the perturbation method compared well with the exact solutions. Improved sound attenuation was observed for the elliptical muffler by suitably locating the inlet/outlet ports such that their center coincided with the nodal diameters of the (2, 1) and the (0, 2) modes. The perturbation method was them employed for studying the TL in an extended chamber elliptic muffler. The presence of resonating peaks in addition to the dome like behavior in the TL was quantified through this work. The analytical treatment of elliptic geometries with duct extensions have not been reported in the past, primarily because of the fact that the method of separation of variables may not be applied for non–confocal geometries. The perturbation based approach was validated with FEM results in ANSYS and were observed to be in good agreement.

In the second part of the dissertation, the sound radiation from distorted ducts when excited

by an internal acoustic field was studied. Using the perturbation based method, the internal acoustic field was determined for a simply–supported elliptic shell. The compliant shell–surface was shown to act like acoustic sources and modified the internal acoustic field. The strength of this source depended on the shell displacement. The shell displacement was governed by the shell equations applied to an elliptic geometry. A Rayleigh–Ritz approach implemented by Sewall *et al.* [35] was employed for determining the shell displacements. The external loading due to the ambient fluid was also considered in the present formulation. The shell displacements were coupled with the internal acoustic field. By solving for these two coupled equations, the external radiation from the shell was quantified. Mode–coupling, whereby higher–order shell modes were vibrated due to plane–wave acoustic field was observed to increase the shell radiation by approximately 10-15 dB. Moreover, the propagation of higher–order acoustic modes above their cutoff–frequency was observed to increase the sound radiation by as much as 30-35 dB.

The final part of the dissertation was focused on studying the effects of a liquid layer on the TL in a muffler. The presence of a liquid layer in a muffler is a common occurrence, for e.g. an oil layer in a compressor, or in an exhaust system. The presence of this layer of liquid may be considered as a compliant surface, potentially altering the sound transmission. A dispersion equation for the wave number suggested otherwise. It was observed from the dispersion relation that the liquid layer essentially performed like a solid boundary. transmission loss analysis based on a numerical approach further strengthened the idea that indeed the liquid layer altered the size of the muffler, and had no other effects. An experimental setup based on the ASTM standard method for measuring TL was developed to verify the numerical model. Close agreement between the experimental and numerical solutions prove that the presence of the liquid layer may be accounted by only altering the size of the muffler.

Bibliography

[1] D. D. Davis Jr., M. Stokes, D. Moore, L. Stevens, Theoretical and experimental investigation of mufflers with comments on engine exhaust muffler design, NACA Report TN 1192 (1954).

[2] J. Igarashi, M. Toyama, Fundamentals of acoustic silencers: (I) theory and experiment of acoustic low-pass filters, Aeronautical Research Institute, University of Tokyo, Report 339 (1958) 223 – 241.

[3] M. L. Munjal, Acoustics of ducts and mufflers, Wiley-Interscience, New York, 1987.

[4] M. L. Munjal, Velocity ratio-cum-transfer matrix method for the evaluation of a muffler with mean flow, Journal of Sound and Vibration 39 (1) (1975) 105 – 119.

[5] M. L. Munjal, Plane wave analysis of side inlet/outlet chamber mufflers with mean flow, Applied Acoustics 52 (2) (1997) 165 – 175.

[6] F. C. Karal, The analogous acoustical impedance for discontinuities and constrictions of circular cross section, The Journal of the Acoustical Society of America 25 (2) (1953) 327 – 334.

[7] A. J. Torregrosa, A. Broatch, R. Payri, F. Gonzalez, Numerical estimation of end corrections in extended-duct and perforated-duct mufflers, Journal of Vibration and Acoustics 121 (1999) 302 – 308.

[8] Z. L. Ji, Acoustic length correction of closed cylindrical side-branched tube, Journal of Sound and Vibration 283 (3 - 5) (2005) 1180 – 1186.

[9] Z. Kang, Z. Ji, Acoustic length correction of duct extension into a cylindrical chamber, Journal of Sound and Vibration 310 (4-5) (2008) 782 – 791.

[10] P. Chaitanya, M. Munjal, Effect of wall thickness on the end corrections of the extended inlet and outlet of a double-tuned expansion chamber, Applied Acoustics 72 (1) (2011) 65 – 70.

[11] L. J. Eriksson, Higher order mode effects in circular ducts and expansion chambers, The Journal of the Acoustical Society of America 68 (2) (1980) 545 – 550.

[12] J. Kim, W. Soedel, General formulation of four pole parameters for three-dimensional cavities utilizing modal expansion, with special attention to the annular cylinder, Journal of Sound and Vibration 129 (2) (1989) 237 – 254.

[13] J. Kim, W. Soedel, Development of a general procedure to formulate four pole parameters by modal expansion and its application to three-dimensional cavities, Journal of Vibration and Acoustics 112 (1990) 452 – 459.

[14] J. G. Ih, B. H. Lee, Analysis of higher order mode effects in the circular expansion chamber with mean flow, The Journal of the Acoustical Society of America 77 (4) (1985) 1377 – 1388.

[15] S. I. Yi, B. H. Lee, Three dimensional acoustic analysis of circular expansion chambers with a side inlet and a side outlet, The Journal of the Acoustical Society of America 79 (5) (1986) 1299 – 1306.

[16] S. I. Yi, B. H. Lee, Three dimensional acoustic analysis of a circular expansion chamber with side inlet and end outlet, The Journal of the Acoustical Society of America 81 (5) (1987) 1279 – 1287.

[17] Y. H. Kim, S. W. Kang, Green's solution of the acoustic wave equation for a circular expansion chamber with arbitrary locations of inlet, outlet port, and termination impedance, The Journal of the Acoustical Society of America 94 (1) (1993) 473 – 490.

[18] B. Venkatesham, M. Tiwari, M. L. Munjal, Transmission loss analysis of rectangular expansion chamber muffler with arbitrary location of inlet/outlet by means of Green's function, Journal of Sound and Vibration 323 (2009) 1032 – 1044.

[19] A. I. El Sharkawy, A. H. Nayfeh, Effect of an expansion chamber on the propagation of sound in circular ducts, The Journal of the Acoustical Society of America 63 (3) (1978) 667 – 674.

[20] F. D. Denia, A. Selamet, F. J. Fuenmayor, R. Kirby, Acoustic attenuation performance of perforated dissipative mufflers with empty inlet/outlet extensions, Journal of Sound and Vibration 302 (4 - 5) (2007) 1000 – 1017.

[21] G. Yu, L. Cheng, D. Li, A three-dimensional model for T - shaped acoustic resonators with sound absorption materials, The Journal of the Acoustical Society of America 129 (5) (2011) 3000–3010.

[22] J. Miles, The reflection of sound due to a change in cross section of a circular tube, The Journal of the Acoustical Society of America 16 (1) (1944) 14 – 19.

[23] A. Selamet, Z. Ji, Acoustic attenuation performance of circular expansion chambers with offset inlet/outlet: I Analytical approach, Journal of Sound and Vibration 213 (4) (1998) 601 – 617.

[24] A. Selamet, Z. Ji, Acoustic attenuation performance of circular expansion chambers with extended inlet/outlet, Journal of Sound and Vibration 223 (2) (1999) 197 – 212.

[25] A. Selamet, M. B. Xu, I.-J. Lee, N. T. Huff, Analytical approach for sound attenuation in perforated dissipative silencers, The Journal of the Acoustical Society of America 115 (5) (2004) 2091 – 2099.

[26] A. Selamet, M. B. Xu, I.-J. Lee, N. T. Huff, Helmholtz resonator lined with absorbing material, The Journal of the Acoustical Society of America 117 (2) (2005) 725 – 733.

[27] C. J. Wu, X. J. Wang, H. B. Tang, Transmission loss prediction on {SIDO} and {DISO} expansion-chamber mufflers with rectangular section by using the collocation approach, International Journal of Mechanical Sciences 49 (7) (2007) 872 – 877.

[28] C. J. Wu, X. J. Wang, H. B. Tang, Transmission loss prediction on a single-inlet/double-outlet cylindrical expansion-chamber muffler by using the modal meshing approach, Applied Acoustics 69 (2) (2008) 173 – 178.

[29] M. V. Lowson, S. Baskaran, Propagation of sound in elliptic ducts, Journal of Sound Vibration 38 (1975) 185 – 194.

[30] K. Hong, J. Kim, Natural mode analysis of hollow and annular elliptical cylindrical cavities, Journal of Sound and Vibration 183 (2) (1995) 327 – 351.

[31] F. D. Denia, J. Albelda, F. J. Fuenmayor, Acoustic behavior of elliptical chamber mufflers, Journal of Sound and Vibration 241 (3) (2001) 401 – 421.

[32] A. Selamet, F. D. Denia, Acoustic behaviour of short elliptical chambers with end-central inlet and end offset or side outlet, Journal of Sound and Vibration 245 (5) (2001) 953 – 959.

[33] S. Banerjee, A. M. Jacobi, Analysis of sound attenuation in elliptical chamber mufflers by using Green's function, in: Proceedings of the ASME 2011 International Mechanical Engineering Congress & Expositions, Denver, USA, 2011.

[34] A. Mimani, M. L. Munjal, 3-D acoustic analysis of elliptical chamber mufflers having an end-inlet and a side-outlet: An impedance matrix approach, Wave Motion 49 (2) (2012) 271 – 295.

[35] J. L. Sewall, W. M. Thompson Jr, C. Pusey, An experimental and analytical vibration study of elliptical cylindrical shells, Applied Acoustics 52 (1997) 165 – 175.

[36] A. Nayfeh, D. Mook, D. Lobitz, S. Sridhar, Vibrations of nearly annular and circular plates, Journal of Sound and Vibration 47 (1) (1976) 75 – 84.

[37] S. B. Roberts, The eigenvalue problem for two dimensional regions with irregular boundaries, Journal of Applied Mechanics 34 (3) (1967) 618 – 622.

[38] D. T. DiPerna, T. K. Stanton, Sound scattering by cylinders of noncircular cross section: A conformal mapping approach, The Journal of the Acoustical Society of America 96 (5) (1994) 3064 – 3079.

[39] R. Parker, C. Mote, Jr, Exact boundary condition perturbation for eigensolutions of the wave equation, Journal of Sound and Vibration 211 (3) (1998) 389 – 407.

[40] A. Cummings, I. J. Chang, R. J. Astley, Sound transmission at low frequencies through the walls of distorted circular ducts, Journal of Sound and Vibration 97 (2) (1984) 261 – 286.

[41] R. Pico, F. Gautier, The vibroacoustics of slightly distorted cylindrical shells: A model of the acoustic input impedance, Journal of Sound and Vibration 302 (1 - 2) (2007) 18 – 38.

[42] A. Sarkar, V. Sonti, Wave equations and solutions of in vacuo and fluid-filled elliptical cylindrical shells, International Journal of Acoustics and Vibration 14 (2007) 35 – 45.

[43] C. E. Wallace, Radiation resistance of a rectangular panel, The Journal of the Acoustical Society of America 51 (3B) (1972) 946 – 952.

[44] F. Fahy, P. Gardonio, in: Sound and Structural Vibration (Second Edition), Academic Press, Oxford, 2007.

[45] E. H. Dowell, G. F. Gorman III, D. A. Smith, Acoustoelasticity: General theory, acoustic natural modes and forced response to sinusoidal excitation, including comparisons with experiment, Journal of Sound and Vibration 52 (4) (1977) 519 – 542.

[46] B. Laulagnet, Sound radiation by a simply supported unbaffled plate, The Journal of the Acoustical Society of America 103 (5) (1998) 2451 – 2462.

[47] S. Kim, M. Brennan, A compact matrix formulation using the impedance and mobility approach for the analysis of structural-acoustic systems, Journal of Sound and Vibration 223 (1) (1999) 97 – 113.

[48] B. Venkatesham, M. Tiwari, M. L. Munjal, Analytical prediction of the breakout noise from a rectangular cavity with one compliant wall, The Journal of the Acoustical Society of America 124 (5) (2008) 2952 – 2962.

[49] B. Venkatesham, M. Tiwari, M. L. Munjal, Analytical prediction of break-out noise from a reactive rectangular plenum with four flexible walls, The Journal of the Acoustical Society of America 128 (4) (2010) 1789 – 1799.

[50] P. R. Stepanishen, Modal coupling in the vibration of fluid - loaded cylindrical shells, The Journal of the Acoustical Society of America 71 (4) (1982) 813 – 823.

[51] M. C. Junger, D. Feit, Sound, structures and their interaction, The MIT Press, Cambridge , Massachusetts, 1972.

[52] P. R. Stepanishen, Radiated power and radiation loading of cylindrical surfaces with nonuniform velocity distributions, The Journal of the Acoustical Society of America 63 (2) (1978) 328 – 338.

[53] B. Laulagnet, J. Guyader, Modal analysis of a shell's acoustic radiation in light and heavy fluids, Journal of Sound and Vibration 131 (3) (1989) 397 – 415.

[54] C. Wang, J. Lai, The sound radiation efficiency of finite length acoustically thick circular cylindrical shells under mechanical excitation I: Theoretical analysis, Journal of Sound and Vibration 232 (2) (2000) 431 – 447.

[55] R. Pico, F. Gautier, J. Redondo, Acoustic input impedance of a vibrating cylindrical tube, Journal of Sound and Vibration 301 (3 - 5) (2007) 649 – 664.

[56] M. Caresta, N. J. Kessissoglou, Acoustic signature of a submarine hull under harmonic excitation, Applied Acoustics 71 (1) (2010) 17 – 31.

[57] A. Cummings, Sound transmission through duct walls, Journal of Sound and Vibration 239 (4) (2001) 731 – 765.

[58] S. N. Yousri, F. J. Fahy, Distorted cylindrical shell response to internal acoustic excitation below the cut-off frequency, Journal of Sound and Vibration 52 (3) (1977) 441 – 452.

[59] C. R. Fuller, Radiation of sound from an infinite cylindrical elastic shell excited by an internal monopole source, Journal of Sound and Vibration 109 (2) (1986) 259 – 275.

[60] S. Temkin, Attenuation and dispersion of sound in dilute suspensions of spherical particles, The Journal of the Acoustical Society of America 108 (1) (2000) 126 – 146.

[61] S. Morioka, G. Matsui, Pressure-wave propagation through a separated gas-liquid layer in a duct, Journal of Fluid Mechanics 70 (1975) 721 – 731.

[62] M. Amabili, Free vibration of partially filled horizontal cylindrical shells, Journal of Sound and Vibration 191 (5) (1996) 757 – 780.

[63] M. Amabili, Flexural vibration of cylindrical shells partially coupled with external and internal fluids, Journal of Vibration and acoustics 119 (3) (1997) 476 – 484.

[64] A. Ergin, P. Temarel, Free vibration of a partially liquid-filled and submerged, horizontal cylindrical shell, Journal of Sound and Vibration 254 (5) (2002) 951 – 965.

[65] R. J. Alfredson, P. O. A. L. Davies, The radiation of sound from an engine exhaust, Journal of Sound and Vibration 13 (4) (1970) 389 – 408.

[66] A. D. Pierce, Acoustics: An introduction to its physical principles and applications, The Acoustical Society of America, Melville, NY, 1989.

[67] R. Courant, D. Hilbert, Methods of mathematical physics, Interscience Publishers, Inc., New York, 1953.

[68] M. Jensen, J. Freeze, A recursive Green's function method for boundary integral analysis of inhomogeneous domains, IEEE Transactions on Antennas and Propagation 46 (1998) 1810–1816.

[69] A. Selamet, Z. L. Ji, Acoustic attenuation performance of expansion chamber with two end-inlets/ one side-outlet, Journal of Sound and Vibration 231 (4) (2000) 1159 – 1167.

[70] A. Selamet, Z. L. Ji, Acoustic attenuation performance of circular expansion chambers with single-inlet and double-outlet, Journal of Sound and Vibration 229 (1) (2000) 3 – 19.

[71] N. W. McLachlan, Theory and application of Matheiu functions, Oxford Press, New York, 1947.

[72] F. D. Denia, L. Baeza, J. Albelda, F. J. Fuenmayor, Acoustic behaviour of elliptical mufflers with single inlet and double outlet, in: Proc. 10th International Congress on Sound and Vibration, Stockholm, Sweden, 2003, pp. 3287 – 3294.

[73] A. H. Nayfeh, Introduction to perturbation techniques, Wiley-Interscience, New York, 1981.

[74] S. Banerjee, A. M. Jacobi, Determination of transmission loss in distorted circular mufflers using a regular perturbation method, Journal of Vibration and Acoustics 136 (2014) 021013.

[75] R. G. Parker, C. D. Mote Jr., Exact perturbation for the vibration of almost annular or circular plates, Journal of Vibration and Acoustics 118 (1996) 436–445.

[76] W. Soedel, Vibrations of shells and plates, Marcel Dekker, Inc., New York, 2004.

[77] ASTM International, ASTM E2611 - 09 Standard Test Method for Measurement of Normal Incidence Sound Transmission of Acoustical Materials Based on the Transfer Matrix Method (2009).